Spring 5-2013

Nanoparticle Filled Polymeric Systems for Gas Barrier and Flame Retardant Properties

Yingji Wu
University of Southern Mississippi

The University of Southern Mississippi

NANOPARTICLE FILLED POLYMERIC SYSTEMS FOR GAS BARRIER AND FLAME RETARDANT PROPERTIES

by

Yingji Wu

Abstract of a Dissertation
Submitted to the Graduate School
of The University of Southern Mississippi
in Partial Fulfillment of the Requirements
for the Degree of Doctor of Philosophy

May 2013

ABSTRACT

NANOPARTICLE FILLED POLYMERIC SYSTEMS FOR GAS BARRIER AND FLAME RETARDANT PROPERTIES

by Yingji Wu

May 2013

Polymer composite gas barrier and fire retardant properties were studied in this investigation. An increase in the gas barrier property was observed by adding silicate nanotubes or clay nanoparticles into polymeric systems. Oxygen permeability, diffusivity, solubility and water vapor permeability were determined for polyimide/silicate nanocomposites with 0 to 9.99% (vol/vol) filler loading. Both oxygen and water vapor permeability for the system gradually decreased when adding increasing amounts of nanofiller up to 4.50% (vol/vol) and increase again after that. The permeability decreasewas caused by both the diffusivity and solubility coefficient changes, although diffusivity (the tortuous factor) is the main reason of permeability deduction.

Other than polyimide systems, high aspect ratio mica filled LLDPE/LDPE multilayer materials were used for gas barrier property improvement. Multilayer coextrusion is an attractive approach for creating designed particulate-filled nanocomposite polymer film structures with enhanced gas barrier properties. Multilayered materials were annealed above the melting temperature of the polymers to activate interdiffusion and to concentrate the mica platelets in the filled LLDPE layers. SEM, TEM and WAXS analysis were employed to probe the films' layer morphology and the platelet orientation/dispersion in the nanocomposite blends and nanoparticulate filled multilayer systems. The oxygen barrier of the blends and multilayer composites were

measured and related to their morphologies. It was shown particle concentrated multilayering leads to an enhancement in oxygen barrier properties as compared to the as-received multilayer materials and nanocomposite blends with the same mineral compositions.

Mica LLDPE/LDPE multilayers were tested for flammability. The multilayer technique and moving boundary effect causes further improvement of the flame retardant properties due to the particle concentration in the LLDPE layers. Although clay and various other types of nanoparticles have been reported and used as flame retardant materials, this study marks the first time nanoparticles were used as flame retardant materials in co-extruded multilayer systems. Flame retardant properties of the blends and multilayer composites were measured and related to the morphological observations. It was shown that multilayer materials have decreased peak heat release rate and enhanced char formation as compared to nanocomposite blends with the same mineral compositions.

Flame retardant materials, zinc acetate (ZnAc), zinc undecylenate (ZnUnd) and Zinc stearate (ZnSt), were studied for thermal degradation and flame retardant properties on standard epoxy/amine systems. The zinc salts had improved flame retardant properties (decreased peak heat release rate (PHRR), smoke emission and improved char formation) on epoxy/amine systems and the flame retardant efficiency order was ZnAc, ZnUnd and ZnSt. The char of ZnUnd epoxy/amine composites, with surface protecting zinc oxide layers, formed a better physical barrier for the flame. SEM and X-ray were used to further understand the mechanism of zinc salts on flame retardant properties.

The University of Southern Mississippi

NANOPARTICLE FILLED POLYMERIC SYSTEMS FOR GAS BARRIER AND FLAME RETARDANT PROPERTIES

by

Yingji Wu

A Dissertation
Submitted to the Graduate School
of The University of Southern Mississippi
in Partial Fulfillment of the Requirements
for the Degree of Doctor of Philosophy

Approved:

Sergei Nazarenko
Director

Jeffrey.Wiggins

Sarah Morgan

Daniel Savin

Kenneth Mauritz

Susan A. Siltanen
Dean of the Graduate School

May 2013

ACKNOWLEDGMENTS

I would like to thank my graduate research advisor, Dr. Sergei Nazarenko, for his mentorship. Without his consistent and illuminating instruction, I could not finish the dissertation and my Ph.D. study. There are numerous others to whom I would like to extend my gratitude including my graduate committee members, Dr. Jeffrey Wiggins, Dr. Sarah Morgan, Dr. Daniel Savin and Dr. Kenneth Mauritz. Their advice and support throughout my graduate career in Polymer Science and Engineering has been invaluable. I would also like to express my appreciation to Dr. Charles Manzi-Nshuti for his endless patience and help on my project.

I would like to acknowledge my fellow graduates within the Nazarenko Research Group and the Polymer Science department for their continuous support. My greatest gratitude towards the Center for Layered Polymeric Systems(CLiPS) for their support on my multilayer project, and especially to the Case Western Reserve University for their cooperative and helpful assistance. Thanks to Vladimir Yudin and his coworkers in Russian Academy of Sciences for providing nanotubes and polyimides.

Finally, I would like to thank my family and friends for their support and encouragement.

TABLE OF CONTENTS

LIST OF TABLES

Table

LIST OF ILLUSTRATIONS

Figure

CHAPTER I

RESEARCH BACKGROUND

Polymer Nanocomposites

Polymer nanocomposites have attracted great interest recently in the scientific and industrial areas. Nanocomposites have improved mechanical,[1,2] thermal,[3] gas barrier,[4,5] flame retardant,[6,7] electrical properties[8] and biodegradability[9] compared to pristine polymers. Nanocomposites are composites with well dispersed nanoparticles in the polymer matrices. Nanoparticles are particles with diameters below the micron dimension: generally, below 0.1 μm (100 nm). One of the feature of nanocomposites is the properties of materials with nanoparticles highly depend on the size of the nanoparticles.

Nanoparticles can be categorized into spherical nanoparticles, tube-like nanoparticles and plate- like nanoparticles. Spherical particles are isodimensional nanoparticles because the length, wide and thickness are all nanoscale. Spherical nanoparticles have large surface area and as the particle size decreased the ratio of surface area versus volume fraction increase. The particle size can be as small as several nanometers. Most common spherical nanoparticles are silica nanoparticles,[10,11] semiconductor nanoclusters[12] and metal oxide.[13,14] The interesting metal oxide are in most cases SiO_2, Al_2O_3, ZrO_2, TiO_2, Fe_2O_3, SnO_2, or ZnO with high application potential in different fields.[15] These metal oxide particles affect optical, magnetic or conducting properties of nanocomposites.

The tube-like nanoparticles are carbon nanotubes,[16] silicate nanotubes[17] and cellulose.[18] These nanoparticles have diameters in the nanoscale and length in the nanoscale or microscale which can be as long as several micrometers. Numerous

investigators have focused on carbon nanotubes. Carbon nanotubes (CNT) were first reported by Iijima in 1991,[16] and the first polymer nanocomposites using carbon nanotubes as a filler were reported in 1994 by Ajayan et al.[19] Nanotubes have great properties; Some nanotubes are stronger than steel, lighter than aluminum, and more conductive than copper.[20] Carbon nanotubes are long cylinders of covalently bonded carbon atoms and have aspect ratios over 1000. Using small amounts of nanoparticles in the polymer systems, the mechanical, electronical and thermal properties were significantly improved.[8] Disadvantages of using carbon nanotubes are that they are expensive and also polymers with carbon nanotubes show dark color.

Silicate type nanotubes were also studied recently for improving properties of polymeric materials. Naturally abundant halloysite nanotubes were able to improve flame retardant properties for thermal plastic systems just by simply blending the nanotubes with polypropylene.[21] Impact strength improved without sacrificing flexural modulus, strength and thermal stability in epoxy systems.[22] The chemical structures of silicate nanotubes is similar to the clay which will be described later, however, the shape is like the carbon nanotube.

Plate-like nanoparticles are one dimensional nanoparticles and this type of nanoparticles includes clay (layered silicate),[4,23] layered double hydroxides[24] and graphite.[25] These nanoparticles have thickness about 1 nm and the diameter varies from 30 nm to several microns. There is wide variety of both synthetic and natural clay. Montmorillonite (MMT) is one type of clay with a stacked layered structure under normal conditions. There are negative charges located on the layers and exchangeable cations between the layers. Each layer consists of two tetrahedrally coordinated silicon

atoms fused to an edge-shared octahedral sheet. The Chemical formula of MMT is $Na_x(Al_{4-x}Mg_x)Si_8O_{20}(OH)_4$ with particle diameter about 200 nm.[26] MMT is inexpensive compared to the carbon nanotubes and has lighter, light brown or yellow color. However, with the same amount of MMT and carbon nanotubes in the polymeric systems, polymer with carbon nanotubes usually has better mechanical and electronical properties. Another disadvantage of using MMT or other layered silicate is the difficulty to separate the layers to get totally exfoliated MMT nanocomposites because thin layers prefer to be stuck together forming a layered structure. MMT has a hydrophilic surface which may cause the phase separation when blend with hydrophobic polymers.

Depending on the dispersion of nanoparticles, there are microcomposites and nanocomposites. Nanocomposites have well dispersed nanoparticles in the polymer matrix and microcomposites are poorly dispersed composite systems where aggregates of nanoparticles are present in the microsize. Nanocomposites have better properties compared to microcomposites, however, improving dispersion of the nanoparticles is difficult in some polymer systems. Decreased performance is caused by the tendency for aggregate during processing and cause phase separation of nanoparticles and polymers. Aggregated nanoparticles can be disrupted into smaller particles by shear forces generating mechanical stress gradients or via chemical treatment. There are many factors affect the aggregation of particles: structures of nanoparticles, particle surface chemistry, modification of nanoparticles, preparation methods and so on.

Surface modification is the most efficient way to disperse nanoparticles in different polymers. To render silicate based nanoparticles miscible with hydrophobic polymers, the hydrophilic silicate surface must convert to an organophilic surface. For

layered silicate and silicate nanotubes, the organomodification can be done by cation exchange reactions[27] or silane coupling reaction.[28] Clay has an exchangeable cation on its surface which can react with alkylammonium or alkyl phosphonim cations to lower the surface energy of inorganic surface and improve wetting of polymer matrix. For some polymeric systems like polyolefins, modified polymers are often used to increase hydrophilicity of the polymer matrix. Polyethylene and polypropylenes are usually modified with maleic anhydride which can yield a hydrophilic carboxylic group. Clay can be fully exfoliated with less than 1% maleic anhydride modification to polyethylene systems.[29]

Gas Barrier Properties

Improving of gas barrier property is basically slowing down the gas transport through the membranes or films and result in decrease of gas permeability. Transport of a small molecule gas through a polymer membrane is a complex process that includes the sorption of gas molecules on the surface of the membrane; the diffusion through it; andfinally, the desorption of gas from the other surface of the membrane. The permeability describes the amount of gas that is able to transport through a thickness of film, over an area, a period of time and at a given pressure. The units of permeability are commonly expressed as cc(STP)·cm/(m^2·day·atm). The permeability (*P*) depends on the diffusivity (*D*) and solubility (*S*) of the gas molecules through the polymer films. The relation among these parameters can be shown using equation: $P = D \cdot S$. The step in diffusion is generally considered to be the movement of a polymer segment to provide a space into which a small molecule can move. Diffusivity should be correlated to the accessible (for a given gas) free volume fraction.[30,31]

Some polymers have high permeability of gas or water vapor which can be used for high gas permeable material applications like contact lenses and sport wear. Gas barrier materials can be used in medical application, food packaging and electronic materials. There are several ways to improve gas barrier properties of polymers: orientation of chains and increasing crystalinity, surface treatment using plasma or glass materials, surface coating of high barrier materials, blends of different polymers, multilayer materials, adding O_2 scavenger or adding particles.[32]

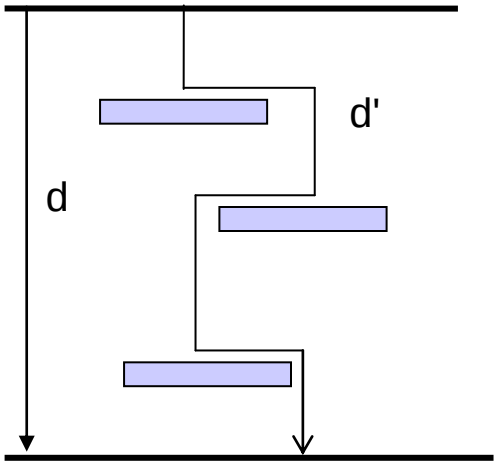

*Figure 1***.** A model for the path of a diffusing gas through the composites.[35]

Gas barrier properties of nanocomposites have been widely studied recently.[26,33,34] Impermeable nanoparticles in the nanocomposites can create a tortuous path for gas molecules as shown in Figure 1, where d is the thickness of the film for barrier test and d' is the total path of the gas molecule. The big decrease of the permeability coefficient in the nanocomposites was explained by the increase of the total path of the gas. Increasing gas barrier is therefore caused by decreasing the diffusion coefficient which is the rate of the gas molecules passing through a film with specific thickness and area at applied pressure. Solubility coefficient does not change much by adding nanoparticles in the polymeric systems.

Gas barrier properties are highly dependent on the particle shape, size (aspect ratio), volume percentage, and particle dispersion. Clays had previously been widely used for gas barrier property. Polyimide/layered silicate nanocomposites have shown reduction in permeability of small gases.[4,22] With 8% MMT by weight in a polyimide system dispersed using a solvent mixing method, the permeability decreased by more than 80%. In this study, aspect ratio was shown to affect gas barrier properties. High aspect ratio Mica (α = 1000) has the highest oxygen barrier when compared to the MMT (α = 200) and seponite (α = 160). In the different polymeric systems, gas barrier shows different results. In the nylon 6-MMT nanocomposites, permeability decreased by about 60% with 18% modified MMT by weight.[35]At low MMT loading,less than 10% inorganic content a majority of the dispersed tactoids did not contain more than 5 nanoplatelet sheets. At higher loadings, the number of middle size agglomerates (stacks of more than 10 nanoplatelet sheets) increased and permeability did not improve further by adding more fillers. Mitt and coworkers[36] found for polypropylene system with 20% MMT by weight, permeability decreased to 50% of pristine polypropylene. In the paper, a mixed morphology consisting of clay tactoids of varying thicknesses represented the microstructure of the composites.

Nazarenko and coworkers[37] studied gas barrier properties of polystyrene-MMT system and found that the aggregation and orientation of the nanoparticles affect barrier properties. In a polystyrene system, permeability decreased by 60% by adding about 16% MMT by weight percent. The gas permeablity only depended on volume percentage and aspect ratio of the nanoparticles when the particles are orientated and well dispersed in the system. The experimental data usually showed lower barrier performance because

nanoparticles are not perfectly orientated and several clay sheets were stacked together. The stack number, *N*, was also related to the gas barrier by the same effect as decreasing aspect ratio.

Graphite is also used for improvement in barrier properties. Graphite sheets are disk-like nanoparticles, similar to clay nanoparticles. Modified graphene was dispersed in the linear low density polyethylene by solution mixing.[38] The oxygen permeability was decreased by 47% with the addition of only 1 wt% of modified graphene. At the same amount of graphene loading, nitrogen permeability was decreased by 52% for pure LLDPE. Graphite nanocomposites have similar gas barrier effect to the clay contained nanocomposites.

Carbon nanotubes are also used to improve the gas barrier properties in different polymeric systems. As the carbon nanoparticlecontent is increased, a maximum reduction is reached in permeability of 28% for CO_2, 42% for O_2 and 58% for N_2 in polypropylene matrix.[39] These nanocomposites also have the same problems as clay nanocomposites which are dispersion and orientation of nanoparticles. Carbon nanotubes showed aggregation as well as random orientation. Moreover, bending of nanotubes was observed in the polymer systems. Improving these orientation and dispersion will help to improve gas barrier properties of nanocomposites.

Theoretical prediction is used to understand the barrier properties of nanocomposites systems. Relative gas permeability of composites filled with impermeable spheres was predicted using Maxwell's equation,[40]

$$\frac{P}{P_0} = \frac{1-\phi}{1+\frac{\phi}{2}} \qquad (1)$$

where P is the permeability of a composite medium, and P_0 is the permeability of polymer matrix, and ϕ is the volume fraction of impermeable phase. The permeability is dependant on the volume percentage of nanoparticles, with 1% of spheres in the polymer by volume only 1.5% permeability deductions expected based on the equation 1.

The Nielsen equation is typically used to describe molecular transport in heterogeneous systems with impenetrable platelets based on the tortuous path theory. Under the dilute regime, the disks are spaced at a distance much exceeding the disk radius r, corresponded to $nr^3 << 1$ and $\phi << 1$, where n is the number density and ϕ is the volume fraction of the nanoparticles. The diffusion in the dilute regime is described by the Nielsen formula,[41]

$$\frac{P}{P_0} = \frac{1-\phi}{1+\frac{\alpha}{2}\phi} \tag{2}$$

where P/P_0 is relative permeability, P is the permeability coefficient of the nanocomposites, P_0 is permeability coefficient of the neat polymer, α is aspect ratio of nanoplatlet ($\alpha = d/h$, d is diameter and h is thickness of particles) and ϕ is the volume fraction of the impermeable nanoparticles. Theretically, 1% MMT ($\alpha = 200$) by volume percent can decrease permeability by 50% which is really enormous compared to the spherical particles.

Under the semidilute regime, the disks are spaced at distances comparable or smaller than r, $nr^3 >> 1$ and $\phi << 1$. The diffusion in the semidelute regime is described by the Cussler formula.[42]

$$\frac{P}{P_0} = \frac{1-\phi}{1+(\frac{\alpha}{2}\phi)^2} \tag{3}$$

The difference between the two formulas is that gas molecules undergo multiple scatterings between close pairs of disks in semidilute regime compared to the dilute regime as shown in Figure 2. In this way the total path through the film is increased and better gas barrier properties can be obtained. The red line shows the path of gas molecules in the nanocomposite films.

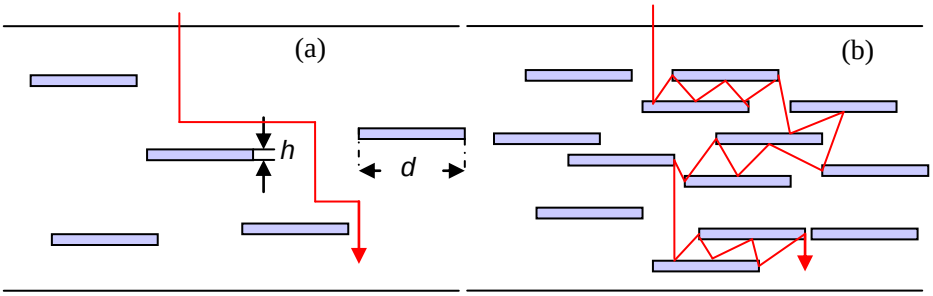

Figure 2. (a) The dilute regime of concentration in an oriented disk composite. (b) The semidilute regime of concentration in an oriented disk composite.

In Fredrickson and Shaqfeh's paper they consider a diffusion-controlled reaction in a composite material consisting of slender rods.[43] It assumed the tubes are aligned in the direction perpendicular to the gas path, with centers of the mass placed randomly in a homogeneous matrix. Gas molecules were assumed to diffuse in the matrix with diffusion coefficient D_0 and be instantly absorbed upon contact with a fiber. Two different regimes are described separately: dilute regime, $nL^3 << 1$, and semidilute regime, $nL^3 >> 1$ and $\phi << 1$. The dilute regime corresponds to the situation in which the average inter spacing is large relative to the length of the rod and semidilute regime corresponds to the situation in which the average inter spacing is small relative to the length of the rod but the volume fraction occupied by rods is still small.

According to this model the relative permeability in dilute regime is

$$P_{//} / P_0 = (1-\phi)\{1-(2\phi L^2 / d^2)^{3/2} /[3\ln^{5/2}(2L/d)]\} \quad (4)$$

where$P_{//}$ is the diffusivity of nanocomposites filled with nanotubes and P_0 is the permeability of pure polymer, L is the length of the nanotubes and d is the diameter of the nanotubes.

Relative permeability in semidilute regime is

$$P_{//} / P_0 = (1-\phi)[1-\frac{8}{3}\phi L^2 / d^2 / \ln^2(1/\phi)] \quad (5)$$

The theoretical model is assuming the particles are orientated to the direction parallel to film surface and no particle aggregation in the matrix. However, it is really difficult to get the perfect nanocomposites systems experimentally that permeability usually higher than predicted using these equations.

Flame Retardant Properties

Polymer materials have great advantages, for example, cheap price, light weight, flexible and enough strength. However, fire hazards associated with the use of these polymeric materials give concern to using polymers in some areas. Flame retardants reduce combustibility of the polymers and help to reduce the smoke and toxic fumes given off when materials burn. Flame retardant materials can be chlorinated paraffin, halogenated materials, particle filled composites, oxygen scavenger and intumescent flame retardants.[44] Halogenated materials are very efficient flame retardant materials, however, they produce toxic small molecular during combustion that it is very dangerous to use.[45] Industry is attempting to replace the halogenated flame retardant materials using halogen-free materials.

There are several different ways to measure the flammability of the polymer materials and the following are the five main types:[44] ignitability test (Ul94), flame spread test, limiting oxygen index (LOI), heat release test (Cone calorimeter) and smoke

test. Cone calorimeter is widely used for lab experiment and industrial area for fire test. This test can obtain total heat release, peak heat release rate (PHRR), smoke, amount of CO and CO_2, time to ignition and mass loss rate during the combustion of the polymers. Here, peak heat release rate is most important parameter which shows the size and intensity of the fire.

In order to improve polymer flame retardant properties, the fundamental combustion process of polymers should be understood first. Polymers pyrolyse to generate small molecules when exposed to high temperature and these small molecules are flammable or nan-flammable materials. Flammable fumes mix with oxygen in the atmosphere forming an ignitable blend and producing flame when met with a spark. The heat generated from the flame further decomposes of the polymers into flammable small molecules. The process is shown in Figure 3. In order to sustain fires, three important elements must be present: combustible fuel, heat and oxygen.

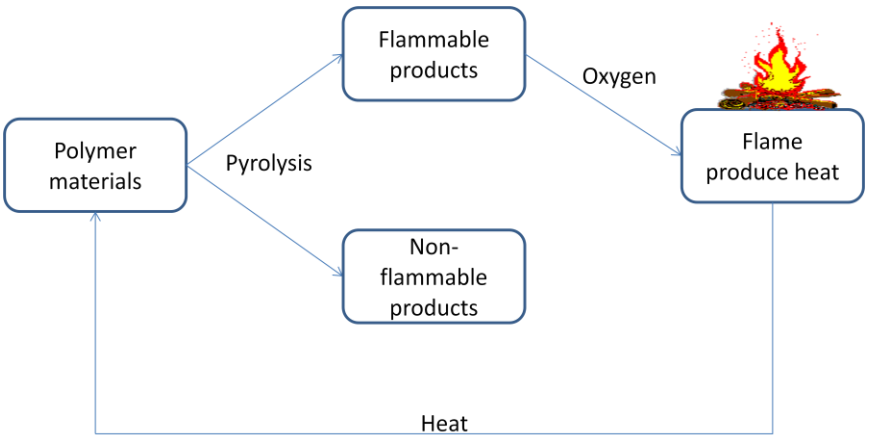

Figure 3. Polymer burning mechanism.

Recently, polymer nanocomposites appealed as one of the most promising developments in the area of flame retardant materials. Nanocomposites with different fillers such as: phosphorus,[46] clay,[47] carbon nanotube,[48] graphite,[49] silicate nanotube[50] and

metal oxide[51] have recently drawn great attention. These compounds mostly perform their flame retardant function in the condensed phase by increasing the amount of carbonaceous residue or char. These fillers can be used as particles mixed with polymers by blending or reacting with the polymer chain. Phosphorus materials are mostly studied to replace halogen flame retardant materials. Commercially available Ammonium polyphosphate (APP) can be used in some polymeric systems, for example, in epoxy formulations.[52] APP shows very high efficiency in epoxy resins, with 15% APP OI number increases from 22 to 31. APP is known as intumescent flame retardant which slows down heat and mass transfer between the gas and condensed phase. Three ingredients are needed to achieve intumescent flame retardant process: an acid source, a char forming agent and a blowing agent.

For inorganic flame retardants, clay and metal oxide are well known. As a typical example, PHRR of nylon 6 and nylon 6 with 5% MMT nanocomposites are 1011 kW/m^2 and 361 kW/m^2 respectively at 35 kW/m^2 heat fluxes as shown by Gilman.[6] Flame retardant properties improved when the nanoparticles exfoliated or intercalated in the polymers. Flame retardant properties decreased compared to the pure polymers with nanoparticles in poorly dispersed systems because MMT layers form stacks and elevated temperatures caused bigger flame. The mechanism of the flame retardant improvement with nanoparticles was studied previously. Lewin[53] suggests that the accumulation of the clay on the materials surface caused by the migration of the silicates to the surface prevents the oxygen and flammable gas from mixing with each other, also prevent hear from materials during the combustion. The migration of the clay from the bulk to the surface is caused by the rising bubbles of small molecule decomposition products of the

degrading polymer. Clay particles are claimed to act as catalyzer to promote char formation studied by Vaia et al.[54] The intimate contact between polymer and clays is essential for the advancement of the char process. Zhu and his coworkers[55] proposed another mechanism where the iron in the clays working as radical scavenger to improve flame retardant properties. Combustion of nanocomposites is a complex mechanism and this lead to decrease of PHRR.

Nanocomposite materials have the potential to improve both flame retardant properties and gas barrier properties. To improve these properties, good dispersion of nanoparticles needs to be achieved in the polymeric systems. Flame retardancy, gas barrier and particle dispersion are all strongly related. Exfoliated nanoparticles create tortuous path which decrease a diffusivity and permeability of the polymer membranes to improve gas barrier properties. On other hand, decrease permeability of oxygen can improve fire properties by cutting off the path of oxygen to the fuel produced from polymer decomposition. It is found that regardless of the kind of nanofillers, higher gas barrier properties (or lower gas permeability) usually produces lower flammability (or better flame retardancy).[56] Materials with both gas barrier and fire retardant properties can be widely applicable in the industrial products.

REFERENCES

1. Giannelis, E. P. Polymer Layered Silicate Nanocomposites. *Adv. Mater*. **1996**, *8*, 29–35.
2. Giannelis, E. P. Polymer-Layered Silicate Nanocomposites: Synthesis, Properties and Applications.*Appl. Organomet. Chem.* **1998**, *12*, 675–680.
3. Zhang, J.; Jiang, D. D.; Wilkie, C. A. Thermal and Flame Properties Of Polyethylene and Polypropylene Nanocomposites Based on An Oligomerically-Modified Clay. *Polym. Degrad. Stab*. **2005**, *91*, 298–304.
4. Yano, K.; Usuki, A.; Okada, A.; Kurauchi, T.; Kamigaito, O. Synthesis and Properties of Polyimide-Clay Hybrid. *J. Polym. Sci., Part A: Polym. Chem.* **1993**, *31*, 2493–2498.
5. Bharadwaj R.K. Modeling the Barrier Properties of Polymerlayered Silicate Nanocomposites. *Macromolecules* **2001**, *34*, 9189–9192.
6. Gilman J.W. Flammability and Thermal Stability Studies of Polymer-Layered Silicate (Clay) Nanocomposites. *Appl. Clay Sci*. **1999**, *15*, 31–49.
7. Gilman J.W.; Jackson C.L.; Morgan A.B.; Harris Jr R.; Manias E.; Giannelis E.P,; Wuthenow M.; Hilton D.; Phillips S.H. Flammability Properties of Polymer-Layered Silicate Nanocomposites. Polypropylene and Polystyrene Nanocomposites. *Chem. Mater*. **2000**, *12*, 1866–1873.
8. Moniruzzaman, M.; Winey, K. I. Polymer Nanocomposites Containing Carbon Nanotubes. *Macromolecules* **2006**, *39*, 5194–5205.
9. Lee, S.R.; Park, H.M.; Lim, H.L.; Kang, T.; Li, X.; Cho, W.J.; Ha, C.S. Microstructure, Tensile Properties, and Biodegradability of Aliphatic Polyester/Clay

Nanocomposites. *Polymer* **2002**, *43*, 2495–2500.

10. Mark, J.E. Ceramic Reinforced Polymers and Polymer-Modified Ceramics. *Polym. Eng. Sci.* **1996**, *36*, 2905–2920.
11. Reynaud, E.; Gauthier, C.; Perez, J. Nanophases in Polymers. *Rev. Metall./Cah. Inf. Tech.* **1999**, *96*, 169–176.
12. Herron, N.; Thorn, D.L. Nanoparticles. Uses and Relationships to Molecular Clusters. *Adv. Mater.* **1998**, *10*, 1173–1184.
13. Li, C.; Wu, J.; Zhao, J.; Zhao, D.; Fan, Q. Effect of Inorganic Phase on Polymeric Relaxation Dynamics in PMMA/Silica Hybrids Studied By Dielectric Analysis. *Eur. Polym. J.* **2004**, *40*, 1807–1814.
14. Hanemann, T.; Szabo, D. V. Polymer-Nanoparticle Composites: From Synthesis to Modern Applications. *Materials* **2010**, *3*, 3468–3517.
15. Lewin, M.; Endo, M. Catalysis of Intumescent Flame Retardancy of Polypropylene by Metallic Compounds. *Polym. Adv. Technol.* **2003**, *14*, 3–11.
16. Iijima, S. Helical Microtubules of Graphitic Carbon.*Nature* **1991**, *354*, 56–58.
17. Yudin, V. E.; Otaigbe, J. U.; Gladchenko, S.; Olson, B. G.; Nazarenko, S.; Korytkova, E. N.; Gusarov, V. V. New Polyimide Nanocomposites Based on Silicate Type Nanotubes: Dispersion, Processing and Properties. *Polymer* **2007**, *48*, 1306–1315.
18. Bledzki, A. K.; Gassan, J. Composites Reinforced with Cellulose Based Fibres. *Prog. Polym. Sci.* **1999**, *24*, 221–274.
19. Ajayan, P. M.; Stephan, O.; Colliex, C.; Trauth, D. Aligned Carbon Nanotube Arrays Formed by Cutting A Polymer Resin-Nanotube Composite. *Science* **1994**, *265*,

1212–1214.

20. Moniruzzaman, M.; Winey, K. I. Polymer Nanocomposites Containing Carbon Nanotubes.*Macromolecules* **2006**, *39*, 5194–5205.
21. Du, M.; Guo, B.; Jia, D. Thermal Stability and Flame Retardant Effects of Halloysite Nanotubes on Polypropylene. *Eur. Polym. J.* **2006**, *42*, 1362–1369.
22. Ye, Y.; Chen, H.; Wu, J.; Ye, L. High Impact Strength Epoxy Nanocomposites with Natural Nanotubes. *Polymer* **2007**, *48*, 6426–6433.
23. Yano, K.; Usuki, A.; Okada, A.Synthesis and Properties of Polyimide-Clay Hybrid Films.*J.Polym. Sci., Part A: Poly.Chem.* **1997**, *35*, 2289–2294.
24. Oriakhi, C. O.; Farr, I. V.; Lerner, M. M. Thermal Characterization of Poly(Styrene Sulfonate)/Layered Double Hydroxide Nanocomposites. *Clays Clay Miner*. **1997**, *45*, 194–202.
25. Shioyama, H. Polymerization of Isoprene and Styrene in the Interlayer Spacing of Graphite. *Carbon* **1997**, *35*, 1664–1665.
26. Alexandre, M.; Dubois, P. Polymer-LayeredSilicateNanocomposites: Preparation, Propertiesand Uses of A New Class of Materials.*Mater. Sci. Eng., R: Reports* **2000**, *28*, 1–63.
27. Krishnamoorti, R.; Vaia, R. A.; Giannelis, E. P. Structure and Dynamics of Polymer-Layered Silicate Nanocomposites.*Chem. Mater*. **1996**, *8*, 1728–1734.
28. Arkles, B. Tailoring Surfaces with Silanes. *Chem. Tech.* **1977**, *7*, 766–778.
29. Wang, K. H.; Choi, M. H.; Koo, C. M.; Choi, Y. S.; Chung, I. J. Synthesis and Characterization of Maleated Polyethylene/Clay Nanocomposites. *Polymer* **2001**, *42*, 9819–9826.

30. Cohen M.H.; Turnbull, D. Molecular Transport in Liquids and Glasses. *J. Chem. Phys*. **1958**, *31*, 1164–1169.

31. Budd, P.M.; McKeownb, N.B.; Fritsch, D. Free Volume and Intrinsic Microporosity in Polymers.*J. Mater. Chem.* **2005**, *15*, 1977–1986.

32. Hu, Y. S.; Mehta, S.; Schiraldi, D. A.; Hiltner, A.; Baer, E. Oxygen Transport As A Solid-State Structure Probe for Polymeric Materials: A Review. *J.Polym.Sci., PartB: Polym.Phys.* **2005**, *43*, 1365–1381.

33. Sorrentino, A.; Gorrasi, G.; Tortora, M.; Vittoria, V. Barrier Properties of Polymer/Clay Nanocomposites. *In Polymer Nanocomposites*. Mai, Y., Yu, Z., Eds.; Woodhead Publishing Ltd. Cambridge, UK **2006**, 273–296.

34. Choudalakis, G.; Gotsis, A. D. Permeability of Polymer/Clay Nanocomposites: A Review.*Eur. Polym. J.* **2009**, *45*, 967–984.

35. Picard, E.; Vermogen, A.; Gerard, J.-F.; Espuche, E. Barrier Properties of Nylon 6-Montmorillonite Nanocomposite Membranes Prepared by Melt Blending: Influence of the Clay Content and Dispersion State. *J.Membr.Sci.* **2007**, *292*, 133–144.

36. Mittal, V. Gas Permeation and Mechanical Properties of Polypropylene Nanocomposites with Thermally-Stable Imidazolium Modified Clay. *Eur.Polym.J.* **2007**, *43*, 3727–3736.

37. Nazarenko, S.; Meneghetti, P.; Julmon, P.; Olson, B. G.; Qutubuddin, S. Gas Barrier of Polystyrene Montmorillonite Clay Nanocomposites: Effect of Mineral Layer Aggregation. *J.Polym.Sci., Part B: Polym. Phys.* **2007**, *45*, 1733–1753.

38. Kuila, T.; Bose, S.; Mishra, A. K.; Khanra, P.; Kim, N. H.; Lee, J. H. Effect of Functionalized Graphene on the Physical Properties of Linear Low Density

Polyethylene Nanocomposites. *Polym.Test*. **2012**, *31*, 31–38.

39. Vassiliou, A.; Bikiaris, D.; Chrissafis, K.; Paraskevopoulos, K. M.; Stavrev, S. Y.; Docoslis, A. Nanocomposites of Isotactic Polypropylene with Carbon Nanoparticles Exhibiting Enhanced Stiffness, Thermal Stability and Gas Barrier Properties. *Compos.Sci.Technol.* **2008**, *68*, 933–943.
40. Petropoulos, J.H. Mechanisms and Theories for Sorption and Diffusion of Gases in Polymers. In *Polymer gas separation membranes*; Paul, D.R., Yampolsk'skii, Y.P., Eds,; CRC Press: Boca Raton, Florida, **1994**; chapter 2, 17–81.
41. Nielsen, L. E. Models for the Permeability of Filled Polymer Systems. *J. Macromol. Sci., Part A* **1967**, *1*, 929–942.
42. Cussler, E. L.; Hughes, S. E.; Ward, W. J., III; Aris, R.Barrier Membranes. *J. Membr.Sci.* **1988**, *38*, 161–174.
43. Fredrickson, Glenn H.; Shaqfeh, Eric S. G. Heat and Mass Transport in Composites of Aligned Slender Fibers. *Phys. Fluids A: Fluid Dynamics* **1989**, *1*, 3–20.
44. Lu, S.; Hamerton, I. Recent Developments in the Chemistry of Halogen-Free Flame Retardant Polymers. *Prog. Polym. Sci.* **2002**, *27*, 1661–1712.
45. Weil, E. D.; Levchik, S.V. Flame Retardants in Commercial Use or Development for Polyolefins. *J. Fire Sci*. **2008**, *26*, 5–43.
46. Green, J. A Review of Phosphorus-Containing Flame Retardants.*J. Fire Sci*. **1992**, *10*, 470–487.
47. Kiliaris, P.; Papaspyrides, C. D. Polymer/Layered Silicate (Clay) Nanocomposites: An Overview of Flame Retardancy. *Prog.Polym. Sci*. **2010**, *35*, 902–958.
48. Bourbigot, S.; Samyn, F.; Turf, T.; Duquesne, S. Nanomorphology and Reaction to

Fire of Polyurethane and Polyamide Nanocomposites Containing Flame Retardants. *Polym. Degrad. Stab.* **2010**, *95*, 320–326.

49. Moon, S.; Jo, B.W.; Farris, R. J.Flame Resistance and Foaming Properties of NBR Compounds with Halogen-Free Flame Retardants. *Polym.Compos.* **2009**, *30*, 1732–1742.
50. Marney, D. C. O.; Russell, L. J.; Wu, D. Y.; Nguyen, T.; Cramm, D.; Rigopoulos, N.; Wright, N.; Greaves, M. The Suitability of Halloysite Nanotubes As A Fire Retardant for Nylon 6. *Polym. Degrad. Stab*. **2008**, *93*, 1971–1978.
51. Linteris, G. T.; Rumminger, M.c D.; Babushok, V. I. Catalytic Inhibition of Laminar Flames by Transition Metal Compounds. *Prog.Energy Combust. Sci.* **2008**, *34*, 288–329.
52. Levchik, S. V.; Weil, E. D. Thermal Decomposition, Combustion and Flame-Retardancy of Epoxy Resins - A Review ofthe Recent Literature. *Polym. Int*. **2004**, *53*, 1901–1929.
53. Lewin M. Some Comments on the Modes of Action of Nanocomposites in the Flame Retardancy of Polymers. *Fire Mater.* **2003**, *27*, 1–7.
54. Vaia, R.A.; Price, G.; Ruth, P.N.; Nguyen, H.T.; Lichtenhan, J. Polymerlayered Silicate Nanocomposites As High Performance Ablative Materials. *Appl. Clay. Sci.* **1999**, *15*, 67–92.
55. Zhu, J.; Uhl, F.M.; Morgan, A.B.; Wilkie, C.A. Studies on the Mechanism by Which the Formation of Nanocomposites Enhances Thermal Stability. *Chem. Mater.* **2001**, *13*, 4649–4654.
56. Song, P.; Yu, Y.; Zhang, T.; Fu, S.; Fang, Z.; Wu, Q. Permeability, Viscoelasticity,

and Flammability Performances and Their Relationship to Polymer Nanocomposites.*Ind. Eng. Chem. Res.* **2012**, *51*, 7255–7263.

CHAPTER II

RESEARCH OVERVIEW

The addition of rigid particles to polymers can produce a number of desirable effects, including increase in stiffness and toughness, a reduction in the coefficient of thermal expansion and an increase in gas barrier properties and flame retardancy as mentioned in Chapter I. This dissertation focuses on polymer composite gas barrier properties and flame retardancy. Different additives, for example, plate-like structured mica, tube-like structured chrysotile nanotubes and metal compunds were investigated in various polymer systems.

Polymer composites with plate-like particles were widely investigated previously. However, tube-like particles are not well understood. Chapter III describes the study of the gas barrier properties of silicate nanotube filled polyimide nanocomposites. Based on the theoretical prediction by Fredrickson and Shaqfeh, nanotubes decrease the permeability in polymer systems by creating a tortuous path for the gas molecules. Oxygen and water vapor permeability, diffusivity and solubility are studied, analyzed and correlated to the particle dispersion and mechanical properties. The difference between the theoredical prediction and the experimental data was discussed.

The Goal of Chapter IV is to evaluate the oxygen barrier properties of multilayer materials containing high aspect ratio mica particles. It is well known that nanoparticles can improve gas barrier properties by blending or reacting with polymers. Gas barrier properties improved when adding a sufficient amount of these inorganic particles. However, poor dispersion of the nanopaticles with high loading nanocomposites systems limited the application of the nanocomposites in various areas. Combined with multilayer

technology and the moving boundary effect, the gas barrier properties improved with particle low loading composites systems.

In Chapter V, flame retardancy and thermal properties are evaluated for particle filled multilayer systems. It is the first time that co-extruded multilayer systems have been studied for their flame retardant properties. Multilayer technology gives rise to improved flame retardancy compared to similarly loaded, composite systems, allowing for higher performance with lower loading levels. The mechanism of combustion for the conventional nanocomposites and multilayer composites are compared and studied. It is interesting to know how the particle content, particle dispersion, multilayer thickness and moving boundary phenomena affects the flammability of the polymers.

The main objective of Chapter VI is to establish a fundamental understanding of Zn salts on the flammability of epoxy/amine systems. Epoxy/amine systems with different Zn salts are studied for flammability. Compared to conventional flame retardants, Zn salts are halogen free and environmentally safe. The efficiency of these flame retardants is studied and compared to each other. The flammability test is conducted using a cone calorimeter. In order to investigate the burning machnism, char and partially pyrolyzed materials are also analyzed using TGA, SEM, XRD, and SEM-EDX.

CHAPTER III

GAS BARRIER BEHAVIOR OF POLYIMIDE NANOCOMPOSITES WITHSYNTHETIC CHRYSOTILE NANOTUBES

Abstract

Chrysotile nanotubes (ChNTs) were synthesized under hydrothermal conditions. These synthetic nanotubes crystallographically and morphologically mimic the nanofibrils of a natural white asbestos but they are considerably shorter. ChNTs containing polyimide nanocomposites were prepared by solution mixing/casting method. Oxygen and water vapor barrier of the nanocomposite films was tested and related to the amount, dispersion, and orientation of the nanotubes. The dispersion and orientation of the nanotubes was examined by transmission electron microscopy (TEM). The nanotubes were nanodispersed and oriented in the plane of the film in the nanocomposites with up to 4.5% (vol/vol) of ChNTs leading to a gradual increase of the gas barrier. The lowest gas permeability was 60% smaller than that for the pristine polyimide film. However, with the onset of nanotube micro aggregation at larger ChNTs loadings the nanotube dispersion and orientation were compromised and oxygen barrier was reduced. The efficacy of nanotubes to enhance polymer gas barrier was discussed and compared with that by nanoplatelets.

Introduction

Creating nanocomposites by mixing a polymer with inorganic nanoparticles represents one of the most simple and efficient approaches for making new materials with enhanced benefits.[1,2] The benefits often are considerably better than one may expect from a simple sum of the constituent properties. Gas barrier enhancement, important for

various packaging applications, is one of the most vivid examples of this potential synergy. Adding a small amount of mineral nanoparticles may lead to a considerable enhancement of the gas barrier. Particulates improve the gas barrier properties of a polymer by reducing the volume accessible for gas transport and also by creating a more tortuous diffusion path. The most common and successful low filler (1-15% wt/wt) gas barrier formulations known today employ high aspect ratio platelet shaped nano silicates also renown as 2-D nanoparticles. The formulations with 2-D montmorillonite clay (MMT) were investigated more often than others. Depending on the amount of filler used, the platelet aspect ratio, and the state of the silicate layers dispersion and orientation, a 20-90% reduction of the gas permeability as compared to pure polymer control has been reported, with about a 20-60% reduction reported for MMT based nanocomposites.[3-7]

A question was posed if tubular 1-D nanoparticulates can be employed as successfully as 2-D nanoplatelets to enhance polymer gas barrier. It has been numerously demonstrated and widely accepted that adding a small fraction of fibrous inclusions can drastically improve many physical properties of a composite such as modulus, viscosity, thermal, and electrical conductive properties.[8,9] We have not been able to identify any systematic investigations specifically dealing with an effect of fibrous inclusions on the gas barrier. In the two reports (outside our group efforts) the gas barrier of ultra-high aspect ratio multi-wall carbon nanotube (MWCN) containing nanocomposites, however, was evaluated as a part of multi-pronged characterization efforts. Sanchez-Garcia et al. along with the morphological characterization and evaluation of thermal, mechanical and electrical properties of MWCN containing nanocomposites based on polycaprolactone (PCL) and polyhydroxybutyrate-*co*-valeriate (PHBV) also reported on the oxygen

barrier.[10] The nanocomposites were prepared via solution mixing/casting method. Oxygen permeability was excitingly reduced by 52% for MWCN/PCL and 62% for MWCN/PHBV nanocomposites containing 1% (wt/wt) of the nanotubes as compared to those for the pristine PCL and PHBV matrixes. Adding more nanotubes, however, led to an increase of oxygen permeability which was attributed to the nanotube aggregation. Song et al. in addition to thermal, rheological, and fire retardant data reported on the oxygen and water vapor barrier of a carbon nanotube (CN) polypropylene (PP) nanocomposite with 1% (wt/wt) of CN.[11]The nanocomposite was prepared via melt blending. The oxygen and water permeability showed only about 10% reduction. In conclusion, the information on the efficacy of the nanotubes to enhance polymer gas barrier is rather scarce, controversial and calls for a more thorough investigation which we aimed in this work.

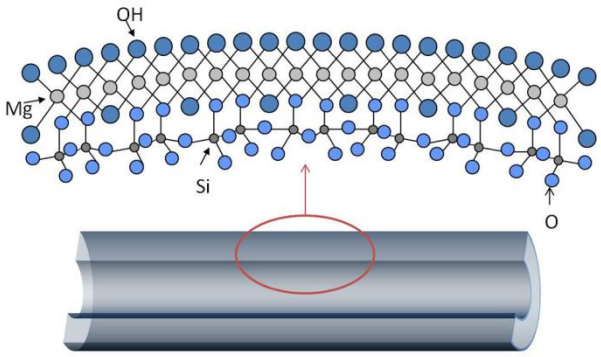

*Figure 4***.** A schematic of the chrysotile hollowed tube structure.

In this study a different than carbon kind of nanotubes was chosen, i.e. the synthetic chrysotile nanotubes. The synthesis of the nanotubes of magnesium hydrosilicate $Mg_3Si_2O_5(OH)_4$with a chrysotile structure has been described elsewhere.[12,13] The ChNTs crystallographically and morphologically mimic the white asbestos, a compound which belongs to the serpentine group of minerals. However,

synthetic ChNTs are significantly shorter than white asbestos nanofibers. A schematic of the nanotube crystalline structure is shown in Figure 4, and it consists of a magnesium hydroxide octahedral framework on the outside and a silicon oxide tetrahedral framework on the inside. Therefore the surface of ChNTs is naturally hydroxylated. The hollowed tube organization of the nanotubes is due to a mismatch of the adjacent crystalline lattices. It has been demonstrated elsewhere that the size and the shape of the ChNTs can be controlled during their synthesis under hydrothermal conditions. This makes it possible to tune ChNT dimensions for various end use applications. Often ChNTs do not require any chemical treatment to be nanodispersed in polymer matrices. A presence of the hydroxyl groups on the surface of ChNTs permits various additional surface treatments to further enhance and to tune the nanotube miscibility in various organic matrices when needed.

A polyimide was selected as the polymer matrix. Polyimides represent an important polymer class widely employed for various advanced applications primarily due to their superior thermal stability and chemical resistance.[14,15] ChNTs containing polyimide nanocomposites were prepared via solution mixing/casting method. The preparation methodology and general characterization of these nanocomposites have been originally described elsewhere.[16] The main purpose of this work was to evaluate the gas barrier of ChNTs containing polyimide nanocomposites and relate it to the amount, dispersion, and orientation of the nanotubes.

Experimental

Chrysotile nanotubes were synthesized in a high pressure autoclave from a mixture of magnesium and silicon oxides under hydrothermal conditions.[12] The conditions were as follows: molar ratio between MgO and SiO_2 in initial mixture was

equal to 1.5, which corresponds to the stoichiometric ratio of these compounds, temperature and pressure were 350 ℃ and 70 MPa, NaOH content in hydrothermal solution was 1% (wt/wt), and the overall reaction duration was 24 hours.

Poly(amic acid) of poly(pyromellitic dianhydride-*co*-4,4'-oxydianiline) (PAA-PMDA) was purchased from Sigma-Aldrich in the form of 15% (wt/wt) solution in N-methyl-2-pyrrolidone (NMP). Poly(pyromellitic dianhydride-*co*-4,4'-oxydianiline) (PMDA-ODA) polyimide films (30-60 μm thickness) were prepared by casting of the solution onto soda lime glass plates followed by curing in the convection oven first at room temperature and then using a series of elevated temperatures 100, 200 and 300 ℃ for one hour at each temperature to reach complete imidization. Standard infra-red spectroscopy (FTIR Perkin-Elmer 180) confirmed the formation of polyimide via observing the characteristic absorption peaks occurring at 1780, 1720, 1380, 725 cm^{-1} that are typical for aromatic polyimide.[14] Subsequently, the cast films were removed after complete imidization from the glass plates by soaking in water. The films were dried in a vacuum oven. The density of the PMDA-ODA films was 1.42 g/cm^3.

The PMDA-ODA/ChNT nanocomposite films containing different concentrations of ChNTs were prepared by adding the desired amount of ChNTs to NMP. The resulting dilute ChNTs suspension in NMP was homogenized for 30 min in an ultrasonic bath (40 kHz). The sonicated ChNT suspension was transferred into a three-neck round bottom flask equipped with a mechanical stirrer, a nitrogen gas inlet, and a drying tube outlet filled with calcium sulfate. After stirring the ChNT solution for 10 min, PAA-PMDA was added into the ChNT suspension and the stirring of the mixture was continued for an additional 60 min until a constant viscosity was obtained. The solid content of the

ChNT/PAA-PMDA solution was 10% (wt/wt) in NMP. Thin PMDA-ODA/ChNT films with varying ChNT content in the polymer (2.9, 3.9, 4.8, 6.5, 7.0, 7.8, 9.1, 13.0 and 16.7% (wt/wt)) were prepared from the ChNT/PAA-PMDA solution by casting as already described above for the pure (unfilled) PMDA-ODA polyimide films. Film thicknesses varied from 0.03 mm to 0.07 mm which was determined by measuring several points on the films using a micrometer and calculating an average thickness. Assuming the two phase model the corresponding mineral volume fractions (*vol*) of the PMDA-ODA/ChNT nanocomposite samples used in this work have been determined using Eq. 1 from known mineral weight fractions (*wt*) as follows:

$$vol = \frac{1}{(\frac{1}{wt} - 1)\frac{\rho_2}{\rho_1} + 1} \tag{1}$$

whereρ_1 and ρ_2 are the densities of the polymer and the nanotubes, 1.42 g/cm^3 and 2.56 g/cm^3, respectively. Nanocomposite weight and volume compositions are listed in Table 1. TEM observations were carried out using a Zeiss 109T TEM operated at 80 kV. Prior to the measurements, ChNTs were dispersed in ethanol (USP grade) at 0.02% (wt/wt) and sonicated for 2 hours in an ultrasonic bath. A small droplet was placed on each TEM grid and dried in air.Samples of PMDA-ODA/ChNT films for the TEM analysis were imbedded in epoxy resin and microtomed using a Leica EM FC6 ultramicrotome. The glass knife was used at room temperature to give about 70 nm thick cross sections.

Oxygen barrier of the PMDA-ODA/ChNT nanocomposites were measured at 25 ℃, 0% RH and 1 atm partial oxygen pressure difference using a commercially manufactured diffusion apparatus OX-TRAN® 2/21 ML (MOCON). Water vapor barrier was measured at 37.8 ℃ and at a partial pressure difference which corresponds to 100%

RH using a diffusion apparatus PERMEATRAN-W® Model 3/33 MG (MOCON). Both instruments employ a continuous-flow method (ASTM D3985-81 and ASTM F1249-01) with nitrogen as a carrier gas to measure oxygen and water vapor flux through polymeric films. The film specimens were masked to aluminum foil with a circular exposure area of 5 cm^2. The masked specimens were conditioned in a vacuum desiccator for more than 12 hours before testing in order to remove any traces of oxygen and water vapor. Oxygen and water vapor flux $J(t)$ was measured. A solution to Fick's second law was employed (Eq.2) to fit the experimental oxygen flux data. From this two parametric fit the permeability P and diffusivity D were calculated as described elsewhere.[17]

$$J(t) = \frac{P\Delta p}{l}[1 + 2\sum_{n=1}^{\infty}(-1)^n \exp(-\frac{D\pi^2 n^2 t}{l^2})] \quad (2)$$

where Δp is the oxygen partial pressure difference, here is 1 atm, l is the thickness of the film and t is the time. The solubility S was calculated from the relationship $P = D \cdot S$. The permeability coefficient P can be also calculated directly from the steady-state flux J_∞ value as follows $P = J_\infty l / \Delta p$. The steady-state flux method was used to calculate the permeability coefficient of water vapor.

Young's modulus (E) of the nanocomposite films was measured using a tensile testing instrument (Alliance RT/10, MTS systems Co., Ltd.) according to ASTM D882-95. The specimen gauge length and width were 50 mm and 5 mm. Special care was taken to ensure the proper specimen alignment in the grips. Abrasive paper was used between the specimen and the grip surfaces to prevent any possible slippage. The Young's modulus was determined at a strain not exceeding 0.5%. Ten replicate measurements were conducted for each sample and the average results of the ten specimens are reported in this article. The error in the modulus measurements was about 5%.

Results and Discussion

Nanotube Morphology and Dimensions

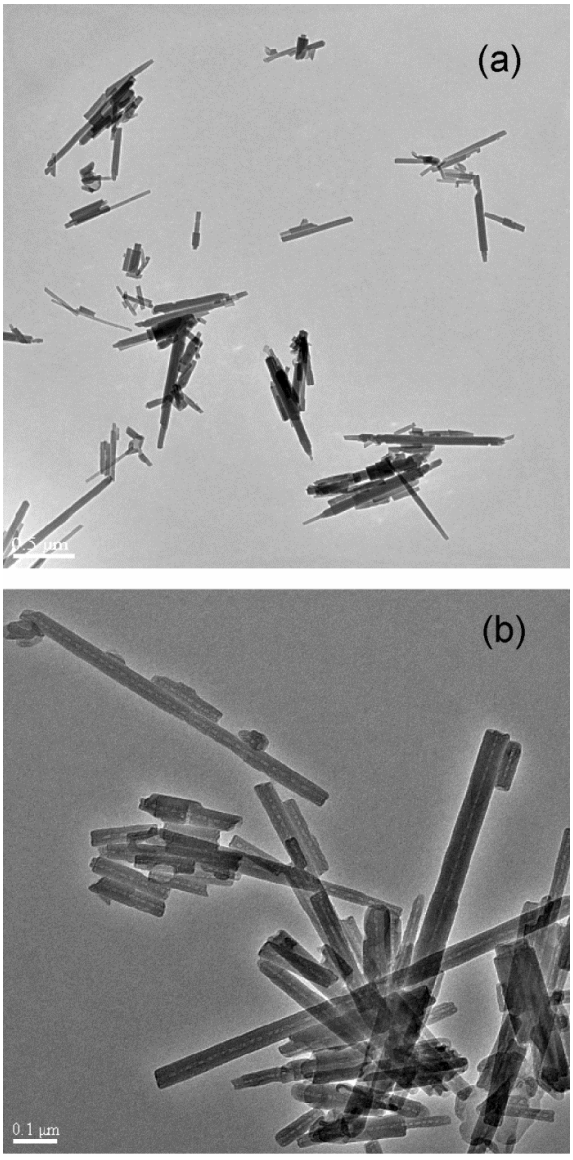

*Figure 5***.** TEM of the nanotubes obtained at various magnifications: (a) low and (b) high.

Figure 5 shows TEM images of the nanotubes after the ethanol solvent in which they were dissolved at low concentration was evaporated prior to the measurements. The images clearly revealed both single nanotubes and nanotube bundles. A broad distribution of the nanotube sizes is in particular apparent when observing the lower magnification

image (Figure 5a). Cylinder-in-cylinder morphology, the defect form of chrysotile tubular structure, can also be occasionally observed in the micrographs. As expected, all the nanotubes appeared lighter (lower electron density) in the nanotube central region, indicative of the inner channel. It has been reported elsewhere that ChNTs have the capacity to absorb water as well as other small gas molecules both onto the outer surface and within these inner nano channels.[18] Therefore the channels appear obstructed all the time.

The statistical analysis of the nanotube dimensions was conducted by using multiple TEM images of the nanotubes. About 300 nanotubes were analyzed to construct the corresponding statistical histograms of the nanotube lengths (L), outer diameters (d), and aspect ratios ($\alpha_t = L/d$). The histograms are shown in Figure 6. The dimensions varied broadly. The lengths varied from 100 to 2800 nm, the diameters from 20 to 95 nm, and the aspect ratios from 2 to 70. Therefore the nanotube lengths varied more than the diameters. The most probable (the maximum on the corresponding histograms) length, diameter, and aspect ratio were determined as 200-300 nm, 40-45 nm, and 4-6. The mean quantities were also calculated as 467 nm, 45 nm, and 10.5 respectively. Interestingly, the mean value of the outer diameter was comparable with the most probable value, but the number average length and aspect ratio values were larger than the corresponding most probable values.

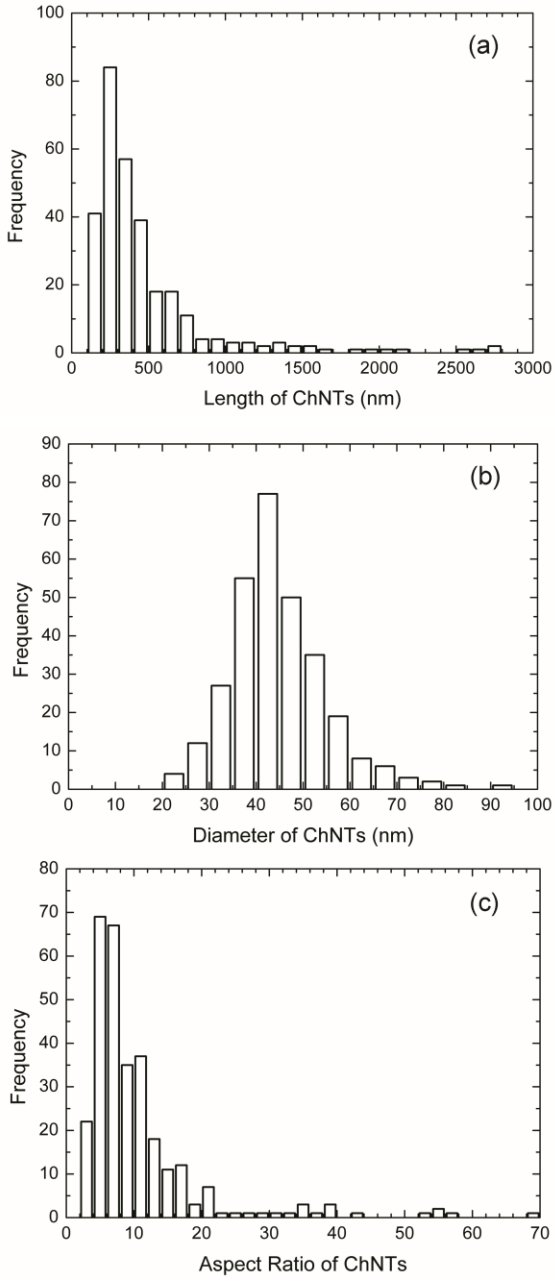

Figure 6. Statistical histograms of the nanotube dimensions: (a) length, *L*; (b) outer diameter, *d*; and (c) aspect ratio, *α*.

Nanotube Dispersion

A comprehensive TEM view of the nanotube dispersion in polyimide matrix is shown in Figure 7. A global view of the ChNTs dispersion, using lower magnification displayed a marked absence of large aggregates for the concentrations up to 4.5%

(vol/vol) (Figures 4a and 4b). Both nanotubes and bundles can only be seen (Figure 7d). Bundles contained about 3 to 10 nanotubes with polymer trapped in between nanotubes. The number of bundles, as well as the number of nanotubes per bundle, gradually increased with the mineral composition. TEM clearly revealed the in-plane orientation of the nanotubes and the bundles in the film. Figure 7b is in particular revealing as it captured the edge of the film. This image, as well as other images, was obtained from the cross-section of the film and the nanotubes are seen either as dots or as line segments of various lengths parallel to the film surface. Therefore, long axes of the nanotubes and the bundles are parallel (in-plane) to the film surface but within the plane the orientation of the nanotubes and the bundles is random.

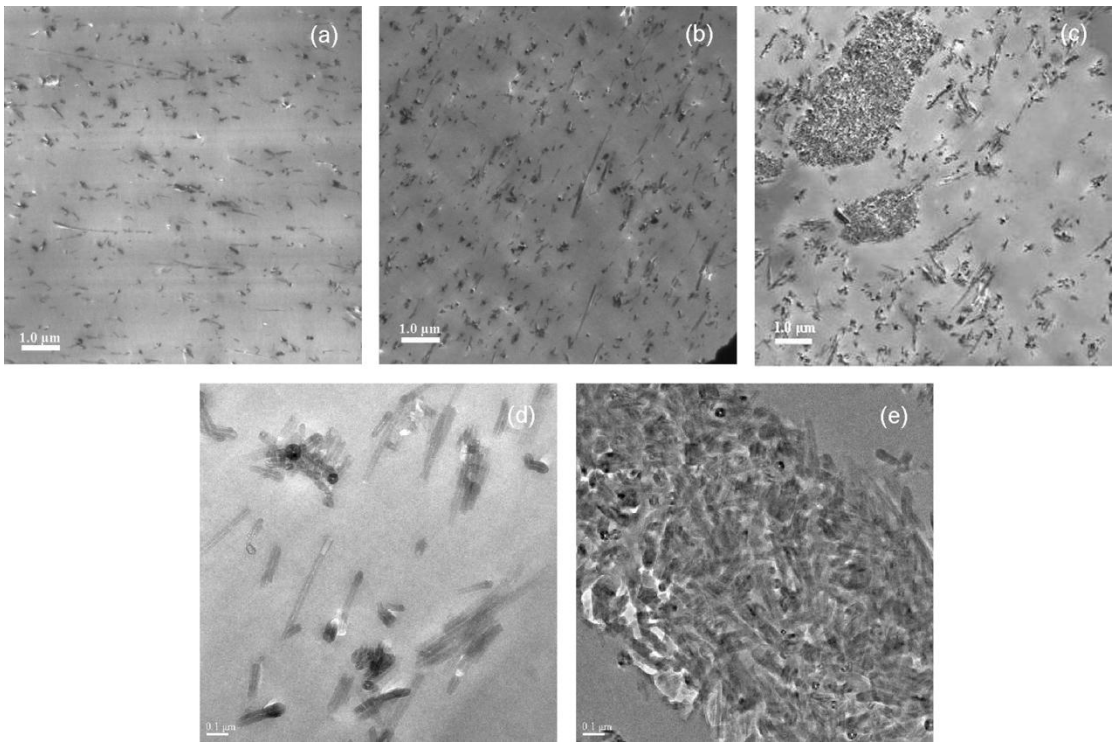

Figure 7. TEM micrographs of microtomed nanocomposites containing various nanotube loadings: (a) 2.2% (vol/vol), (b) 4.5% (vol/vol), (c) 7.7% (vol/vol) - low magnification; (d) 4.5% (vol/vol) and (e) 7.7% (vol/vol) - high magnification.

Nanocomposite films with the compositions larger than 4.5% (vol/vol) of nanotubes all revealed larger aggregates which were morphologically different from the bundles. The cross-section of the nanocomposite film containing 7.7% (vol/vol) of nanotubes is displayed in the TEM images 4c (low magnification) and 4e (high magnification). The lower magnification image clearly showed micro agglomeration of the nanotubes throughout the polymer matrix with sizes reaching up to 3 μm in addition to single nanotubes and small nanotube bundles (nano agglomeration). At higher magnification one can see that the nanotubes forming large micro aggregates are packed irregularly in contrast to the fairly parallel orientation of the nanotubes in the bundles.

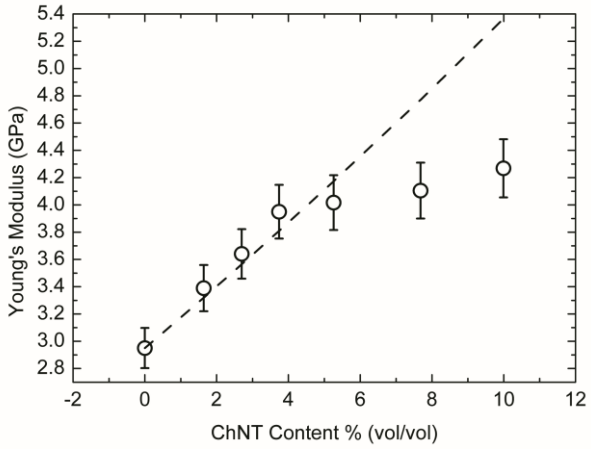

*Figure 8***.** Young's modulus of nanocomposite films as a function of volume concentration of ChNTs. Dashed line represents theoretical prediction using Eq. 3.

Young's modulus has been often employed to probe the dispersion state of various particle filled nanocomposites. Figure 8 shows the effect of ChNTs volume fraction on the nanocomposite film Young's modulus (E_c). As expected, the rigidity of ChNTs prominently enhanced the modulus of the films. At ChNTs maximum loading, about 10.0% (vol/vol), the E_c was 4.27 GPa which is 1.45 times larger than that of the unfilled PMDA-ODA film (E_m = 2.95 GPa). The increase of the modulus can be divided

into two segments: the linear, steeper increase, from 0 to about 4.0-6.0% (vol/vol) of the filler followed by the flat part which was attributed to the nanotube micro agglomeration. Noteworthy, the linear increase of E_c at lower mineral compositions was found to be in a good agreement with the calculated behavior (dashed line in Figure 8). The calculations (Eq. 3) assumed that the nanocomposites obeyed the in-plane randomly oriented discontinuous fiber lamina model.[19] The TEM results described earlier support the application of this model.

$$\frac{E_c}{E_m} = \frac{3}{8}\left(\frac{1+2(L/d)\eta_L V_f}{1-\eta_L V_f}\right) + \frac{5}{8}\left(\frac{1+2\eta_T V_f}{1-\eta_T V_f}\right) \tag{3}$$

where $\eta_L = \frac{(E_f/E_m)-1}{(E_f/E_m)+2(L/d)}$, $\eta_T = \frac{(E_f/E_m)-1}{(E_f/E_m)+2}$, E_m is the matrix modulus, E_f is the nanotube modulus, L is the length, and d is the diameter of the nanotubes and V_f is the volume fraction of the nanotubes in the nanocomposite. To calculate the moduli we used the following values: E_m = 3 GPa was measured in this work, E_f(ChNT) = 160 GPa was obtained from the literature,[20] and the nanotube aspect ratio (L/d) = 10.5 was obtained in this work. Importantly, the effect of nano agglomeration (bundle formation) on the Young's modulus seems to be rather small. The nanocomposites which contained both the single nanotubes and the bundles at lower mineral compositions show a very good agreement with the theoretical prediction based on the single nanotube dispersion state. In contrast, the micro aggregation apparently had a fairly profound effect.

A question on the physical meaning of the critical mineral composition range associated with the onset of the micro agglomeration was posed. One plausible argument considers the percolation phenomenon. It is possible that when approaching the percolation threshold the nanotubes are situated close enough to each other to interact and

this leads to micro aggregation. Mean field theories are able to estimate the critical volume fraction, V_f^p, at the percolation threshold in many cases. In particular, when the particulates exhibit a cylindrical shape, the prediction is very simple (i.e. $V_f^p = 0.6/\alpha$, where $\alpha = L/d$ is the cylinder aspect ratio).[21] Using the mean values of the geometric parameters found from the TEM analysis already discussed V_f^p = 5.7% (vol/vol) was estimated, and it is within the experimentally observed transitional composition range 4-6% (vol/vol).

Gas Barrier Behavior

Figure 9 shows oxygen flux, $J(t)$, curves obtained for various nanocomposite films. The volume fractions of ChNTs and the film thicknesses are described in the figure caption. Both the experimental data (open circles) and the fits (red lines) conducted according to Eq.2 are shown. These two-parametric fits permitted the calculation of both the permeability, P, and the diffusion coefficient, D, for each nanocomposite film while the solubility, S, was obtained from the relationship $P = D \cdot S$. The flux curves consisted of a non-steady and a steady-state region. The non-steady region is mainly determined by the diffusion coefficient and the steady-state part by the permeability coefficient. An appropriate choice of the specimen thickness typically results in good experimental resolution of the various features of the time dependence. Because of the solution casting protocol used in this work, the film thicknesses were too difficult to control leading to their variation. Some films were too thin to entirely resolve the non-steady-state part of the permeation curve with quite a few experimental data points missing in the middle, most rapid, section. This is because of the relatively long response time of the electrolytic sensor used in the OX-TRAN® 2/21 permeation instrument. Slower initial and final

(approaching the steady state) sections of the non-steady-state part of the permeation curve, however, contained sufficient number of points.

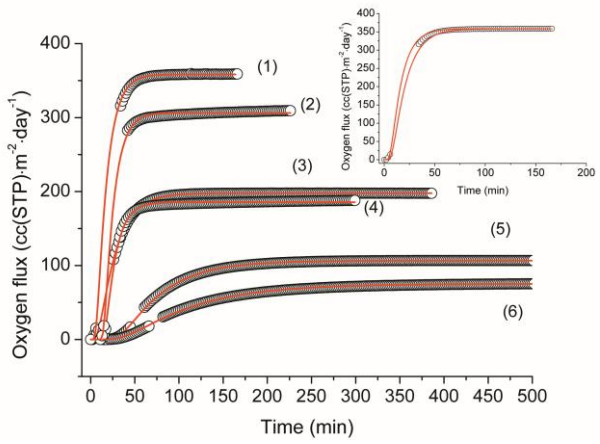

*Figure 9***.** Representative oxygen permeation curves obtained for nanocomposite films and polyimide control. Experimental data are open circles and the fits to Eq. 2 are red lines. Film mineral compositions (vol/vol) and thicknesses are indicated for the curves as follows: (1) 0% and 0.040mm; (2) 2.3% and 0.031 mm; (3) 5.3% and 0.043mm; (4) 4.5% and 0.029mm; (5) 10% and 0.074mm; (6) 4.0% and 0.072 mm.

The permeability coefficient was determined from the steady state region fairly accurately, with the uncertainty ±4%. This is essentially instrument related uncertainty and it does not arise from the fit. The quality of the curve fit to Eq. 2, however, critically controls the uncertainty of determining *D* and subsequently *S* which is calculated from *P* and *D*. Normally, the fit, when film thickness is adequate, leads to an uncertainty for *D* not larger than ±10%.[17] To illustrate that this uncertainty for *D* is also suitable here the insert is shown in Fig.6. The insert exhibits two fits of the experimental flux curve (1) which represents pure PMDA-ODA system by using the same P = 1.42 cc(STP)cm/m^2/day/atm but two different *D* values. One *D* value is 10% larger and the other is 10% smaller than the best fit value $2.3 \cdot 10^{-9}$cm^{2}s^{-1}. Clearly, the uncertainty (±10%) used here for *D* reasonably bounds the data. A question was raised if the uncertainty can become larger due to the missing points in the middle section.

Importantly, we found by fitting numerous data collections that the fit of the non-steady-state region was essentially confined by its initial and final sections which were always experimentally extant even for the thinnest films used in this work. The data in the middle section were not too important in obtaining the same fit. For instance, we calculated virtually the same diffusion coefficients with and without points in the middle section for the curves (5) and (6). Some additional data points in the middle section of these curves simply were removed by hand to prove the case.

Table 1

Oxygen and water vapor barrier characteristics of polyimide/ChNTs nanocomposites.

wt%	vol%	*P* (Oxygen) [cc(STP) cm m^{-2} day^{-1} atm^{-1}]	*P* (Water) [cc(STP) cm m^{-2} day^{-1} atm^{-1}]	*D* (Oxygen) [$10^{-9}cm^2s^{-1}$]	*S* (Oxygen) [cc(STP) cc^{-1} atm^{-1}]
0	0	1.42 ±0.06	2328 ±116	2.3 ±0.3	0.73 ±0.07
2.9	1.6	1.16 ±0.05	---	1.8 ±0.2	0.73 ±0.07
3.9	2.2	0.942 ±0.04	1597 ±80	1.6 ±0.2	0.69 ±0.07
4.8	2.7	0.905 ±0.04	1443 ±72	1.5 ±0.2	0.72 ±0.07
6.5	3.7	0.542 ±0.02	1365 ±68	1.2 ±0.1	0.54 ±0.05
7.0	4.0	0.539 ±0.02	1209 ±61	1.1 ±0.1	0.55 ±0.06
7.8	4.5	0.505 ±0.02	965 ±48	1.1 ±0.1	0.56 ±0.06
9.1	5.3	0.851 ±0.03	1463 ±73	1.6 ±0.2	0.60 ±0.06
13.0	7.7	0.849 ±0.03	1363 ±68	1.8 ±0.2	0.55 ±0.06
16.7	10.0	0.788 ±0.03	1239 ±62	2.0 ±0.2	0.45 ±0.05

Oxygen *P*, *D*, and *S* values as well as water vapor permeabilities are listed in Table 1. The water vapor measurements methodology used in this work did not permit the extraction of the corresponding diffusivity and solubility coefficients. Therefore, the permeability coefficients are only reported. The oxygen permeability coefficient of the PMDA-ODA control, 1.42 cc(STP)cm/m^2/day/atm, was found to be in a good agreement with the literature value 1.26 cc(STP)cm/m^2/day/atm.[22] The water vapor permeability of the polyimide control, 2328 cc(STP)cm/m^2/day/atm, was somewhat lower than the permeability value 3771 cc(STP)cm/m^2/day/atm we found in the literature for Kapton®.[23] It was shown elsewhere that the gas permeability of a PMDA-ODA system can be greatly affected by the synthesis method, film preparation, annealing temperature, and test conditions used.[24,25]

Figure 10 shows oxygen permeability (a), diffusivity (b) and solubility (c) of the nanocomposites as a function of ChNTs volume fraction. The figure helps to rationalize experimental data listed in Table 1. The permeability behavior roughly resembled the V-shaped trend. First oxygen permeability gradually decreased with the ChNT content reaching the minimum at 4.5% (vol/vol). The lowest oxygen permeability, 0.50 cc(STP)cm/m^2/day/atm, was 64% smaller than the one reported here for the pristine polyimide. With further increase of ChNT content, oxygen permeability partially recovered to become 0.85 cc(STP)cm/m^2/day/atm at 5.3% (vol/vol) and then remained practically unchanged. At 10% (vol/vol) (the largest ChNT content used in this work) the oxygen permeability was 0.79 cc(STP)cm/m^2/day/atm which was 45% smaller than for the pristine control. Oxygen permeability behavior of ChNT nanocomposites correlated with ChNTs dispersion and orientation which we discussed earlier in the text. At lower

ChNT compositions, the nanotubes were nanodispersed and in-plane orientated thus creating a more tortuous path for gas molecules and a higher gas barrier. However, with the onset of nanotube micro aggregation the nanotube dispersion and orientation were markedly compromised and oxygen barrier was noticeably reduced.

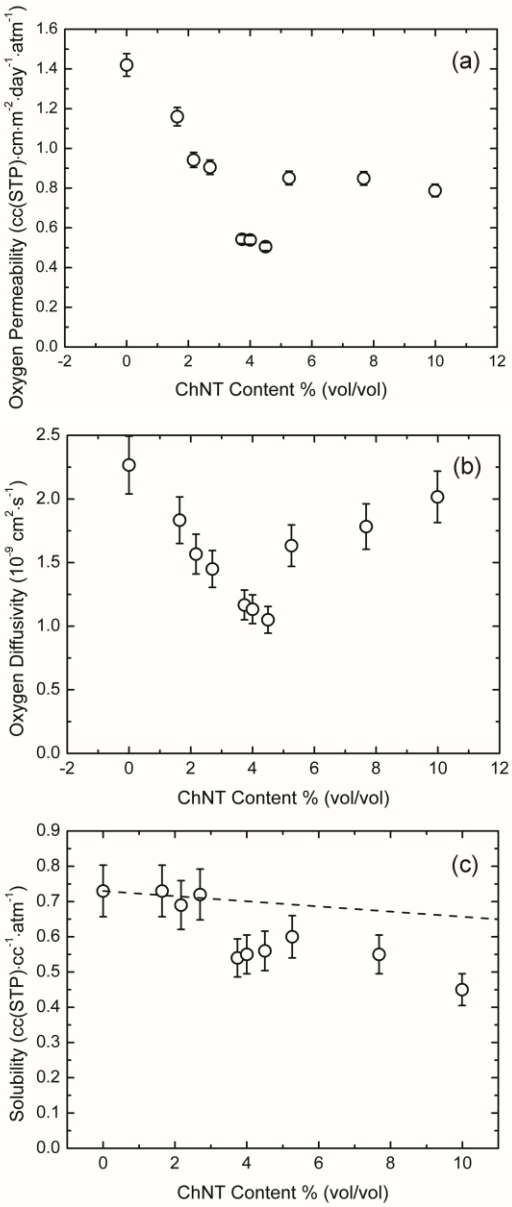

Figure 10. (a) Oxygen permeability, (b) diffusivity, and (c) solubility of polyimide/ChNT nanocomposites as a function of ChNT volume content % (vol/vol).

As $P = D \cdot S$, it was important to understand the relative contributions of the oxygen diffusivity and solubility to the permeability. The oxygen diffusivity markedly exhibited a similar to permeability V-shaped trend. The only difference was that while at higher ChNT content, 5.3-10.0% (vol/vol) ,the permeability practically remained unchanged but the diffusivity continued to increase. Therefore, the diffusivities of the PMDA-ODA control and the nanocomposite with 10.0% (vol/vol), the two ends of the V-shaped dependence, were nearly the same $(2.3 \pm 0.2) \cdot 10^{-9} cm^2 s^{-1}$ and $(2.0 \pm 0.2) \cdot 10^{-9} cm^2 s^{-1}$. The minimum diffusivity $(1.1 \pm 0.1) \cdot 10^{-9} cm^2 s^{-1}$ was also attained at 4.5% (vol/vol). It is by 52% smaller than for the pristine polyimide. Therefore, the reduction of oxygen permeability at lower ChNT content was essentially due to diffusivity while the contribution of oxygen solubility was minor. At higher ChNT content the relative contributions of oxygen diffusivity and solubility however were comparable.

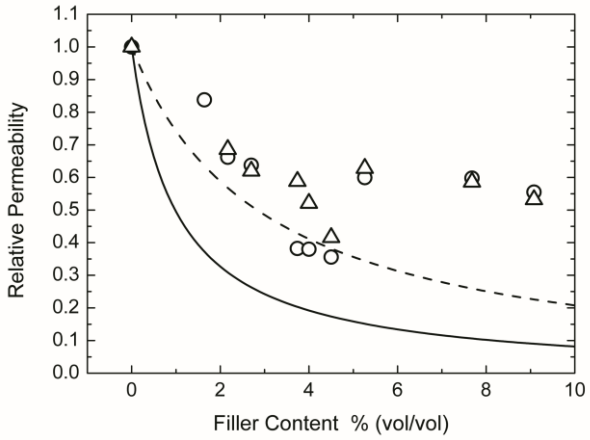

Figure 11. Relative (P/P_0) oxygen (circles) and water vapor (triangles) permeability of polyimide/ChNT nanocomposites as a function of ChNT volume content % (vol/vol). Solid and dashed lines are the Nielsen prediction of relative gas permeability of MMT based nanocomposites (Eq. 4) with s = 1 and s = 1/3 correspondingly.

The solubility trend is worth discussing in greater detail. Within the ChNT content range 0-2.7%(vol/vol) the nanocomposite solubility agreed fairly well with the

additive rule prediction $S = S_0(1-V_f)$ shown as the dashed line in Figure 10c. However, at larger ChNT content the nanocomposite experimental solubility data laid well below this line. One plausible explanation of this deviation envisions the formation of insoluble polymeric regions which are excluded (screened) within the nano aggregates (bundles) and micro aggregates. The TEM micrographs shown in Figure 7 point toward the possibility of trapping some polymeric material in between the nanotubes and within the micro aggregates. Simple calculations based on the additive prediction of solubility suggest that at the ChNT content 4.5% (vol/vol) the volume fraction of these insoluble regions can be as large as 19% of the total polymer phase and even larger, 31% at 10% (vol/vol).

Assessing water vapor permeability of the nanocomposite films was not only practically important in this study but it was fundamentally interesting to determine if the permeability of a different gas would demonstrate similar to oxygen trend. Relative, divided by the permeability of the PMDA-ODA control, permeabilities of oxygen and water vapor are shown in Figure 11 for comparison. As one can see, the two relative permeability trends virtually overlapped implying that the observed permeation behavior is real, not gas (vapor) specific, and reflects the structure variation of the nanocomposites with the ChNT content.

A question was posed regarding the efficacy of ChNTs to enhance gas barrier. As montmorillonite clay has been most commonly employed to enhance the polyimide gas barrier, two theoretical predictions of the relative permeability versus filler content% (vol/vol) were generated for MMT like platelet inclusions using the modified (includes the orientation factor) Nielsen equation (Eq. 4) to match the gas barrier efficacies of

MMT and ChNTs.[7,26,27] In Eq. 4, which assumes ultimate dispersion of individual platelets, P is the permeability coefficient of the nanocomposite, P_0 is the permeability coefficient of the neat polymer, $D/h = \alpha$ is the diameter to thickness (aspect) ratio of nanoplatelets (for MMT we assumed $\alpha = 200$) and V_f is the volume fraction of MMT, and s is the platelet orientation factor: $s = 1$ when platelets are oriented parallel to the film surface, and $s=1/3$ when platelets display random planar orientation. Solid ($s = 1$) and dashed ($s =1/3$) lines in Fig.8 represent these two definitive cases.

$$\frac{P}{P_0} = \frac{1 - V_f}{1 + s \cdot \frac{1}{2}\alpha V_f} \tag{4}$$

The nanocomposites with ultimately dispersed and oriented parallel to the film surface MMT layers exhibit higher gas barrier than the nanocomposite films containing ChNTs presented in this work. For instance at 4.5% (vol/vol) of filler the calculated permeability of MMT based nanocomposite with $s = 1$ is by 81% smaller than that for the pristine polymer as compared to 64% for the ChNT based nanocomposite. On the other hand, the nanocomposites based on ChNTs and the nanocomposites having ultimately dispersed and randomly oriented MMT sillicate layers show comparable gas barrier at least before the onset of micro aggregation of the nanotubes. Given that it is practically impossible to fabricate nanocomposites with ultimately dispersed silicate layers this result clearly indicates at the potential of ChNTs to serve as an efficient gas barrier enhancing additive. Importantly, the nanotubes do not have to be surface modified to achieve this level of gas barrier whereas MMT clay practically always requires surface modification to render its natural hydrophilicity.

In conclusion of this discussion we are set to answer a fundamental question: why high-barrier films should be expected when polymer matrix is reinforced with 1-D particulates, i.e. nanotubes, nanofibers, etc.? Also, what is the advantage of using 1-D particulates as compared to more traditional 2-D platelet like particulates? For many researchers and practitioners working in this field using 1-D particulates for gas barrier enhancement may look not as compelling. The benefit, however, may arise from the fact that nanotubes as compared to nanoplatelets are more effective in reaching the so called semidilute particle concentration regime wherein the characteristic distance between the particulates becomes comparable to their length. It is foreseen that the diffusion of a penetrant molecule in the semidilute regime becomes much more difficult, more confined and localized as compared to the dilute concentration regime in which the particles are situated on a distance far exceeding their length. In part this is because the diffusion path turns out to be considerably more tortuous and also due to the penetrant multiple reflections between the neighboring nanotubes. The last contribution important in the semidilute regime should become negligible in the dilute regime. The nature of the molecular transport localization in the composites containing 2-D platelet particulates was relatively recently theoretically described using first principles by Fredrickson and Bicerano.[28] For 1-D fibrillar inclusions similar theory is yet to be developed.

To elucidate qualitatively that nanotubes are more efficient than nanoplatelet particulates in reaching the semidilute regime the nanotube concentration regimes were quantitatively identified like in the literature,[29] using the dimensionless "dilution" parameter, $\delta_t = n_t \cdot L_t^3$, where $n_t = N_t / V_p$ is the concentration of the nanotubes (the number $N_t$of the nanotubes in the polymer volume V_p) and L_t is the nanotube length. The

dilution parameter may be envisioned as a ratio of the volume formed all together by N_t imaginary cubes with the side L to the polymer volume V_p. Evidently when δ =1 the two volumes are the same and the centers of mass of the nanotubes must on an average be situated at a distance L_t from each other. The dilute and semidilute regimes thus are respectively identified as follows: $V_f << 1$, $\delta_t << 1$, and $V_f << 1$, $\delta_t >> 1$, with the condition $V_f << 1$, $\delta_t = 1$ representing a transition from one dilution regime to another. Note that V_f is the nanotube volume fraction. Likewise the dilution parameter (as well as the dilution regimes) can be introduced for nanoplatelets, $\delta_p = n_p \cdot L_p{}^3$, where L_p is the platelet (disk) diameter. For given V_f the corresponding nanotube and nanoplatelet concentrations can be expressed like this $n_t = \frac{4V_f}{\pi L_t d^2}$ and $n_p = \frac{4V_f}{\pi L_p{}^2 h}$, where d is the nanotube diameter and h is the platelet thickness. And finally the corresponding dilution parameters for nanotubes and nanoplatelets can be expressed through their aspect ratios as follows.

$$\delta_t = n_t \cdot L_t{}^3 = \frac{4V_f}{\pi} \cdot \frac{L_t{}^2}{d^2} = \frac{4V_f}{\pi} \cdot \alpha_t{}^2 \tag{5}$$

$$\delta_p = n_p \cdot L_p{}^3 = \frac{4V_f}{\pi} \cdot \frac{L_p}{h} = \frac{4V_f}{\pi} \cdot \alpha_p \tag{6}$$

Because $\delta_t \sim \alpha_t{}^2$ and $\delta_p \sim \alpha_p$ the nanotubes will reach the semidilute regime at considerably smaller particulate volume fractions than nanoplatelets if they exhibit similar aspect ratios. To illustrate this effect in numbers the calculations have been conducted. The nanotubes with $\alpha_t \approx 10.5$ (our case) will reach the dilution regimes described by δ_t = 1 and 10 subsequently at V_f = 0.007 and 0.07. However, the nanoplatelets with $\alpha_p \approx 10.5$ will reach these two regimes at V_f = 0.08 and 0.8. The

difference is fairly dramatic. The difference becomes rather small when the nanotubes with $\alpha_t \approx 10.5$ are compared with MMT like platelets exhibiting $\alpha_p \approx 200$. These nanoplatelets will reach the dilution regimes with $\delta_p = 1$ and 10 at $V_f = 0.004$ and 0.04. This all may explain why high-barrier films can be expected when polymer matrix is reinforced with 1-D tubular particulates. Importantly, the nanotubes may not be needed to be very long and shorter nanotubes can also be quite efficient and certainly more dispersible.

Conclusions

Chrysotile nanotube containing polyimide nanocomposites were prepared via solution mixing/casting method. Nanotube dispersion in the nanocomposites was studied by TEM which at smaller mineral compositions 0-4.5% (vol/vol) showed only randomly oriented in-plane of the film single nanotubes and small nanotube bundles. Nanocomposite films with larger mineral compositions in addition exhibited micro agglomeration of the nanotubes throughout the polymer matrix with the aggregate sizes reaching up to 3 μm. Young's modulus of the nanocomposite films was measured and exhibited a strong correlation with the dispersion state of the nanotubes. The modulus gradually increased with the nanotube content first and then exhibited flattening which was attributed to the onset of micro aggregation. The discontinuous fiber lamina model was employed to describe the modulus behavior before it flattened and it showed a good agreement with the experimental data.

Oxygen permeability, diffusivity and solubility of the nanocomposite films were determined from the oxygen flux data. Oxygen permeation behavior of ChNT nanocomposites correlated well with ChNTs dispersion and orientation states. The

permeability roughly resembled the V-shaped trend with the nanotube volume composition. At smaller ChNT compositions, the nanotubes were nano dispersed and in-plane orientated thus leading to higher gas barrier. The lowest oxygen permeability found for the nanocomposites was at 4.5% (vol/vol) of nanotubes and it was 64% smaller than for the pristine polyimide. However, with the onset of nanotube micro aggregation the nanotube dispersion and orientation were markedly compromised and oxygen barrier was noticeably reduced. The reduction of oxygen permeability at smaller ChNT content was essentially due to diffusivity while the contribution of oxygen solubility was minor. At larger ChNT content however the relative contributions of oxygen diffusivity and solubility were comparable. The solubility trend at larger nanotube compositions indicated the possibility of excluded, screened within the nano aggregates (bundles) and micro aggregates, and thus insoluble polymeric regions.

Water permeability was tested in addition to oxygen permeability. When oxygen and water relative (normalized per permeability of the polyimide control) permeability versus nanotube volume composition were plotted together both trends virtually overlapped implying that the observed permeation behavior is not gas (vapor) specific and thus uniquely reflects the structural variation within the nanocomposites only.

To understand the efficacy of ChNTs to enhance gas barrier, the relative permeability of the nanocomposites containing nanotubes were compared with the trend predicted by the Nielsen formula describing the nanocomposites containing nanodispersed platelets like monmorillonite (α = 200). Nanocomposites based on ChNTs and the nanocomposites having nanodispersed and randomly oriented MMT sillicate layers showed fairly comparable gas barrier at least before the onset of micro aggregation

of the nanotubes.

Finally a question was posed regarding why high-barrier films should be expected when the polymer matrix is reinforced with 1-D particulates. It was quantitatively shown that nanotubes are more effective than nanoplatelets in reaching the so called semidilute, leading to high gas barrier, particle concentration regime wherein the characteristic distance between the particulates becomes comparable or lesser than their length. Because the dilution parameter is proportional to the square of the nanotube aspect ratio whereas it is proportional to the first power of the nanoplatelet aspect ratio, the nanotubes should reach the semidilute regime at considerably smaller particulate volume fractions than nanoplatelets when they exhibit similar aspect ratios.

REFERENCES

1. Fischer, H. Polymer Nanocomposites: from Fundamental Research to Specific Applications. *Mater. Sci. Eng., C* **2003**, *23*, 763–772.
2. Hussain, F.; Hojjati, M.; Okamoto, M.; Gorga, R. E.Review Article: Polymer-MatrixNanocomposites, Processing, Manufacturing, and Application: An Overview. *J. Compos. Mater.* **2006**, *40*, 1511–1575.
3. Yano, K.; Usuki, A.; Okada, A.;Synthesis and Properties of Polyimide-Clay Hybrid Films. *J. Polym. Sci., Part A: Polym. Chem.* **1997**, *35*, 2289–2294.
4. Bharadwaj, R. K.; Mehrabi, A. R.; Hamilton, C.; Trujilo, C.; Murga, M.; Fan, R.; Chavira, A.; Thompson, A. K. Structure-Property Relationships in Cross-Linked Polyester-Clay Nanocomposites. *Polymer* **2002**, *43*, 3699–3705.
5. Maji, P. K.; Das, N. K.; Bhowmick, A. K.Preparation and Properties of Polyurethane Nanocomposites of Novel Architecture As Advanced Barrier Materials. *Polymer* **2010**, *51*, 1100–1110.
6. Gain, O.; Espuche, E.; Pollet, E., Alexandre, M. Dubois, P.Gas Barrier Properties of Poly(ε-caprolactone)/Clay Nanocomposites: Influence of the Morphology and Polymer/Clay Interactions. *J. Polym. Sci., Part B: Polym. Phys.* **2004**, *43*, 205–214.
7. Nazarenko, S.; Meneghetti, P.; Julmon, P.; Olson, B. G.; Qutubuddin, S. Gas Barrier of Polystyrene Montmorillonite Clay Nanocomposites: Effect of Mineral Layer Aggregation. *J. Polym. Sci., Part B: Polym. Phys.* **2007**, *45*, 1733–1753.
8. Du, F.; Winey, K. I. In Nanotubes and Nanofibers; Gogotsi, Y., Ed.; CRC Press **2006**; pp 179–198.
9. Moniruzzaman, M.; Winey, K. I.; Polymer Nanocomposites Containing Carbon

Nanotubes. *Macromolecules* **2006**, *39*, 5194–5205.

10. Sanchez-Garcia, M. D.; Lagaron, J. M.; Hoa, S. V. Effect of Addition of Carbon Nanofibers and Carbon Nanotubes on Properties of Thermoplastic Biopolymers. *Compos. Sci. Technol.* **2010**, *70*, 1095–1105.
11. Song, P.; Yu, Y.; Zhang, T.; Fu, S.; Fang, Z.; Wu, Q. Permeability, Viscoelasticity, and Flammability Performances and Their Relationship to Polymer Nanocomposites. *Ind. Eng. Chem. Res.* **2012**, *51*, 7255–7263.
12. Korytkova, E. N.; Maslov, A. V.; Pivovarova, L. N.; Drozdova, I. A.; Gusarov, V. V. Formation of $Mg_3Si_2O_5(OH)_4$ Nanotubes under Hydrothermal Conditions. *Glass Phys. Chem.* **2004**, *30*, 51–55.
13. Korytkova, E. N.; Maslov, A. V; Pivovarova, L. N.; Polegotchenkova, Y. V.; Povinich, V. F.; Gusarov, V. V. Synthesis of Nanotubular $Mg_3Si_2O_5(OH)_4$–$Ni_3Si_2O_5(OH)_4$ Silicates at Elevated Temperatures and Pressures. *Inorg. Mater.* **2005**, *41*, 743–749.
14. Bessonov, M. I.; Koton, M. M.; Kudryavtsev, V. V.; Laius, L. A. In Polyimides: Thermally Stable Polymers; English translation. New York: Plenum Press; **1987**.
15. Cella, J. A. In Polyimides: Fundamentals and Applications; Ghosh, M. K.; Mittal, K. L. Eds.; Marcel Dekker Inc.: New York, **1996**, 343–367.
16. Yudin, V. E.; Otaigbe, J. U.; Gladchenko, S.; Olson, B. G.; Nazarenko, S.; Korytkova, E. N.; Gusarov, V. V.New Polyimide Nanocomposites Based on Silicate Type Nanotubes: Dispersion, Processing And Properties. *Polymer* **2007**, *48*, 1306–1315.
17. Sekelik, D. J.; Stepanov, S. V.; Nazarenko, S.; Schiraldi, D.; Hiltner, A.; Baer, E.

Oxygen Barrier Properties of Crystallized and Talc-Filled Poly(Ethylene Terephthalate). *J. Polym. Sci., Part B: Polym. Phys.* **1999**, *37*, 847–857.

18. Olson, B. G.; Decker, J. J.; Nazarenko, S.; Yudin, V. E.; Otaigbe, J. U.; Korytkova, E. N.; Gusarov, V. V.; Aggregation of Synthetic Chrysotile Nanotubes in the Bulk and in Solution Probed by Nitrogen Adsorption and Viscosity Measurements. *J. Phys. Chem. C* **2008**, *112*, 12943–12950.
19. Mallick, P. K. In Fiber-Reinforced Composites: Materials, Manufacturing, and Design, 3rd Ed.; CRC Press Taylor & Francis Group: Boca Raton, FL, **2008**; 161–164.
20. Piperno, S.; Kaplan-Ashiri, I.; Cohen, S. R.; Popovitz-Biro, R.; Wagner, H. D.; Tenne, R.; Foresti, E.; Lesci, I. G.; Roveri, N. Characterization of Geoinspired and Synthetic Chrysotile Nanotubes by Atomic Force Microscopy and Transmission ElectronMicroscopy. *Adv. Funct. Mater.* **2007**, *17*, 3332–3338.
21. Garboczu, E. J.; Snyder, K. A.; Douglas, J. F.; Geometrical Percolation Threshold of Overlapping Ellipsoids. *Phys. Rev. E: Stat. Phys., Plasmas, Fluids, Relat. Interdiscip. Top.* **1995**, *52*, 819–828.
22. Stern, S. A.; Mi, Y.; Yamamoto, H.; Clair, A. K. Structure/Permeability Relationships of Polyimide Membranes: Applications to the Separation of Gas Mixtures. *J. Polym. Sci., Part B: Polym. Phys.* **1989**, *27*, 1887–1909.
23. Pauly, S.Permeability and Diffusion Data. In Polymer Handbook, 4th Ed.; Bandrup, J., Immergut, E. H., Grulke, E. A.,Eds.; John Wiley and Sons: New York, NY, **1999**, 543–569.
24. Xu, Z. K.; Xiao, L.; Wang, J. L.; Springer, J. Gas Separation Properties of PMDA/ODA Polyimide Membranes Filling with Polymeric Nanoparticles. *J.*

Membr. Sci. **2002**, *202*, 27–34.

25. Kim, Y. K.; Park, H.; Lee, Y. M.Preparation and Characterization of Carbon Molecular Sieve Membranes Derived from BTDA-ODA Polyimide and Their Gas Separation Properties. *J. Membr. Sci.* **2005**, *255*, 265–273.
26. Nielsen, L. E. Models for the Permeability of Filled Polymer Systems. *J. Macromol. Sci. Chem. part A* **1967**, *1*, 929–942.
27. Bharadwaj, R. K. Modeling the Barrier Properties of Polymer-Layered Silicate Nanocomposites. *Macromolecules* **2001**, *34*, 9189–9192.
28. Fredrickson, G. H.; Bicerano, J. Barrier Properties of Oriented Disk Composites.*J. Chem. Phys.* **1999**, *110*, 2180–2188.
29. Fredrickson, G. H.; Shaqfeh, E. S. G. Heat and Mass Transport in Composites of Aligned Slender Fibers. *Phys. Fluids A* **1989**, *1*, 3–20.

CHAPTER IV

MICA FILLED MULTILAYERED COMPOSITES WITH ENHANCED GAS BARRIER PROPERTIES

Abstract

Multilayer coextrusion is an attractive approach for creating designed particulate-filled nanocomposite polymer film structures with enhanced gas barrier properties for typical of high viscosity, high loading systems. Organophylic mica with an aspect ratio of 1000 was used as the high aspect ratio nanocomposite filler in this research. Multilayered composites were processed with alternating layers of pure low-density polyethylene (LDPE) and mica filled linear low-density polyethylene (LLDPE) containing grafted maleic anhydride to promote particulate dispersion. Moving boundary effect is demonstrated in systems including LLDPE/LDPE multilayer systems as LLDPE, with its numerous short branches, was more mobile than the long branched LDPE polymer. Multilayered materials were annealed above melting temperature of the polymers to activate interdiffusion and to concentrate the mica platelets in the filled LLDPE layers. SEM, TEM, and WAXS analysis were employed to probe the films' layer morphology and the platelet orientation/dispersion in the nanocomposite blends and nanoparticulate filled multilayer systems. Oxygen barrier of the blends and multilayer composites were measured and related to the morphological observations. It was shown that particle concentrated multilayering leads to an enhancement in oxygen barrier properties as compared to as received multilayer materials and nanocomposite blends with the same mineral compositions.

Introduction

Layer Multiplying Process

Multilayered co-extrusion is a technique by which two or more different polymers are combined into micro or nanolayer materials with up to thousands of layers.[1] This technique can be utilized and combined with other processing techniques to improve a film's mechanical,[2,3] gas barrier[4-6] and electrical properties.[7]

The co-extrusion system used to prepare micro and nanolayered materials consist of two extruders, a series of layer multiplier elements and a film die.[8]The two extruders produce an initial bilayer flow that then travels through a series of multiplying die elements. In each element the melt is first sliced vertically, then spread horizontally, and finally recombined by stacking, doubling the number of layers with each multiplication. The total number of layers can range from tens to thousands with individual layer thicknesses from the macro to the nanoscale.

Interdiffusion of Polymers and Moving Boundary Effect

Interdiffusion behavior can be observed between contacting miscible polymers in the melt state. In a multilayer system, with a high interface to volume ratio, the interdiffusion progression is easy to observe by annealing the materials into the melt state. Multilayer concentration profiles across the layers gradually convert into a periodic gradient blend with compositional maxima located at the centers of the initial layers.[9] Interdiffusion kinetics depends on the diffusion coefficient of the contacting polymers in the layers which is directly related to the structure, composition, temperature, molecular weight, and polydispersity of the polymers. Differences in the fractional diffusion coefficients of the components will result in convective flow and movement of the initial

interface, known as the "moving boundary effect".[10, 11] Convective flow is evident by the movement of the interface towards the faster diffusing component. The moving boundary effect in microlayers was demonstrated with a miscible high density polyethylene (HDPE), low density polyethylene (LDPE) and linear low-density polyethylene (LLDPE) system.[11]The moving boundary effect was caused by relative immobility of a high molecular weight fraction of the HDPE for HDPE/LLDPE pairs and long chain branched LDPE molecules for LDPE/LLDPE pairs.

The moving boundary effect in layers can be exploited to create layered structures with highly concentrated inorganic particles. This can be achieved by filling the fast diffusing polymer layers with inorganic particles. Inorganic particle (TiO_2, nickel, and talc platelets) filled LLDPE and unfilled low-density polyethylene (LDPE) multilayer systems were studied previously[12]. When the polymer layers were interdiffused at 200 ℃ for 600 min, the inorganic particle filled layers were distinctly thinner than the initial layers, decreasing from 30 μm to about 10 μm. This lead to inorganic particle concentration in the LLDPE layers as the inorganic particles did not interdiffuse into the other polymer phase.Particle size is much bigger than the polymer chain and movement of the inorganic particles is slower.

Gas Barrier Properties of Nanocomposites

Nanoparticles are widely used to improve mechanical, electrical, gas barrier and fire retardant properties in polymer composites.[13] Analysis of polymers combined with layered silicates to form nanocomposites dates back to the 1940s with a patent application by Carter et al.[14] Clays, with their plate-like structure, and carbon nanotubes are some of the most widely used nanoparticles.[15]

Gas barrier property improvements of nanocomposites have been extensively studied with a recent interest in clay type nanoparticles.[16-18] Impermeable nanoparticles in the nanocomposites create a tortuous path for gas molecules. Permeability of the materials is a function of both the diffusivity and the solubility of the gas molecules in the polymer matrix. Since the polymer solubility coefficient is not greatly affected by the inclusion of the clay platelets, the decrease in the permeability coefficient of the nanocomposites is explained by a decrease in the diffusion coefficient. Oxygen permeability of the LLDPE/MMT composites was studied previously.[19] Modified MMT was added to the LLDPE up to 7% (wt/wt). As the content of MMT increases, the oxygen permeability decreases. For 7% (wt/wt) MMT nanocomposites permeability decreased 40% compare to the pristine LLDPE. Nazarenko and coworkers[20] studied gas barrier properties of a polystyrene-MMT system and found that the aggregation and orientation of the nanoparticles affect the barrier properties. The gas permeability is not only dependent on the volume percentage and aspect ratio of the nanoparticles, but on how the particles are orientated and dispersed in the system as well.

Yano and co-workers[16] found that with only 2% high aspect ratio mica in the polyimide system the permeability decreased by 80%; however, polyimide is a hydrophilic polymer system and they used a solution casting method. In recent literature[21], the oxygen permeability of nanocomposites of poly(ethylene terephthalate) (PET) with a synthetic mica were analyzed. Oxygen barrier properties improved by 30% with 2% (wt/wt) of mica but did not improve further with added mica content. Mica filled thermal plastic systems have also been studied previously.[22] Oxygen permeability decreases of only 30% were reported with 10% (wt/wt) mica added in the LDPE and

HDPE nanocomposites through melt blending in an extruder. The mica did not disperse well in the thermal plastic polymers without organic surface or polymer modification by adding polar groups. Poorly dispersed mica systems are not nanocomposites but microcomposites and do not show significant gas barrier property improvement.

In this study, surface modified mica were mixed with maleic anhydride grafted LLDPE systems to generate exfoliated nanocomposites. Nanocomposites were used in a multilayer system to study the moving boundary phenomenon and its effect on gas barrier properties. Alternating layers of particulate filled LLDPE and unfilled LDPE layers with widely different diffusion coefficients resulted in a movement of the initial layer interfaces toward the nanocomposite layers resulting in nanoparticle concentration in the filled layers.

Experimental

Materials

Linear low density polyethylene (LLDPE) was provided by Chemtura Corporation under the trade name Polybond® 3149. The LLDPE was modified with 1%maleic anhydride and had a melt flow index of 12-30 g/10min (ASTM D 1238). Low density polyethylene (LDPE) was provided by Dow Plastic under the trade name Dow™ LDPE 640I with a melt flow index of 2 g/10min (ASTM D 1238). The density of the LLDPE and LDPE is 0.926 g/cc and 0.9215 g/cc respectively.

Synthetic mica (Somasif ME-100) with an aspect ratio of 1000 is a synthetic fluorohectorite produced by CO-OP Chemical Co., Japan. Its structural formula can be expressed as $Na_{2x}Mg_{3.0-x}Si_4O_{10}(F_yOH_{1-y})_2$, (x = 0.15-0.5,y = 0.8-1.0). The mica has a cation-exchange capacity (CEC) of 120 meg/100g. The surface modifier used in this

study, Di(hydrogenated tallow) dimethylammonium chloride, a standard alkyl ammonium surfactant (ARQUAD 2HT-75), was provided by Sigma-Aldrich Corporation.

Mica Modification

Mica was modified via a cation exchange reaction. 1% (wt/wt) unmodified mica was dispersed in deionized water, and then the surface modifier (ARQUAD 2HT-75) was added in accordance with the CEC of the mica. After the cation exchange reaction was completed, the modified clay was filtered and dried. The original cation in the galleries was replaced by the organic cation after the reaction. The cation head was attached to the surface of the mica because the surface of the Mica is negatively charged. The organic tail was in between the two mica layers to further separate the layers.[23] Wide Angle X-Ray Diffraction (WAXD) (Rigaku Ultima III) was used to determine the d-spacing of the modified mica. The diffraction patterns were recorded at scattering angles (2θ) from 1 ºto 15 °at a scanning rate 0.5 º/min. Modification of the mica was also confirmed by TGA (TA Q500). The TGA was performed in nitrogen atmospheres at 10 ℃/min intervals up to 800 ℃. Mica and modified mica were dried in the vacuum oven at 90 ℃ for 10 hours prior to testing.

Nanocomposites Preparation

Modified mica was blended with LLDPE using PRISM TSE 16TC twin-screw extruder at 200 ℃ and 50 rev/min screw speed. The pelletized LLDPE was mixed uniformly at dry conditions with mica powder before melt blending in the extruder. The mixture of LLDPE and mica was added to the feeder of the extruder and the polymer was mixed with the nanoparticles in the molten state during the extruder process. The composites from extruder were pelletized and dried in the oven at 90 ℃ for 2 hours.

LLDPE-mica nanocomposites with 0-15% (wt/wt) mica composition were prepared. All of the composites were passed through the extruder 3 times to achieve optimal dispersion of mica in the polymer.

WAXD was used to analyze the dispersion of nanoparticles in the nanocomposites. The nanocomposites were scanned at diffraction angles (2θ) from 1 ºto 10 ºat a scanning rate of 0.5 º/min. The mica d-spacing can be estimated by Bragg's law:

$$d = \frac{\lambda sin\theta}{2} \quad (1)$$

where d is basal spacing, λ is wavelength of the X-ray beam and θ is the diffraction angle of incidence. The radiation has the wavelength 1.54 Å.

Transmission Electron Microscopy (TEM) (JEOL Ltd. JEM-2100) was performed at 200kV on the nanocomposites to analyze dispersion of the mica in the nanocomposites. The specimens were cryo-microtomed in thin sections of 70-100 nm and placed on a copper grid with no staining agents.

Multilayer Materials Preparation

Multilayers with alternating layers of LDPE and LLDPE/mica were extruded using a continuous layer-multiplying co-extruder at Case Western Reserve University. By varying the melt feed ratio, the film thickness, number of layers, and the individual layer thicknesses can be precisely controlled. The extrusion rates were regulated to obtain a 1:1 ratio of the components. The films in this study had a thickness of approximately 400 μm, 17 and 65 layers, and individual layer thicknesses of 30 and 5 μm respectively. The extruding temperature was 200 ℃. LDPE and LLDPE/mica viscosities matched at this temperature.

The multilayer materials were annealed in the oven while confined with a metal mold in a nitrogen atmosphere. Nitrogen was used to prevent the degradation of the polymers. The annealing temperature of the multilayer films was 200 ℃ and annealing times were30 min, 60 min, 5 hours, 10 hours and 30 hours. The films were covered by Teflon sheets on the top and bottom to preserve the films' smooth and uniform surface. The films were quenched in a water bath after annealing.

The Mica dispersion in the multilayered materials before and after annealing was analyzed using WAXD. WAXD was necessary to quantify if the multiplying and annealing affected the dispersion of the nanoparticles. TEM was also used to analyze the dispersion and orientation of the mica in the multilayered systems before and after annealing. Scanning Electron Microscopy (SEM) was performed using a FEI Quanta 200 SEM. SEM was utilized to analyze layer thicknesses in the multilayer materials before and after annealing. The cross sections of these materials were cryo-microtomed and sputter coated using gold particles prior to the SEM test.

Gas Barrier Test

Oxygen barrier properties of the nanocomposites and multilayered materials were measured at 25 ^{o}C, 0% RH and 1 atm partial oxygen pressure difference using commercially manufactured diffusion apparatus OX-TRAN® 2/21 ML (MOCON). The specimens were kept in vacuum desiccators for over 12 hours before testing. Conditioning in nitrogen inside the permeation unit was needed to remove traces of atmospheric oxygen and water. Afterward, pure oxygen gas was introduced into one side of the test cell as the driving force for permeation is a difference in the partial pressure of oxygen. The oxygen diffuses into the film and passes through the other side of the film

where nitrogen sweep gas carries the oxygen to the detector. The oxygen flux curves were developed when the sensor detected oxygen gas on the other side of the film.

As the oxygen concentration in the film reaches a constant distribution, the flux approaches the steady-state value J. Fick's Second Law is used to fit the flux curves,

$$J(t) = \frac{Pp}{l}[1 + 2\sum_{n=1}^{\infty}(-1)^n \exp(-\frac{D\pi^2 n^2 t}{l^2})] \quad (2)$$

where$P$ is oxygen pressure, p is partial pressure, l is thickness of the film and t is the time. P can be calculated using the steady-state flux value $P = Jl / p$ .From the fitting of the flux curve, the diffusivity (D) can be obtained. Solubility(S) can be obtained from the relationship $P = DS$.

Results and Discussion

Mica Analysis

High aspect ratio mica are plate-like shaped nanoparticles with 1 nm thickness (h) and about 1000 nm diameter (d). The mica is in white fine powder form at room temperature. TEM images of mica and modified mica are shown in Figure 12. Mica showed irregular plate-like shapes and several mica layers are stacked together. The TEM sample was made by dispersing mica in ethanol at low concentrations, followed by solvent evaporation. The surface of the layer is negatively charged and there are exchangeable cations between the layers. Figure 12(b) shows the surface modified mica with the same magnification. After surface modification, mica surfaces become more hydrophobic and more difficult to disperse in the ethanol. The diameter and shape of the mica didn't change after modification based on the TEM images.

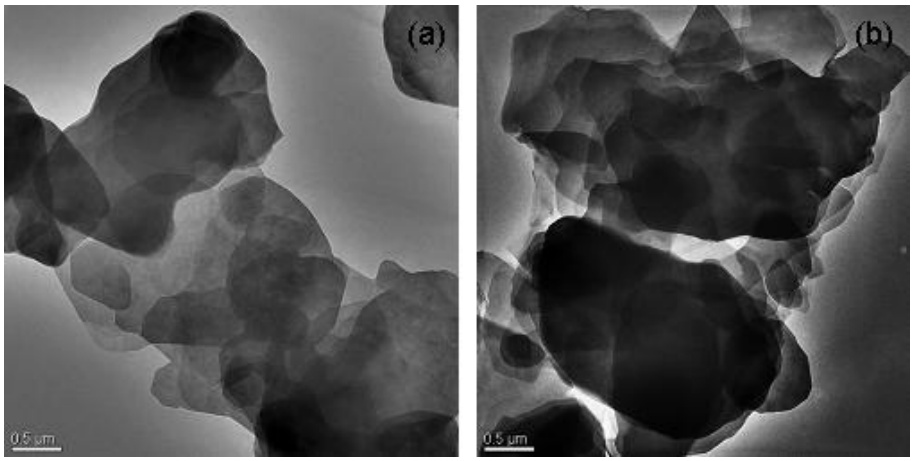

Figure 12. TEM of (a) mica and (b) surface modified mica.

More than 10 TEM images were analyzed to quantitatively compare the diameter of the mica before and after surface modification. At least 100 mica particles were measured for each graph to generate diameter histograms. Figure 13(a) shows the diameter histogram of mica before surface modification and Figure 13(b) shows the diameter histogram of surface modified mica. The mica diameter is generally in the range of 0.5 μm and 3 μm. It shows that about 60% of the particles have diameters between 0.6 μm and 1.2 μm in both the unmodified and modified mica. The average diameters of the mica and the surface modified mica are 1.24 μm and 1.03 μm, respectively. From the histogram, one can clearly see that the mica diameter is around 1 μm and that the mica did not break down into small pieces during the surface modification reaction.

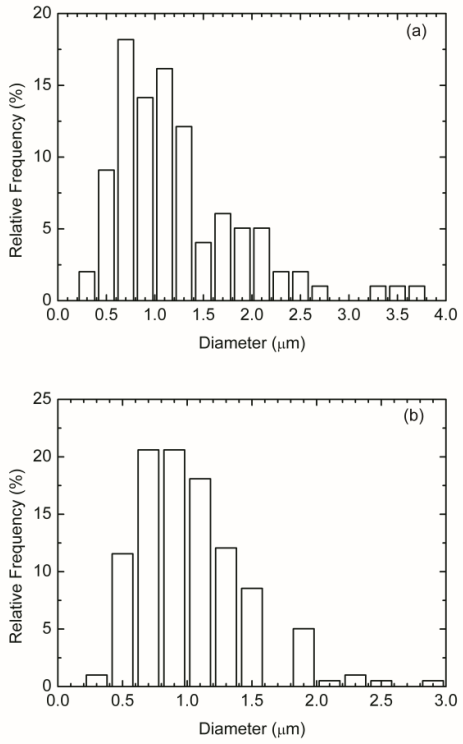

*Figure 13***.** Comparison of length histogram of (a) mica and (b) surface modified mica.

Mica is not easily dispersed in most polymers, especially organophilic polymers, due to the surface chemistry and preferred face-to-face stacking.[24] However, replacement of the inorganic cations in the galleries of the clay by alkylammonium surfactants not only improves compatibility of the surface of the clay and the hydrophobic polymer matrix, but also expends the clay galleries.[25] Mica was modified by Di(hydrogenated tallow) dimethylammonium chloride which is an organic ion with long alkyl chains. The modification can be detected using WAXD and TGA.

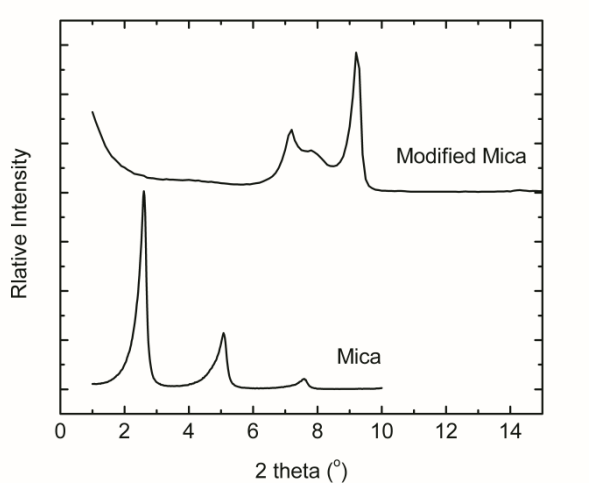

*Figure 14***.** Wide angle X-ray diffraction of synthetic mica before and after surface modification.

WAXD was utilized to measure the d-spacing between the mica layers and an increase in d-spacing is observed after the surface modification reaction. Figure 14 shows the WAXD of mica before and after modification. Unmodified mica has a 2θ peak at about 10 degrees and other peaks that may be caused by free water absorption. The peaks of modified mica shifted to lower angle values. Bragg's law can be used to calculate the interlayer spacing between the mica layers. The basal spacing of the mica is about 1 nm before surfactant modification and increased to 3.4 nm after modification.

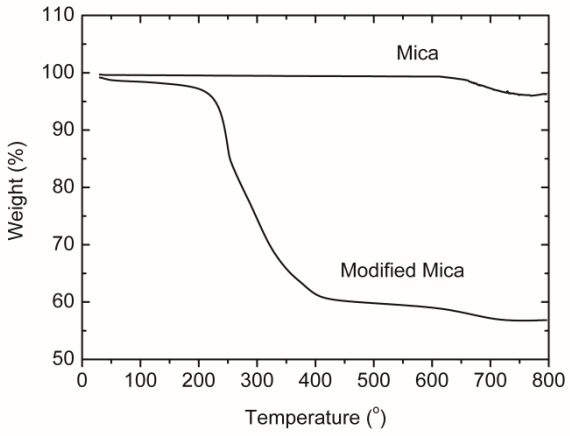

*Figure 15***.** TGA of synthetic mica and surface modified mica at nitrogen atmosphere.

TGA of mica and modified mica are shown in Figure 15. Modified mica has lower thermal stability compared to the unmodified mica because the organic modifier is not stable at high temperatures. There is no weight loss at 200-600 ℃ for mica and only 5% weight loss when heated to 800 ℃ in a nitrogen atmosphere. However, the modified mica had about 46% weight loss upon heating to the same temperature. The degradation temperature of the modified mica is about 250 ℃. LLDPE and Mica were extruded at 200 ℃, so the organic modifier is stable at this temperature. The organic modifier content is about 44% by weight based on the TGA final residue at 800 ℃.

Dispersion of Mica in Nanocomposites

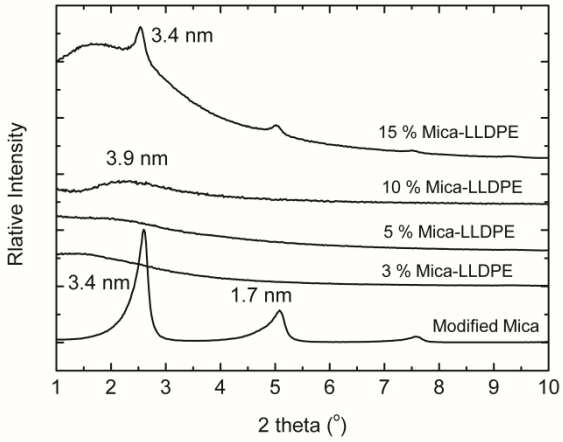

*Figure 16***.** Wide angle X-ray diffraction of mica and Mica-LLDPE composites.

Modified mica was extruded with LLDPE at 200 ℃ and a screw speed of 50 rev/min during 3 passes through the extruder. Twin screw extruders are commonly used for polymer processing because the high shear force can separate the platelet layers. The LLDPE contained 1% maleic anhydride by weight which can work as a compatibilizer between hydrophobic polymers and hydrophilic nanoparticles to help the dispersion of the particles in the polymer matrix. Nanocomposites with 3, 5, 10 and 15% (wt/wt) modified mica were processed for analysis.

The WAXD studies provided information on the dispersion state of the mica. In poorly dispersed mica filled polymeric systems, the polymer chains are not intercalated into the mica galleries and d-spacing is not altered from that of the original modified mica. Intercalated systems can be achieved by penetration of the polymer chains into the mica galleries, resulting in diffraction peak movement towards lower angles. Polymer chains force the mica sheets separate from each other and when the distance is far enough, exfoliated nanocomposites can be achieved. Typically no diffraction peaks can be observed for fully exfoliated nanocomposites.

Figure 16 shows the WAXD of nanocomposites with different content of mica. Nanocomposistes with 3 and 5% (wt/wt) mica show really small diffraction peaks. This is because the mica is almost fully exfoliated into the polymer matrix in the low concentration nanocomposites systems. The diffraction peak for the 10 % (wt/wt) mica composites moved toward a lower angle value and the diffraction strength is decreased due to the system being in a state of a combination of intercalated and exfoliated phases. For the 15% (wt/wt) mica composites, diffraction peaks (2θ) at 2 ºand 2.5 ºcan be observed which indicate that both intercalated and poorly dispersed aggregates exist in the system. Mica was close to exfoliation in the composites with low mica content, however, intercalated and aggregated mica still can be observed in the higher concentration mica composites where more shear force and better extruding conditions are needed to better disperse the mica.

WAXD shows the average dispersion of the mica in the LLDPE, however, it is difficult to be conclusive on the orientation, distribution, and shape of the mica particles. Furthermore, it is difficult to determine the existent of large aggregates from WAXD

analysis. TEM can be used to better describe the dispersion of the mica in the polymer matrix to be combined with the WAXD data. TEM provides a direct visual depiction of the composites' structure. Figure 17 shows the LLDPE-mica composites with 5% (wt/wt) modified mica. The composites were cryo-microtomed to 100 nm thick sections before testing. Figure 17(a) shows the overall dispersion of mica in selected area and Figure 17(b) shows a higher magnification of an area on the previous TEM image where the individual particles and their arrangement can be seen more clearly. From the TEM images it appears that the mica is well dispersed in the polymer matrix and both single layer mica and small stacked mica layers were observed. Mica particles are orientated in the direction parallel to the film surface. Compression molding of nanocomposites contributes to the orientating of the particles in the polymeric systems at melting state. The result of TEM and WAXD both showed that composites with 5% (wt/wt) mica were a combination of primarily exfoliated platelets and some intercalated stacks.

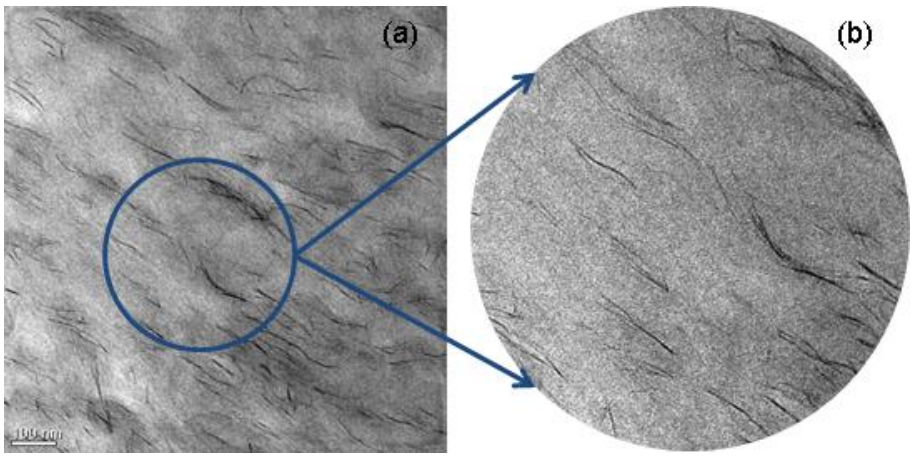

*Figure 17***.** TEM of 5% (wt/wt) LLDPE-mica nanocomposites at (a) low magnification and (b) high magnification.

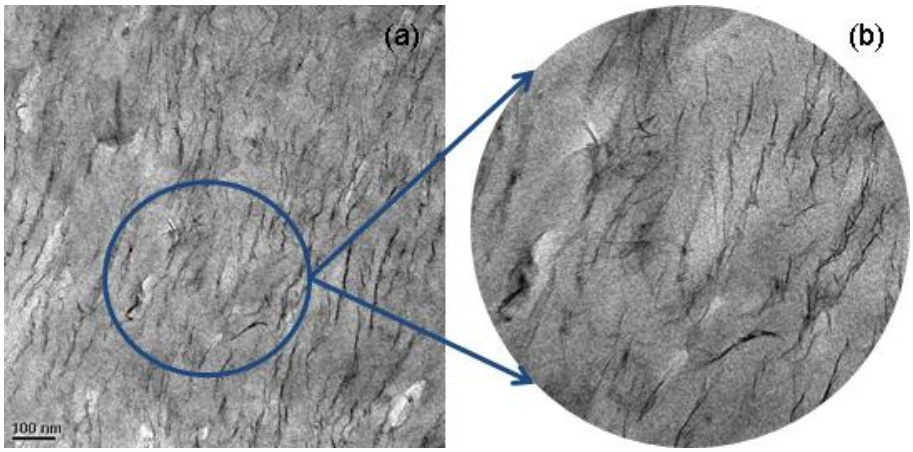

*Figure 18***.** TEM of 10% (wt/wt) LLDPE-mica nanocomposites at (a) low magnification and (b) high magnification.

Figure 18 shows TEM image of the 10% mica-LLDPE composites, representing high mineral content system. Individual layers were hardly visible on the image and a large amount of aggregates were observed through the whole film. Aggregates contained several mica layers in which the mica layers were tilted and bent. The interlayer spacing was fairly heterogeneous. Mica aggregates showed orientation in the direction parallel to the film surface. The X-ray diffraction showed only one small peak (d = 3.9) which reflects intercalation of the mica, however, TEM shows mixture of intercalated and coherent layer stacking structures.

Complete dispersion of mica is needed to optimize gas barrier property improvement as evident by the poorly dispersed systems not showing the enhancement of previously studied nanocomposite systems[13]. In order to improve gas barrier properties effectively either 3% or 5% mica nanocomposites would be used for further studies in multilayered systems.

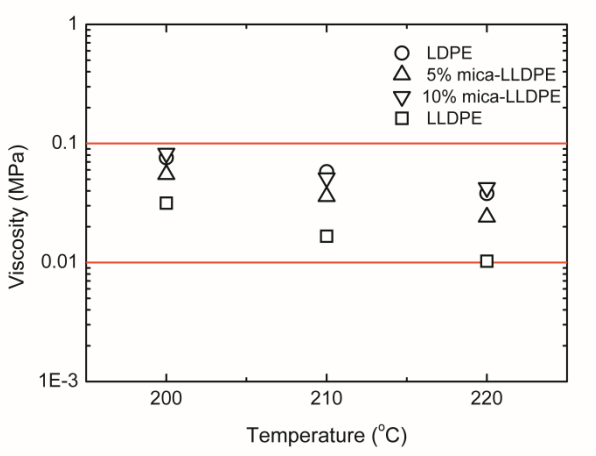

*Figure 19***.** Viscosity of LDPE, 5% mica-LLDPE and 10% Mica-LLDPE nanocomposites at temperature 200, 210 and 220 ℃ to show the multilayer processing window.

The viscosities as a function of temperature of the pure polymers and composites are shown in Figure 19. Viscosity analysis can be used to identify the optimal multilayer processing temperature, where the materials would have similar viscosity. In a system of materials with mismatched viscosities, the material with the lowest viscosity tends to encapsulate the other material, leading to interfacial instabilities. As shown in the Figure 19, pristine LLDPE has a much lower viscosity as compared to the LDPE. The viscosity gap was designed on purpose because the mica particles increase the viscosity of the LLDPE system. The viscosity of the 5% LLDPE-mica is slightly lower compared to the LDPE and the 10% LLDPE-mica is matched with LDPE. However, as mentioned previously, mica is better dispersed and exfoliated in 5% mica composites than in 10% mica composites. So, 5% mica-LLDPE systems and LDPE were chosen to make multilayer materials with the proper extruding temperature.

Multilayer materials

Multilayer materials were fabricated using a co-extruder that contains alternating layers of LDPE and 5% (wt/wt) mica LLDPE nanocomposites. Multilayer materials were

designed to have a total number of layers of 17 and 65 layers. Multilayer materials had a total thickness of about 300-400 μm and a width of 15 cm. The top and bottom layers are both LDPE layers with half the thickness of the inner layers. The 17 layer and 65 layer multilayer materials had single layer thicknesses of 20 μm and 5 μm, respectively.

The multilayer materials were annealed at 200 ℃ for different times to induce interdiffusion of the polymers. There are three factors that affect the properties of multilayer materials: layer uniformity, nanoparticle dispersion and the moving boundary effect. Layer uniformity constitutes no layer breakage or large thickness variance between layers. Nanoparticle dispersion is very important for gas barrier properties. Although exfoliated nanocomposites were used in multilayering, nanoparticle dispersion and orientation may change during multilayering or annealing in the melt state. For example, when the layer thickness is comparable with the particle diameter, particle reaggregation may occur. The moving boundary effect can concentrate the particles in the nanopaticle filled layers and may help to improve gas barrier and fire properties.

DSC was used to measure the melting temperature of the LDPE, 5% mica-LLDPE, and LLDPE-mica/LDPE multilayer materials before and after annealing as shown in Figure 20. The melting temperature of the LDPE is 111.2 ℃ and the melting temperature of the LLDPE is 121.4 ℃. LDPE has lower melting temperature than LLDPE because of structural differences. 65 layers of LLDPE-mica/LDPE multilayer materials had two melting peaks with maxima at 109.8 ℃ and 117.4 ℃ which corresponds to the LDPE and mica-LLDPE layers. The melting peaks shifted toward each other and were broadened when compared to the peaks of the LDPE and mica-LLDPE single layer materials which implies that the interdiffusion process may have already

started during the multilayering process. For 17 layers, there is only one peak at 110.7 ℃ and a shoulder at about 117 ℃. This may also indicate that the interdiffusion of LDPE and LLDPE had already started during the multilayering process. DSC of the multilayer materials after annealing shows two melting peaks at 111.2 ℃ and 115.1 ℃, however, they appear to be different than the melting peaks of the unannealed materials for both 17 and 65 layers. The two melting peaks are really close to each other and almost combined into one peak. Interdiffusion of the LDPE and LLDPE into each other caused the peak shift and combination. The two layers were still not totally mixed, because two separate peaks can still be observed from the DSC curves.

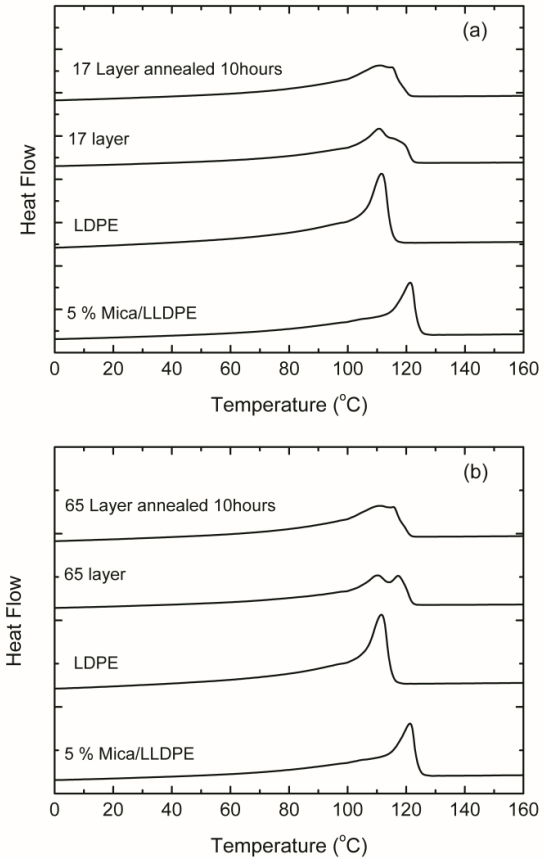

Figure 20. DSC of LDPE, 5% mica-LLDPE nanocomposites and (a) 17 layers and (b) 65 layers multilayerd materials before and after annealed for 10 hours at 200 ℃.

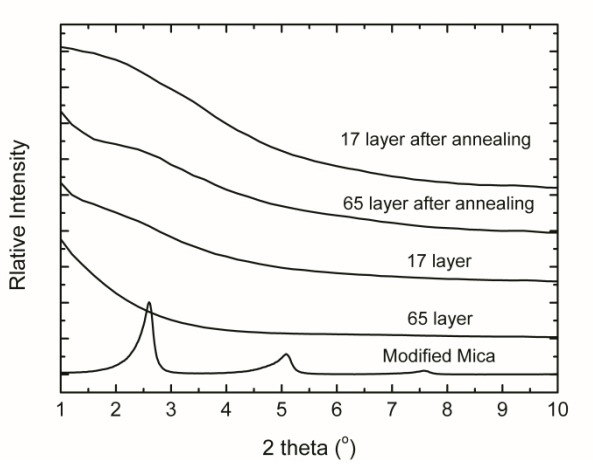

Figure 21. Wide angle X-ray diffraction of surface modified mica, 65 layers and 17 layers multilayer materials before and after annealed for 10 hours at 200 ℃.

As mentioned previously, particle reaggregation may affect permeability and the multilayering process may affect the dispersion of mica. TEM and WAXD can be used to observe the dispersion of the mica particles in the multilayer systems. Figure 21 showed WAXD of the multilayer materials before and after annealing for 17 and 65 layers. These multilayer materials before annealing did not show any obvious diffraction peaks, meaning there is no particle reaggregation upon multilayering. The multilayer materials after annealing showed shoulders at $2\theta = 2.5$ º. This may be caused by small amount of particle reaggreation during the annealing process. LLDPE and LDPE diffuse into each other when annealing at high temperatures and may compress the mica particles to form aggregates. The other possibility is that the surface modifier of the mica degraded at the annealing temperature and caused the mica particle reaggregation.

TEM was used to further confirm the structure of the mica in the multilayer materials as showed in Figures 22 and 23. Figure 22 shows the cross section of the 17 layer multilayer materials before and after annealing. Figure 22(a) and (b) show different parts of the multilayer material before annealing. Figure 22(a) shows both the LDPE and

LLDPE-mica layers and the boundary can be clearly observed. The mica appears well dispersed and only a small amount of intercalated structures were observed near the boundary of LLDPE-mica and LDPE layers. Orientation of the mica parallel to the film surface can be attributed to the fact that the high aspect ratio mica can be rotated and aligned by the moderate shear forces that arise as the melt spreads out in the press. In both compression molded composites and multilayered material, an ordered structure of mica particles can be observed. Figure 22(b) shows the structure of mica in the bulk of the LLDPE-mica layers. The dispersion and orientation are similar to that in Figure 22(a), except a less intercalated structure of mica observed.

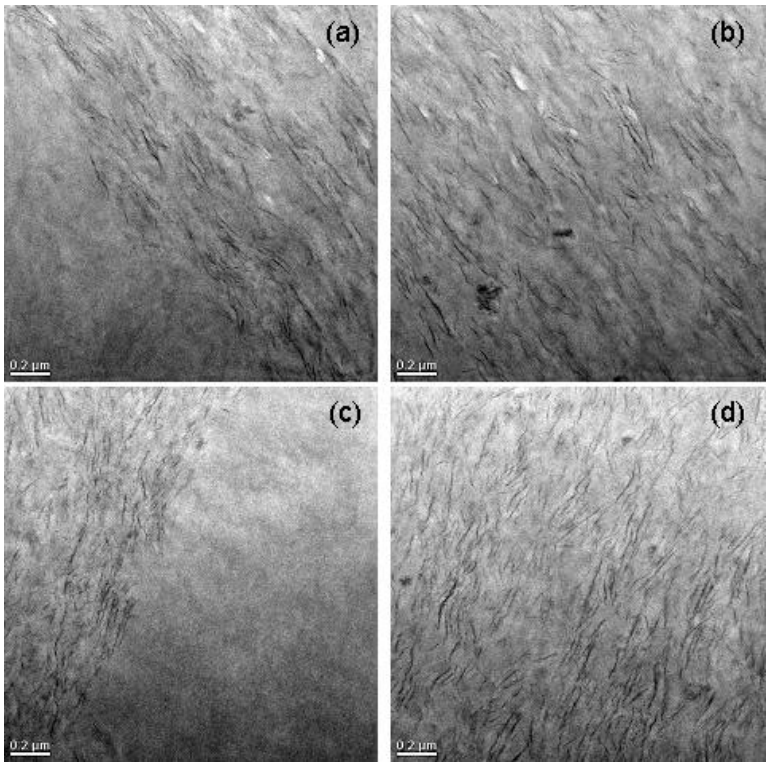

*Figure 22***.** TEM of 17 layers of 5% mica-LLDPE/LDPE multilayer material (a) and (b) before annealed (c) and (d) after annealed at 200 ℃ for 10 hours. (a) and (c) shows both of the LDPE layer and LLDPE-mica layers and (b) and (d) shows bulk of the LLDPE-mica layers.

Multilayer materials with 17 layers after annealing are shown in Figure 22(c) and (d). Figure 22(c) shows both the LDPE and LLDPE-mica layers and Figure 22(d) shows the bulk of the LLDPE-mica layers. The mica near the LDPE layers shows some intercalation or concentrated regime which may be caused by the moving boundary effect between the LLDPE-mica and LDPE layers. LLDPE polymer chains intercalated between the mica layers escaped from the layers and diffused into LDPE layers which caused a densification of mica near the edges of the LLDPE-mica layers. The concentration of mica did not obviously increase in the bulk of LLDPE-mica layers as shown in Figure 22(d). LLDPE in the bulk of the layers may not be able to diffuse into the LLDPE because of the concentrated mica at the edges of the layers preventing the LLDPE from diffusing out of the layers.

Figure 23 shows the 65 layer multilayer materials before and after annealing. Figure 23(a) and (b) show different parts of the layers for both the LDPE and LLDPE-mica layers in the TEM images. Orientation of the mica can be observed for the 65 layers system, with mica still well dispersed in the LLDPE layers. The 65 layer multilayer materials have an individual layer thickness of about 5 μm. The average mica diameter (1μm) is in the same range as that of the individual layer thicknesses of the 65 layers multilayer materials. Particles tend to lose their orientation and reaggregate when the layer thickness is close to the particle size. However, reaggregation or a change in orientation of the mica was not evident after the multilayering process. The dispersion of mica in the 17 layer and 65 layer systems appear very similar.

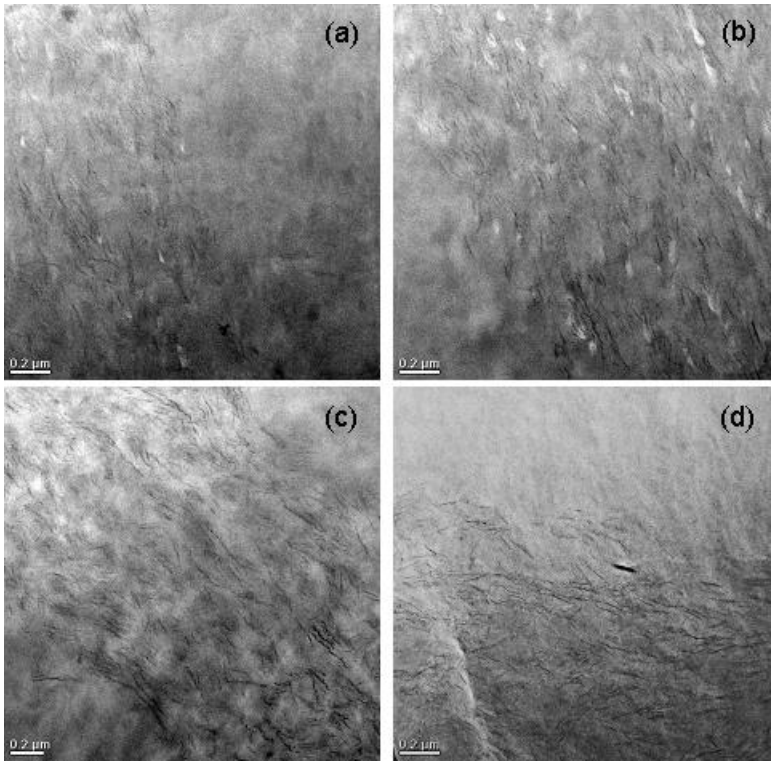

*Figure 23***.** TEM of 65 layers of 5% mica-LLDPE/LDPE multilayer material (a) and (b) different part of the films before annealed (c) and (d) after annealed at 200 ℃ for 10 hours.

Figure 23(c) and(d) show the 65 layer materials after annealing. Mica also condensed at the edge of the layers forming a mica concentrated area as also observed in the 17 layer system. An entire LLDPE-mica layer can be seen for the annealed 65 layers while only part of the LLDPE-mica layers can be seen for 65 layers before annealing at the same magnification. The layer thickness decreased to about 2 μm from 5 μm after annealing due to the moving boundary effect. However, one cannot quantify the moving boundary effect based on the TEM picture taken from really small area of the film cross section. The layer thickness may vary from one layer to another and the thinner layer may not have been generated by the moving boundary effect. SEM is better way to observe the layer thickness changes than TEM because SEM can clearly show multiple layers at a lower magnification.

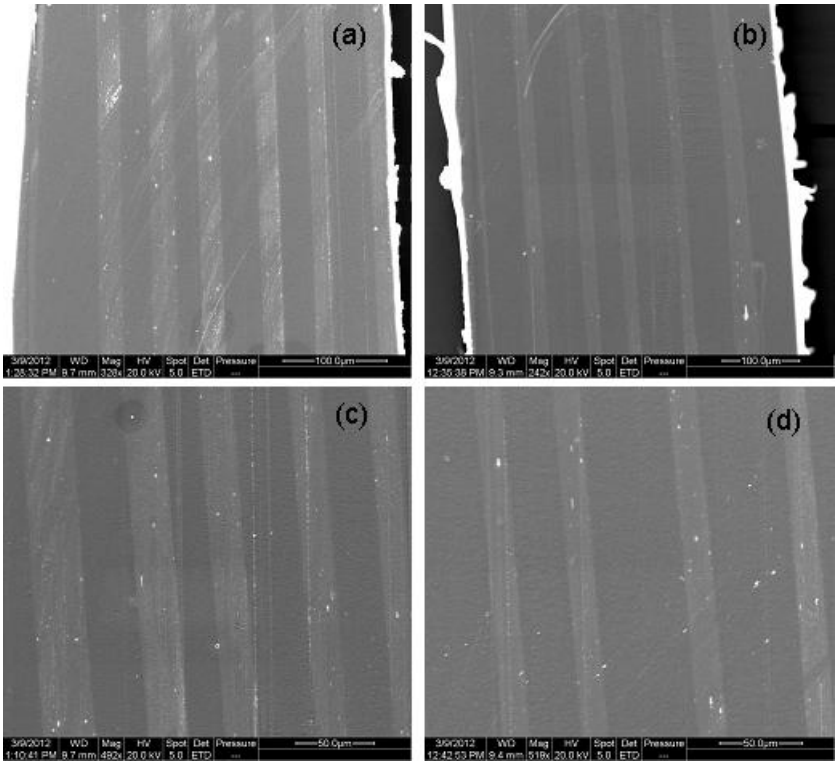

Figure 24. SEM of the 17 layers 5% mica-LLDPE/LDPE multilayer materials (a) and (c) before and (b) and (d) after annealed at 200 ℃ for 10 hours at different magnification.

Layer structures were observed using SEM by looking at the cross section of the multilayer films. Figure 24(a) and (c) show SEM images of the 17 layer multilayer materials with different magnifications before annealing. The white layers are the mica filled LLDPE layers with an average thickness of 22.6 μm while the black layers are the LDPE layers with an average thickness of 31.4 μm. LDPE and LLDPE-mica were fed at an 1:1 ratio during the multilayer process, however, the thickness of LLDPE-mica layers and LDPE layers are slightly different. This may be caused by the interdiffusion of the LLDPE and LDPE layers and the moving boundary effect during the multilayering process.

Table 2

Thicknesses total layers, LDPE layers and LLDPE-mica layers of the multilayer materials before and after annealed for 30 min, 1 hour and 10 hours at 200 ℃.

	Total Thickness (μm)	Filled Layer Thickness (μm)	Unfilled Layer Thickness (μm)
Mica-LLDPE/LDPE 17 layers before anneal	390	22.6 ±4.4 (0.42)	31.4 ±5.8 (0.58)
Mica-LLDPE/LDPE 17 layers 30min anneal	393	16.6 ±2.3 (0.30)	38.4 ±7.3 (0.70)
Mica-LLDPE/LDPE 17 layers 1h anneal	373	15.4 ±1.7 (0.30)	38.3 ±8.3 (0.70)
Mica-LLDPE/LDPE 17 layers 10h anneal	400	16.7 ±2.6 (0.27)	46.3 ±8.1(0.73)
Mica-LLDPE/LDPE 65 layers before anneal	320	5.1 ±2.4 (0.49)	5.4 ±1.2 (0.51)
Mica-LLDPE/LDPE 65 layers 30min anneal	333	3.2 ±1.4 (0.35)	6.0 ±2.9 (0.65)
Mica-LLDPE/LDPE 65 layers 1h anneal	310	3.3 ±1.3 (0.32)	6.8 ±3.3 (0.68)
Mica-LLDPE/LDPE 65 layers after anneal	310	3.0 ±1.5 (0.28)	7.7 ±2.1(0.72)

The thickness of the LLDPE-mica layers was reduced after being annealed for 10 hours while that of the LDPE layers increased as shown in Figure 24(b) and (d). LLDPE is a short chain branched linear polymer and LDPE is a long chain branched polymer contributing to their different mobilities and diffusion coefficient in the melt. Differences in the fractional diffusion coefficients of the components result in a convective flow and

movement of the initial interface toward the faster diffusing material. Layer thicknesses and relative layer thicknesses (thicknesses of the LLDPE-mica or LDPE verses the sum of the two layer thicknesses) are shown in the Table 2. The average LLDPE-mica layer thickness decreased from 22.6 μm to 16.7 μm and the LDPE layer thickness increased from 31.4 μm to 46.3 μm. The concentration of mica was estimated to have increased to about 8% (wt/wt) based on the depletion of LLDPE in the nanocomposite layer.

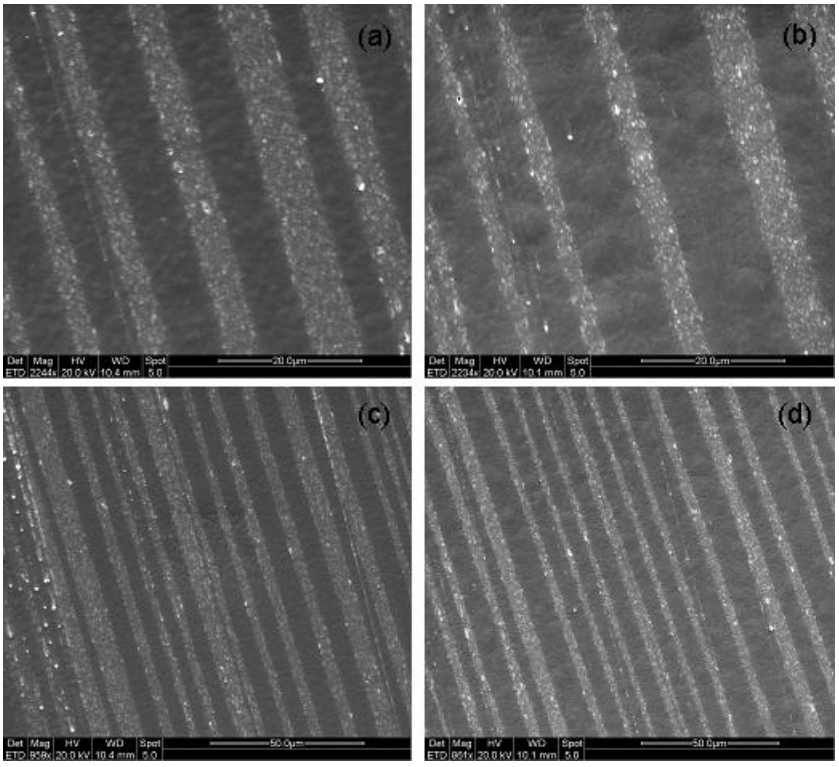

Figure 25. SEM of the 65 layers 5% mica-LLDPE/LDPE multilayer materials (a) and (c) before and (b) and (d) after annealed at 200 ℃ for 10 hours at different magnification.

Figure 25 shows an SEM image of the 65 layer multilayer material before and after annealing with two different magnifications. Both LLDPE-mica and LDPE layers have large variation in thickness. The average thicknesses of the LLDPE-mica and LDPE layers are 5.1 and 5.4 μm before annealing, respectively. The average thickness of the LLDPE-mica and LDPE layers are 3.0 and 7.7 μm after annealing. The interdiffusion and

moving boundary effect caused a change in layer thicknesses for both the 17 and 65 layer multilayer materials to a thickness ratio of LLDPE to LDPE 3:8 after annealing. As mentioned previously, the moving boundary effect stopped at some point, not reaching super thin layer of LLDPE-mica layers. This could possibly be attributed to the mica concentration increase at the edge of LLDPE-mica layers which hindered the LLDPE from further diffusing into the LDPE layers.

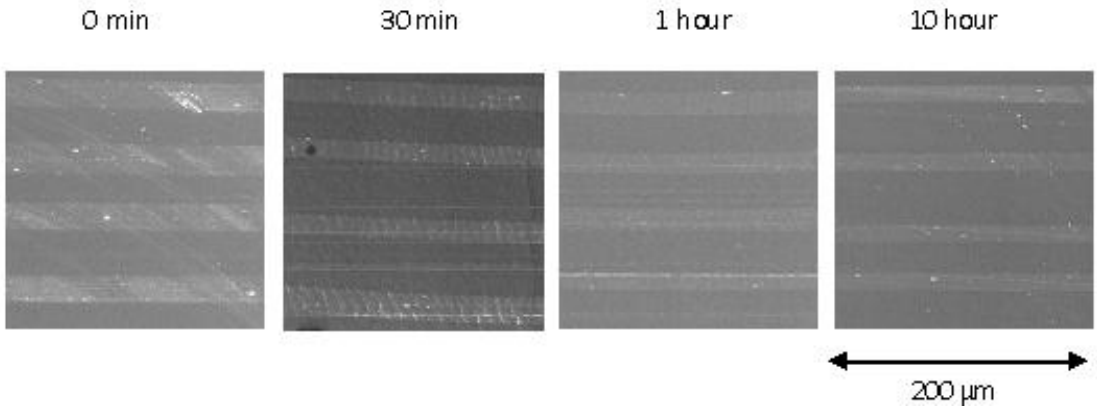

*Figure 26***.** SEM of the 17 layer 5% mica-LLDPE/LDPE multilayer annealed at 200 ℃ for the time indicated.

The SEM images in Figure 26 show the LLDPE-Mica/LDPE 17 layer materials after being annealed in the melt at 200 ℃ for various periods of time (0 min, 30 min 1 hours and 10 hours). Each image shows a 200 µm ×200 µm section with 7 individual layers. As mentioned previously the filled and unfilled layers had approximately the same thicknesses in the originial multilayer materials. After 30 min in the melt, the filled LLDPE layers became noticeably thinner and the LDPE layers became thicker due to the moving boundary effect. After 10 hours, the thickness differences are really significant between the LLDPE-mica layers and the LDPE layers.

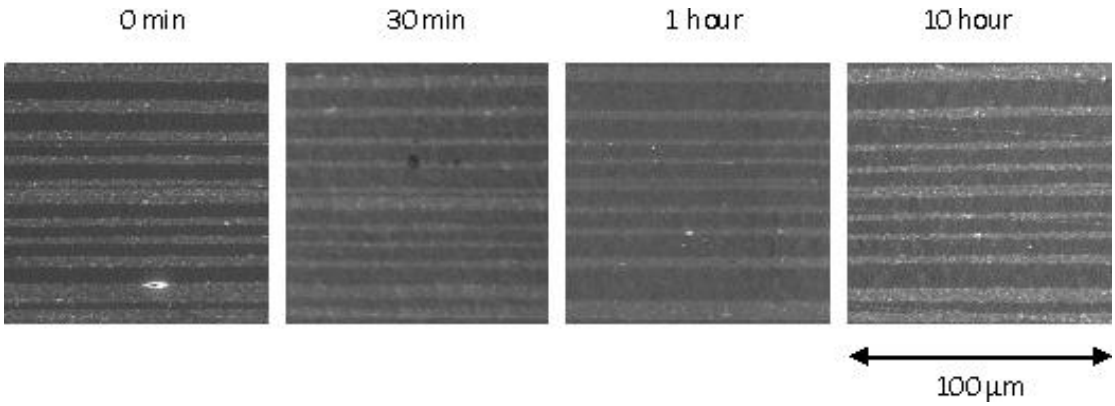

*Figure 27***.** SEM of the 65 layer 5% mica-LLDPE/LDPE multilayer annealed at 200 ℃ for the time indicated.

The thickness changes are plotted in Figure 28(a). The blue line shows the thickness of the LDPE layers and red line shows the thickness of the LLDPE-mica layers. The thicknesses are averages and the error bars reveal layer thickness variation. The gap between the two lines increased and reached a leveling off point within 60 minutes. After 60 minutes the diffusion speed became really slow and reached a plateau.

The SEM in Figure 27 shows the LLDPE-Mica/LDPE 65 layer material annealed at 200 ℃ for various times. Each image shows an 100 µm ×100 µm area. There are double layers in each picture which can be used as a marker to determine that the same layers were being analyzed in each image. The thickness changes of the double layers are obvious with an increase in annealing time (ie, 19.3 µm for 0 min, 17.9 µm for 30 min, 10.3 µm for 1 hour and 9.0 µm for 10 hours). However, the layers next to the double layer did not change as much (6.1 µm for 0 min, 5.0 µm for 30 min, 5.0 µm for 1 hour and 4.6 µm for 10 hours). Ideally, each filled and unfilled layers should perform the same way in the melt state, however, initial layer thickness differences, heterogeneity of the temperature in the films may result in a disparity in interdiffusion behavior for the different layers. The layer thickness as a function of annealing time is shown in Figure

28(b). Overall thicknesses of the LDPE layers increased and the LLDPE-mica layers decreased by increasing annealing time. 65 layers showed the same interdiffusion behavior and moving boundary effect as the 17 layer system with little difference in diffusion time. The error bar is larger because the thickness variation is greater for the 65 layer multilayer materials.

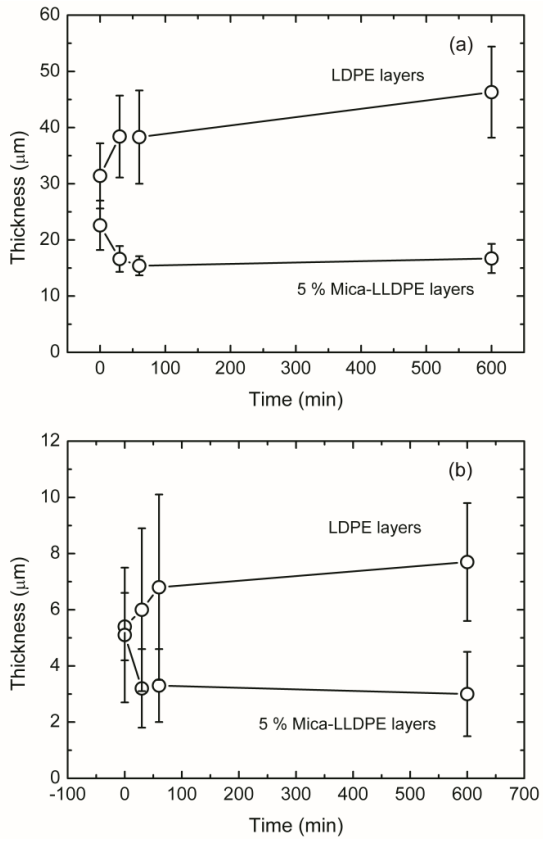

*Figure 28***.** Change in the average thicknesses of (a) 17 layers and (b) 65 layers of the 5% mica-LLDPE/LDPE layers with time in the melt at 200 ℃.

Gas Barrier Property

Density of synthetic mica is about 2.6 g/cm^3 before modification, the surface modifier alkyl ammonium surfactant is 0.859 g/cm^3 and the LLDPE is 0.926 g/cm^3. Based on these densities, the volume percent of mica can be calculated as shown in Table 3. All of the permeability measurements were repeated to assess the reproducibility of

the data. Pure maleic anhydride grafted LLDPE has a permeability of about 13.0 cc cm/m^2·day·atm at room temperature. The permeability of the pure LLDPE as reported previously, 35.3 cc cm/m^2·day·atm at 25 ℃ and 36.5 cc cm/m^2·day·atm at 35 ℃.[26,27] Maleic anhydride grafted LLDPE has a lower permeability than LLDPE because of the stronger chain interactions by adding a hydrophilic component. By adding different amounts of maleic anhydride, the permeability changes.

Gas barrier properties of the mica nanocomposites were investigated prior to the study of multilayer materials. High aspect ratio mica improved the gas barrier properties in the LLDPE-mica nanocomposites. This effect was described previously in Yano's work.[16] Impermeable mica creates a tortuous pathway for the gas molecules and thus causes a decrease in the diffusion coefficient. Gas permeability of the pure LLDPE and its nanocomposites are shown in the Figure 29(a). As the concentration of mica is increased, the permeability gradually decreases and reaches a plateau after 10% mica loading. The lowest permeability is 4.06 cc cm/m^2·day·atm (about 70% deduction in permeability compared to the pure polymer) with 10% mica in the LLDPE. Permeability did not decrease further due to poor dispersion of mica when the filler loading gets too high which can be observed from WAXD as shown previously.

As stated in equation 1, permeability is affected by both diffusivity and solubility. Diffusivity decreases through increasing the tortuousity of the gas molecules while solubility changes can bet attributed to changes in the amount of gas that can be absorbed into the film. The diffusion coefficient of the pure LLDPE and its nanocomposites are shown in Figure 29(b). The diffusion coefficient also decreased as mica concentration increased. The diffusion coefficient curve resembles the permeability curve which means the decrease in permeability is primarily a factor of the diffusivity decrease.

Table 3

Oxygen transport properties of mica filled LLDPE composites.

Materials	Absolute Weight percentage of mica (%)	Volume percentage of mica (%)	Permeability (cc cm/m^2/day/ atm)	Diffusivity ($10^{-7}$$cm^2$/s)	Solubility (cc/cc/atm)
LLDPE	0	0	13.12 ± 1.29	3.18	0.0511
3% mica LLDPE	1.68	0.60	8.57 ± 1.00	2.20	0.0488
5% mica LLDPE	2.80	1.01	6.06 ±0.03	1.40	0.0503
10% mica LLDPE	5.60	2.06	4.06 ± 0.71	1.16	0.0455
15% mica LLDPE	8.40	3.14	4.19 ±0.27	1.08	0.0469
LDPE	-	-	20.03	-	-

Solubility of the LLDPE and mica-LLDPE composites did not change significantly. It decreased slightly because the LLDPE content decreased when mica was added. However, the solubility did not exactly match the predicted line shown in Figure

29(c). The reason is some of the polymers may be trapped between mica bundles and bundle size increased as the mica content increased.

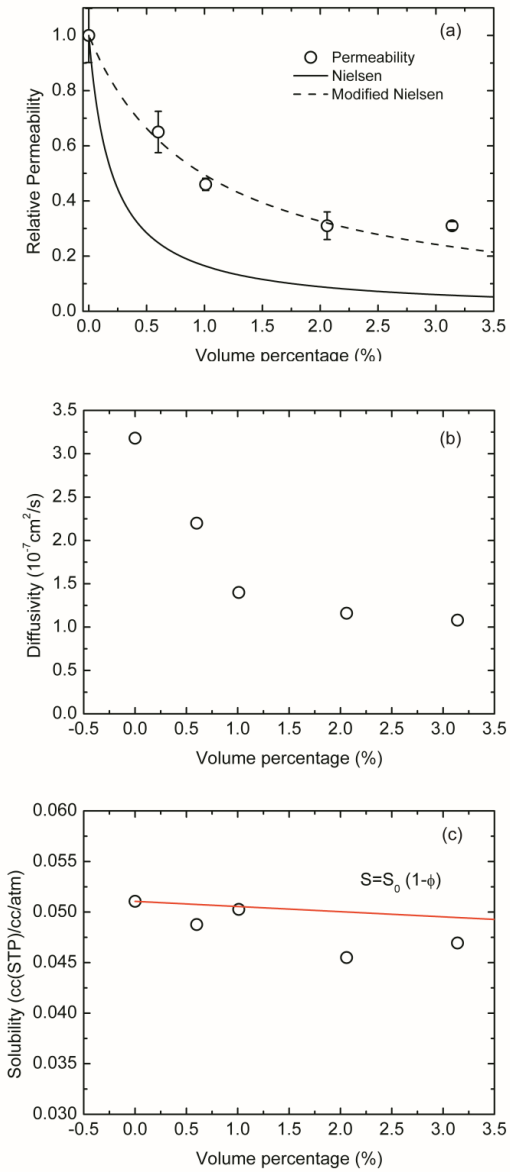

Figure 29. (a) Exerimental dependence of relative permeability and theoretical fit to Equation 4 and Equation 5 (α = 1000, N = 5), (b) Diffusivity and (c) solubility of Mica-LLDPE composites versus volume percentage of mica.

Relative permeability was plotted with theoretical prediction simulated by the Nielsen and modified Nielsen formula. Nielsen's formula[28] is used to predict the relative permeability of nanocomposites with disk-like shaped nanoparticles as compared to the

pure polymers. The formula can be used for the dilute regime in which disks are spaced at distances exceeding that of the disk radius and assumes the particles are orientated parallel to the film surface. In Nielsen's formua, P is the permeability of the nanocomposites, P_0 is the permeability of the pure polymer without the filler, ϕ is the volume percentage of the clay, and α is the aspect ratio of the clay.

$$\frac{P}{P_0} = \frac{1-\phi}{1+\frac{\alpha}{2}\phi} \tag{3}$$

Nazarenko et al.[20] proposed a modified Nielsen equation in the case of the existence of layer stacks in the polymeric systems instead of perfectly exfoliated fillers,

$$\frac{P}{P_0} = \frac{1-\phi}{1+\frac{\alpha}{2N}\phi} \tag{4}$$

where N is the number of silicate layers in the layer stacks.

The theoretical predictions of Nielsen and the modified Nielsen models were plotted with experimental data in Figure 29(a). Aspect ratio of the mica, $\alpha = d/h$, was about 1000, where d is diameter of mica and h is thickness of mica. The diameter of the mica was stated previously (Figure 13). Nielsen's model overestimates the reduction in permeability as it predicts a lower permeability than experimentally measured. This is caused by the reality that the mica layers were not perfectly exfoliated but formed small mica stacks. In contrast, the modified Nielsen model with $N = 5$, showed an excellent agreement with the experiment data. This is because the mica aggregated into small mica stacks with approximately 5 mica layers in each stack. TEM micrographs were also used to observe the size of the layer stacks and supported the results from the modified Nielsen model fitting mentioned previously in Figure 17.

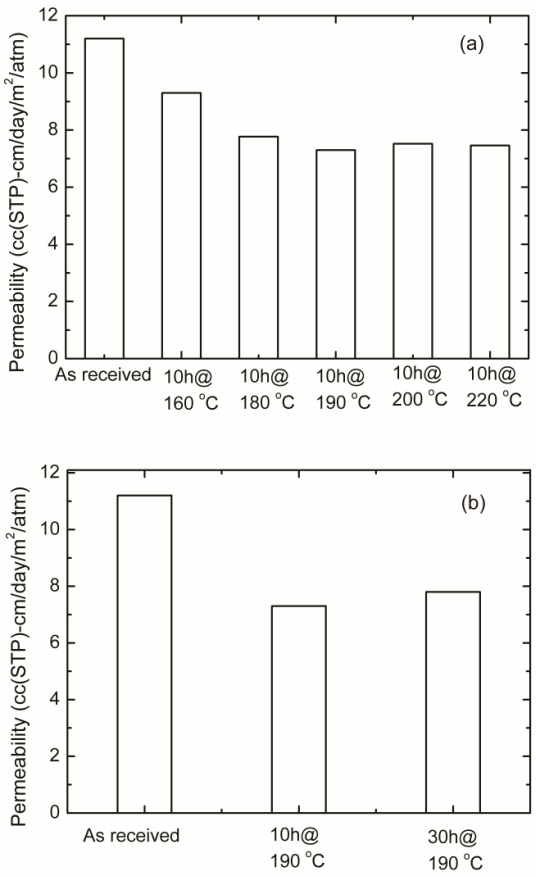

Figure 30. Permeability of 65 layers multilayer materials (a) annealed at different temperatures for 10 hours and (b) for times indicated at 200 ℃.

The permeability of the multilayer materials consisting of LLDPE and 5% mica-LLDPE can be calculated by a series model of the form:[4]

$$\frac{1}{P_m} = \frac{1}{2P_0} + \frac{1}{2P_f} \tag{5}$$

where P_0 is the permeability of the LDPE and P_f is permeability of the 5% mica nanocomposite and P_m is the permeability of the 5% mica-LLDPE /LDPE multilayer materials. As shown in Table 3, the permeability of the LDPE and 5% mica-LLDPE nanocomposites are 20.03 cc cm/m^2·day·atm and 6.06 cc cm/m^2·day·atm, respectively. Multilayer material permeability, P_m, should be 9.3 cc cm/m^2·day·atm based on Equation 5 which is lower than the experimental results of 11.6 cc cm/m^2·day·atm for the 17 layer

multilayer materials and 11.1 cc cm/m^2·day·atm for the 65 layer multilayer materials. Particle orientation and dispersion may change slightly during the multilayering process which can cause an increase in permeability as compared to the theoretically predicted value.

Multilayer material were annealed for different times and temperatures and analyzed for gas barrier properties. This experiment was conducted to optimize the temperature and time needed to achieve the best barrier property improvement. The 65 layer materials were annealed in the melt at temperatures of 160 ℃, 180 ℃, 190 ℃, 200 ℃ and 220 ℃ for 10 hours. It is well known that polymer chain movement is highly depend on the temperature and as temperature increases the diffusion speed increases. Figure 30(a) shows that the gas permeability decreases when the annealing temperature was increased and leveled off after 190 ℃. The optimal temperature is 190-200 ℃ for annealing these multilayer films. Lower temperature restricts the chain movement and higher temperature may result in oxidation and degradation of the polymers.

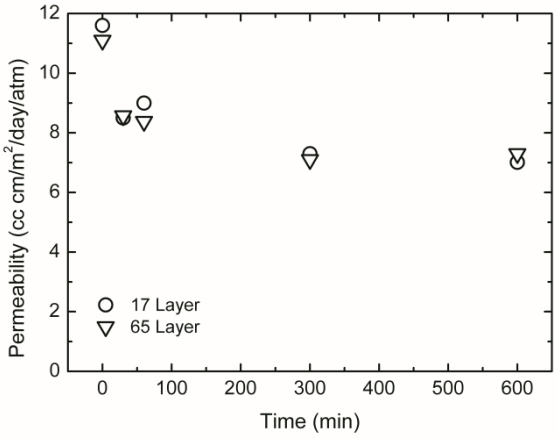

Figure 31. Permeability of 17 layers and 65 layers 5% mica-LLDPE/LDPE multilayer materials before and after annealing at 200 ℃ for time indicated.

Time of annealing is also very important. This effect can be explained when the gas barrier measurements are combined with the SEM results. LLDPE-mica layer did not

shrink much further when comparing the 1 hour and 10 hour anneal times as observed from the SEM pictures showed previously. The interdiffusion effect was possibly restricted by the concentrated high aspect mica at the layer interfaces when the mica concentration reached about 7-8%. Even increasing the annealing time to 30 hour, as shown in Figure 30(b), did not changed the permeability as compared to annealing for 10 hours. The highest level of interdiffusion in this study was achieved by 10 hours of anneal time.

The permeability of the annealed multilayer materials as a function of time in the melt is plotted in Figure 31. The 17 and 65 layer films were annealed at 200 ℃ for 30 min, 60 min, 5 hours and 10 hours. Permeability decreased rapidly when annealed for 30 min, after that permeability did not change much up to 10 hours. This result corresponds to the SEM analysis of layer thicknesses of the multilayer materials annealed for various times. Permeability of the multilayer materials decreased from 11.6 cc cm/m^2·day·atm to 7.0 cc cm/m^2·day·atm for 17 layers and 11.1 cc cm/m^2·day·atm to 7.3 cc cm/m^2·day·atm for 65 layers. The gas barrier propertieswere improved by 40% for the 17 layer films and 35% for the 65 layer films.

The permeability of the mica filled layers, P_f, was extracted from the measured permeability using Equation 5. P_0 is the permeability of the LDPE layers (20.03 cc cm/m^2·day·atm) and P_m is the permeability of the 10 hour annealed films (7.01 cc cm/m^2·day·atm). The calculated P_f of the 10 hour annealed 65 layer film is 4.5 cc cm/m^2·day·atm which is close to permeability of the 10% mica nanocomposites (4.06 cc cm/m^2·day·atm). The extracted P_f values for the films annealed for different times are listed in Table 4. The filled layer permeability decreased from 8.1 cc cm/m^2·day·atm to

4.3 cc cm/m^2·day·atm which is a 47% improvement of gas barrier properties compare before and after annealed mutlialyer materials. When compare to the 5% mica-LLDPE nanocomposites, permeability (6.06 cc cm/m^2·day·atm) decreased by 30% for the filled layers.

Table 4

Oxygen permeability of 5% mica-LLDPE/LDPE multilayer materials and filled layers extracted from multilayer materials.

	17 layers multilayer materials		65 layers multilayer materiasl	
Annealing time	P_m	P_f	P_m	P_f
0 min	11.6	8.1	11.1	7.6
30 min	8.5	5.4	8.5	5.4
1 hour	9.0	5.8	8.4	5.3
5 hours	7.3	4,5	7.1	4.3
10 hours	7.0	4.3	7.3	4.5

Conclusions

Surfactant modified mica was able to be exfoliated in the LLDPE polymer matrix at low concentrations of mica. Nanocomposites and LDPE were multilayered in alternating layers of 17 and 65 layers using a multilayer co-extruder with layer thicknesses of about 30 and 5μm. A moving boundary was observed between LLDPE-Mica layers and LDPE layers after annealing these multilayer materials at 200 ℃ for different annealing hours. Mica filled LLDPE layers were shrunk while LDPE layers were swelled by increasing annealing time, however, the interdiffusion became slow after

60 min. Filled layers decreased by 30% for the 17 layerand 40% for the 65 layer film after 10 hours of annealing, reaching the limit of boundary movement. Gas barrier properties of annealed samples improved compared to as received multilayer materials because mica was concentrated in the LLDPE layers. Gas barrier properties of the annealed films improved by 40% and the filled layer gas barrier properties improved by 47% as compared to the as received multilayer films. The gas barrier properties did not improve further because boundary movement ceased after a certain time.

REFERENCES

1. Mueller, C. D.; Nazarenko, S.; Ebeling, T.; Schuman, T. L.; Hiltner, A.; Baer, E. Novel Structures by Microlayer Coextrusion-Talc-Filled PP, PC/SAN, and HDPE/LLDPE. *Polym. Eng. Sci.* **1997,** *37*, 355–362.
2. Ma, M.; Vijayan, K.; Hiltner, A.; Baer, E.; Im, J. Thickness Effects in Microlayer Composites of Polycarbonate and Poly(Styrene-Acrylonitrile). *J. Mater.Sci.* **1990**, *25*, 2039–2046.
3. Sung, K.; Hiltner, A.; Baer, E. Three-dimensional Interaction of Crazes and Micro-shearbands in PC-SAN Microlayer Composites. *J. Mater.Sci.* **1994**, *29*, 5559–5568.
4. Sekelik, D. I.; Stepanov, E. V.; Nazarenko, S.; Schiraldi, D.; Hiltner, A.; Baer, E. Oxygen Barrier Properties of Crystallized and Talc-Filled Poly(ethylene terephthalate). *J. Polym. Sci., Part B: Polym. Phys.* **1999**, *37*, 847–857.
5. Jarus, D.; Hiltner, A.; Baer, E.; Microlayer Coextrusion as A Route to Innovative Blend Structures. *Polym. Eng. Sci.* **2001**, *41*, 2162–2171.
6. Jarus, D.; Hiltner, A.; Baer, E. Barrier Properties of Polypropylene/Polyamide Blends Produced by Microlayer Coextrusion. *Polymer* **2002**, *43*, 2401–2408.
7. Nazarenko, S.; Dennison, M.; Schuman, T.; Stepanov, E. V.; Hiltner, A.; Baer, E. Creating Layers of Concentrated Inorganic Particles by Interdiffusion of Polyethylenes in Microlayers. *J. Appl. Polym. Sci.* **1999**, *73*, 2877–2885.
8. Mueller, C.; Kerns, J.; Ebeling, T.; Nazarenko, S.; Hiltner, A.; Baer, E. Microlayer Coextrusion: Processing and Applications. *Polymer Process Engineering*. Coates, P. D., Eds.; Vol. 97. London: Bradford, **1997**, 137–157.
9. Keskkula, H.; Paul, D. R.; Young, P.; Stein, R. S. Diffusion of Miscible Polymers in

Multilayer Films. *J. Appl. Polym. Sci.* **1987**, *34*, 1861–1877.

10. Schuman, T.; Nazarenko, S.; Stepanov, E.V.; Magonov, S.N.; Hiltner, A.; Baer, E. Solid State Structure and Melting Behavior of Interdiffused Polyethylenes in Microlayers. *Polymer* **1999**, *40*, 7373–7385.
11. Schuman, T.; Stepanov, E.V.; Nazarenko, S.; Capaccio, G.; Hiltner, A.; Baer, E. Interdiffusion of Linear and Branched Polyethylene in Microlayers Studied via Melting Behavior. *Macromolecules* **1998**, *31*, 4551–4561.
12. Nazarenko, S.; Dennison, M.; Schuman, T.; Stepanov, E. V.; Hiltner, A.; Baer, E. Creating Layers of Concentrated Inorganic Particles by Interdiffusion of Polyethylenes in Microlayers. *J. Appl. Polym. Sci.* **1999**, *73*, 2877–2885.
13. Alexandre, M. and Dubois, P. Polymer-Layered Silicate Nanocomposites: Preparation, Properties and Uses of A New Class of Materials. *Mater. Sci. Eng., R: Reports* **2000**, *28*, 1–63.
14. Ray, S. S., and Okamoto, M. Polymer/layered Silicate Nanocomposites: A Review from Preparation to Processing. *Prog. Polym. Sci.* **2003**, *28*, 1539–1641.
15. Zanetti, M.; Lomakina, S.; Camino, G. Polymer layered silicate nanocomposites. *Macromol. Mater. Eng*. **2000**, *279*, 1–9.
16. Yano, K.; Usuki, A.; Okada, A. Synthesis and Properties of Polyimide-Clay Hybrid Films. *J. Polym. Sci. Part A: Polym. Chem.* **1997**, *35*, 2289–2294.
17. Lan, T.; Kaviratna, P. D.; Pinnavaia, T. J. On the Nature of Polyimide-Clay Hybrid Composites. *Chem. Mater.* **1994**, *6*, 573–575.
18. Messersmith, P. B.; Giannelis, E. P. Synthesis and Barrier Properties of Poly(ε-Caprolactone)-Layered Silicate Nanocomposites. *J. Polym. Sci. Part A: Polym.*

Chem. **1995**, *33*, 1047–1057.

19. Hotta, S.; Paul, D.R. Nanocomposites Formed from Linear Low Density Polyethylene and Organoclays. *Polymer* **2004**, *45*, 7639–7654.
20. Nazarenko, S.; Meneghetti, P.; Julmon, P.; Olson, B.G.; Qutubuddin, S. Gas Barrier of Polystyrene Montmorillonite Clay Nanocomposites: Effect of Mineral Layer Aggregation. *J. Polym. Sci. Part B: Polym. Phys.* **2007**, *45*, 1733–1753.
21. Soon, K.; Harkin-Jones, E.; Rajeev, R. S. Morphology, Barrier, and Mechanicalproperties of Biaxially Deformed Poly(Ethylene Terephthalate)-Mica Nanocomposites. *Polym. Eng. Sci.* **2012**, *52*, 532–548.
22. Xanthos, M; Faridi, N; Li, Y. Processing/Structure Relationships of Mica-Filled PE-Films with Low Oxygen Permeability. *Int. Polym. Proc.* **1998**, *13*, 58–66.
23. Pinnavaia, T. J. Intercalated Clay Catalysts. *Science* **1983**, *220*, 365–371.
24. LeBaron, P.C.; Wang, Z.; Pinnavaia, T. J. Polymer-Layered Silicate Nanocomposites: An Overview. *Appl. Clay Sci.* **1999**, *15*, 11–29.
25. Fukushima, Y.; Inagaki, S. Synthesis of An Intercalated Compound of Montmorillonite and 6-Polyamide. *J. Inclusion Phenom.* **1987**, *5*, 473–482.
26. Durmus, A.; Woo, M.; Kasgoez, A.; Macosko, C. W.; Tsapatsis, M. Intercalated Linear Low Density Polyethylene (LLDPE)/Clay Nanocomposites Prepared with Oxidized Polyethylene as A New Type Compatibilizer: Structural, Mechanical And Barrier Properties. *Eur. Polym. J.* **2007**, *43*, 3737–3749.
27. Hotta, S.; Paul, D. R. Nanocomposites Formed from Linear Low Density Polyethylene and Organoclays. *Polymer* **2004**, *45*, 7639–7654.
28. Nielsen, L. E. Models for the Permeability of Filled Polymer Systems. *J. Macromol.*

Sci., Part A **1967**, *1*, 929–942.

CHAPTER V

MICA FILLED MULTILAYERED COMPOSITES WITH ENHANCED FLAME RETARDANT PROPERTIES

Abstract

Polymer-layered silicate nanocomposites form a class of flame retardant materials of interest due to their balance of mechanical, thermal, gas barrier and flammability properties. Multilayer coextrusion is an attractive approach to creating alternating layers of two polymers and polymer composites for mechanical and gas barrier property improvement. These two approaches combined together allowed the fabrication particulate-filled nanocomposite polymer film structures with enhanced flame retardant properties. Organophylic mica with an aspect ratio of 1000 was used as the high aspect ratio nanocomposite filler in this research. Multilayered composites were processed with alternating layers of pure low-density polyethylene (LDPE) and mica filled linear low-density polyethylene (LLDPE) containing grafted maleic anhydride to promote particulate dispersion. Moving boundary effect is demonstrated in systems including LLDPE/LDPE multilayer systems as LLDPE, with its numerous short branches, was more mobile than the long branched LDPE polymer. SEM and TEM analysis were employed to probe the films' layer morphology and the platelet orientation/dispersion in the nanocomposite blends and nanoparticulate filled multilayer systems. Flame retardant properties of the blends and multilayer composites were measured and related to the morphological observations. It was shown that multilayer materials have decreased peak heat release rate and enhanced char formation as compared to nanocomposite blends with the same mineral compositions.

Introduction

A wide variety of fillers such as phosphorus, halogens and so on can be very effective for different polymer systems.[1-5] However, these traditional fillers may severely affect the other important properties, such as mechanical, thermal and rheological properties.

Layered-silicate containing nanocomposites have potential to improve flame retardant properties for different polymers without sacrificing other properties. Montmorillonite (MMT) is mostly used layered-silicate nanoparticles for flame retardant properties. Recently, Gilman and his coworkers reported that improved flammability behaviors were observed for a bunch of polymer-MMT nanocomposites measured by cone calorimetry.[6,7] Peak heat release rate (PHRR) of nylon 6 decreased to 361 kW/m^2 from 1011 kW/m^2 by adding 5% MMT to the polymeric systems. Polyethylene-MMT systems studied for flame retardant properties by Zhang and Wilkie.[8] The presence of 3% modified MMT in the LDPE brings about a reduction of 30-40% in the peak heat release rate. The amount of the PHRR reduction is quite variable for MMT containing polymers, depending on the modification of MMT and polymer systems, ranged from 25% to 60% with same amount of MMT. Flame retardant property improved when the nanoparticles exfoliated or intercalated in the polymers. Flame retardant properties decreased compare to the pure polymers with nanoparticls poorly dispersed systems because MMT layers form stacks and elevated temperature causes bigger flame.

Different polymeric systems, polypropylene (PP) and polystyrene (PS), filled with MMT and fluorohectorite were also studied for flame retardant properties.[7] Cone calorimetry measurement showed that all MMT-based nanocomposite systems reported

had reduced flammability and fluorohectorite nanocomposite was ineffective at reducing the flammability of PS due to poor dispersion of large aspect ratio fluorohectorite. Large aspect ratio nanoparticles were expected to have better flame resistant properties if the dispersion was improved. Layered-silicate nanocomposites reduce the flammability by creating barrier layers on the top of the burning material to limit the decomposed small molecules movement.

Synthetic mica is one type of layered silicate with high crystalline, high aspect ratio, and stable physical and chemical properties. Mica has different chemical structure formula compare to MMT and is more difficult to exfoliate due to the high aspect ratio feature. However, polymer-mica composites had better mechanical[9,10] and barrier[11,12] than polymer-MMT composites when mica were well dispersed in the polymer matrices. In the previous paper, flammability performance of MMT and mica nanocomposites behaved similarly within the cone calorimeter, with the mica nanocomposites showing lower PHRR values.[13] It was shown that increasing the total loading of organoclay is a possibility to improve flammability, but as clay loading is increased, the nanocomposite benefits are lost.

Multilayered co-extrusion and moving boundary effect allowed generate concentrated particles in the polymeric systems with small amount of particles. Co-extrusion is a technique by which two or more different polymers are combined into micro or nanolayer materials with up to thousands of layers.[14] This technique can be utilized and combined with other processing techniques to improve a film's mechanical,[15,16] gas barrier[17-19] and electrical properties.[20]

The co-extrusion system used to prepare micro and nanolayered materials consist of two extruders, a series of layer multiplier elements and a film die.[21] The two extruders produce an initial bilayer flow that then travels through a series of multiplying die elements. In each element the melt is first sliced vertically, then spread horizontally, and finally recombined by stacking, doubling the number of layers with each multiplication. The total number of layers can range from tens to thousands with individual layer thicknesses from the macro to the nanoscale.

Differences in the fractional diffusion coefficients of the components will result in convective flow and movement of the initial interface, known as the "moving boundary effect".[22, 23] Interdiffusion behaviors can be observed between contacting miscible polymers in the melt state. In a multilayer system, with a high interface to volume ratio, the interdiffusion progression is easy to observe by annealing the materials into the melt state. Multilayer concentration profiles across the layers gradually convert into a periodic gradient blend with compositional maxima located at the centers of the initial layers.[24]Interdiffusion kinetics depends on the diffusion coefficient of the contacting polymers in the layers which is directly related to the structure, composition, temperature, molecular weight, and polydispersity of the polymers. Convective flow is evident by the movement of the interface towards the faster diffusing component. The moving boundary effect in microlayers was demonstrated with a miscible high density polyethylene (HDPE), low density polyethylene (LDPE) and linear low-density polyethylene (LLDPE) system.[23] The moving boundary effect was caused by relative immobility of a high molecular weight fraction of the HDPE for HDPE/LLDPE pairs and long chain branched LDPE molecules for LDPE/LLDPE pairs.

The moving boundary effect in layers can be exploited to create layered structures with highly concentrated inorganic particles. This can be achieved by filling the fast diffusing polymer layers with inorganic particles. Inorganic particle (TiO_2, nickel, and talc platelets) filled LLDPE and unfilled low-density polyethylene (LDPE) multilayer systems were studied previously.[25] When the polymer layers were interdiffused at 200 ℃ for 600 min, the inorganic particle filled layers were distinctly thinner than the initial layers, decreasing from 30 μm to about 10 μm. This lead to inorganic particle concentration in the LLDPE layers as the inorganic particles did not interdiffuse into the other polymer phase. Particle size is much bigger than the polymer chain and movement of the inorganic particles is slower.

In this study, nanocomposites and multilayer technique were combined together to generate high aspect ratio mica filled multilayer materials. This is the first time co-extruded multilayer materials with nanoparticle filler were used for flame retardant test. The filler loading was 5% (wt/wt) in LLDPE layers in order to maintain the dispersion of mica. Mica was modified using surface modifier and exfoliated in the LLDPE matrix. Multilayer materials were processed using LDPE and mica-LLDPE materials with total layer numbers 17 and 65 layers which had thickness of individual layers 20 μm and 5 μm. Dispersion of mica in nanocomposites and multilayer materials were observed by TEM and multilayer structures were observed using SEM. Flammability and thermal stability of nanocomposites and multilayer materials were tested using cone calorimetry and TGA analysis. Effect of the nanoparitcles, multilayer technique and moving boundary phenomena on the flammability was investigated.

Experimental

Materials

Linear low density polyethylene (LLDPE) was provided by Chemtura Corporation under the trade name Polybond® 3149. The LLDPE was modified with 1% maleic anhydride and had a melt flow index of 12-30 g/10min (ASTM D 1238). Low density polyethylene (LDPE) was provided by Dow Plastic under the trade name Dow™ LDPE 640I with a melt flow index of 2 g/10min (ASTM D 1238). The density of the LLDPE and LDPE is 0.926 g/cc and 0.9215 g/cc respectively.

Synthetic mica (Somasif ME-100) with an aspect ratio of 1000 is a synthetic fluorohectorite produced by CO-OP Chemical Co., Japan. Its structural formula can be expressed as $Na_{2x}Mg_{3.0-x}Si_4O_{10}(F_yOH_{1-y})_2$, (x = 0.15-0.5,y = 0.8-1.0). The mica has a cation-exchange capacity (CEC) of 120 meg/100g. The surface modifier used in this study, Di(hydrogenated tallow) dimethylammonium chloride, a standard alkyl ammonium surfactant (ARQUAD 2HT-75), was provided by Sigma-Aldrich Corporation.

Mica Modification

Mica was modified via a cation exchange reaction. 1% (wt/wt) unmodified mica was dispersed in deionized water, and then the surface modifier (ARQUAD 2HT-75) was added in accordance with the CEC of the mica. After the cation exchange reaction was completed, the modified clay was filtered and dried. The original cation in the galleries was replaced by the organic cation after the reaction. The cation head was attached to the surface of the mica because the surface of the Mica is negatively charged. The organic tail was in between the two mica layers to further separate the layers. Wide Angle X-Ray Diffraction (WAXD) (Rigaku Ultima III) and TGA (TA Q500) were used to determine the

d-spacing of the modified mica and organic modification reported in the previously.[26] The basal spacing of mica is about 1 nm before surfactant modification and 3.4 nm after modification. Based on the TGA analysis about 45% of organic modifier reacted with inorganic mica.

Nanocomposites Preparation

Modified mica was blended with LLDPE using PRISM TSE 16TC twin-screw extruder at 200 ℃ and 50 rev/min screw speed. Twin screw extruders are commonly used for polymer processing because the high shear force can separate the platelet layers. The pelletized LLDPE was mixed uniformly at dry conditions with mica powder before melt blending in the extruder. The mixture of LLDPE and mica was added to the feeder of the extruder and the polymer was mixed with the nanoparticles in the molten state during the extruder process. The composites from extruder were pelletized and dried in the oven at 90 ℃ for 2 hours. LLDPE-mica nanocomposites with 0-15% (wt/wt) mica composition were prepared. All of the composites were passed through the extruder 3 times to achieve optimal dispersion of mica in the polymer.

Transmission Electron Microscopy (TEM) (JEOL Ltd. JEM-2100) was performed at 200 kV on the nanocomposites to analyze dispersion of the mica in the nanocomposites. The specimens were cryo-microtomed in thin sections of 70-100 nm and placed on a copper grid with no staining agents.

Multilayer Materials Preparation

Multilayers with alternating layers of LDPE and LLDPE/mica were extruded using a continuous layer-multiplying co-extruder at Case Western Reserve University. By varying the melt feed ratio, the film thickness, number of layers, and the individual layer

thicknesses can be precisely controlled. The extrusion rates were regulated to obtain a 1:1 ratio of the components. The films in this study had a thickness of approximately 400 μm, 17 and 65 layers, and individual layer thicknesses of 20 and 5 μm respectively. The extruding temperature was 200 ℃. LDPE and LLDPE/mica viscosities matched at this temperature.

The multilayer materials were annealed in the oven while confined with a metal mold in a nitrogen atmosphere. Nitrogen was used to prevent the degradation of the polymers. The annealing temperature of the multilayer films was 200 ℃ and annealing times were 30 min, 60 min, 5 hours and 10 hours. The films were covered by Teflon sheets on the top and bottom to preserve the films' smooth and uniform surface. The films were quenched in a water bath after annealing.

TEM was also used to analyze the dispersion and orientation of the mica in the multilayered systems before and after annealing. Scanning Electron Microscopy (SEM) was performed using a FEI Quanta 200 SEM. SEM was utilized to analyze layer thicknesses in the multilayer materials before and after annealing. The cross sections of these materials were cryo-microtomed and sputter coated using gold particles prior to the SEM test.

Flame retardant test

Cone Calorimeter (Gavmark Cone) was used to evaluate the fire properties of the LLDPE-mica composites and multilayered LLDPE-mica/LDPE composites. Cone calorimeter measurements were performed according to ASTM E 1354 at 50 kW/m^2 incident fluxes using a cone shaped heater with the exhaust flow set at 24 L/sec. The samples square plaques of approximately 30 g, $3 \times 100 \times 100$ mm^3 for cone calorimetry

were prepared by compression molding. Typical results from cone calorimetry were reproducible to within about ±10%.[27] These uncertainties are based on many runs in which thousands of samples have been combusted.

Results and Discussion

High aspect ratio mica are plate-like shaped nanoparticles with 1 nm thickness (*h*) and about 1000 nm diameter (*d*). Mica was modified by hydrophobic surface modifier to improve wetting of hydrophobic polymers. The LLDPE contained 1% maleic anhydride by weight which can work as a compatibilizer between hydrophobic polymers and hydrophilic nanoparticles to help the dispersion of the particles in the polymer matrix. Nanocomposites properties, such as mechanical, thermal, rheological and gas barrier properties were highly affected by the dispersion and orientation of the nanoparticles in the polymer systems.

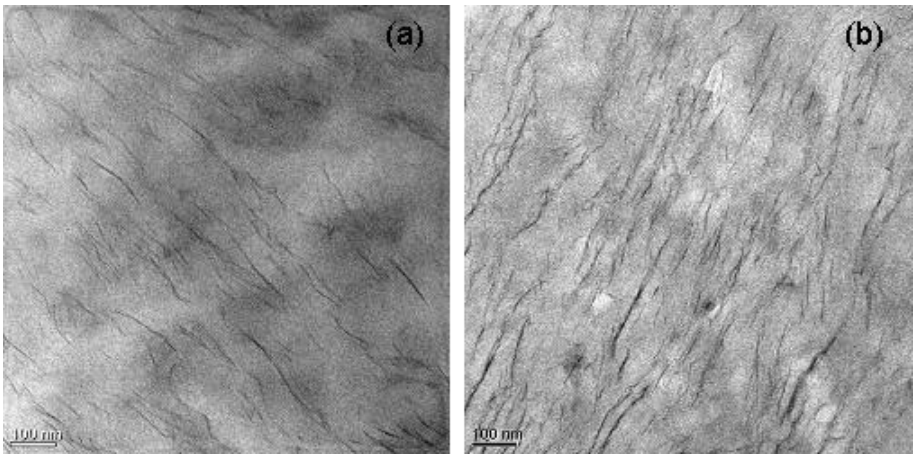

*Figure 32***.** TEM of (a) 5% (wt/wt) and 10% (wt/wt) LLDPE-mica nanocomposites.

WAXD was used to analyze the mica dispersion in the LLDPE which was reported in the previous paper.[26] There were not any reflection peaks for low loading nanocomposites and intercalation peaks were observed for the high loading nanocomposites. WAXD shows the average dispersion of the mica in the LLDPE,

however, it is difficult to be conclusive on the orientation, distribution, and shape of the mica particles. Furthermore, it is difficult to determine the existent of large aggregates from WAXD analysis. TEM can be used to better describe the dispersion of the mica in the polymer matrix to be combined with the WAXD data. TEM provides a direct visual depiction of the composites' structure. Figure 32(a) shows the LLDPE-mica composites with 5% (wt/wt) modified mica. The composites were cryo-microtomed to 100 nm thick sections before testing. From the TEM images of Figure 32(a) it appears that the mica is well dispersed in the polymer matrix and both single layer mica and small stacked mica layers were observed. Mica particles are oriented in the direction parallel to the film surface. Compression molding of nanocomposites contributes to the orientation of the particles in the polymeric systems in melting state. The results of TEM and WAXD showed that composites with 5% (wt/wt) mica were a combination of primarily exfoliated platelets and some intercalated stacks.

Figure 32(b) shows TEM image of the 10% mica-LLDPE composites, representing a high mineral content system. Individual layers were hardly visible on the image and a large amount of aggregates were observed through the whole film. Aggregates contained several mica layers in which the mica layers were tilted and bent. The interlayer spacing was fairly heterogeneous. Mica aggregates showed orientation in the direction parallel to the film surface. TEM shows mixture of intercalated and coherent layer stacking structures. Mica is better dispersed and exfoliated in 5% mica composites than in 10% mica composites. So, 5% mica-LLDPE systems and LDPE were chosen to make multilayer materials with the proper extruding temperature.

Multilayer materials were fabricated using a co-extruder that contains alternating layers of LDPE and 5% (wt/wt) mica LLDPE nanocomposites. Multilayer materials were designed to have a total number of layers of 17 and 65 layers. Multilayer materials had a total thickness of about 300-400 μm and a width of 15 cm. The top and bottom layers are both LDPE layers with half the thickness of the inner layers. The 17 layer and 65 layer multilayer materials had single layer thicknesses of 20 μm and 5 μm, respectively.

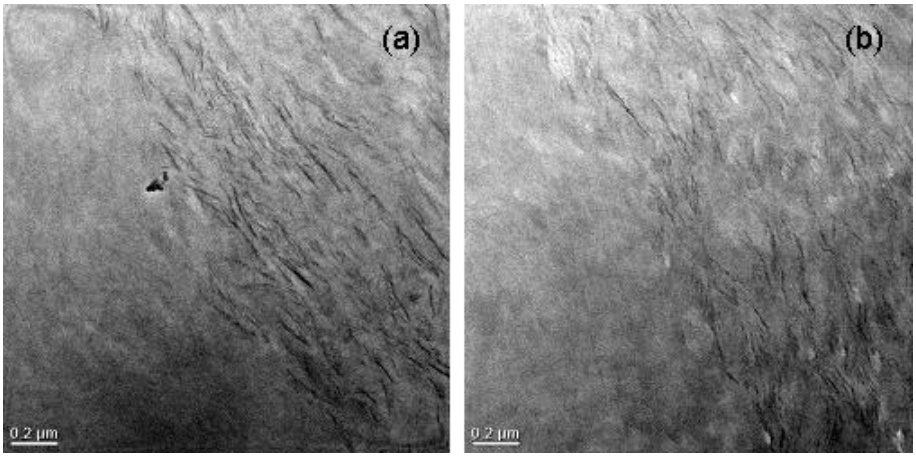

*Figure 33***.** TEM of Multilayer material (a) 17 layers and (b) 65 layers of 5% Mica-LLDPE/LDPE showing both LDPE and Mica-LLDPE layers.

TEM was used to confirm the structure of the mica in the multilayer materials as showed in Figure 33. Figure 33(a) shows the cross section of the 17 layer multilayer materials containing both LDPE and LLDPE-mica layers with clear boundary. The mica appears well dispersed and only a small amount of intercalated structures were observed near the boundary of LLDPE-mica and LDPE layers. Orientation of the mica parallel to the film surface can be attributed to the fact that the high aspect ratio mica can be rotated and aligned by the moderate shear forces that arise as the melt spreads out in the press. In both compression molded composites and multilayered material, an ordered structure of mica particles can be observed.

Figure 33(b) shows the 65 layer multilayer materials with both the LDPE and LLDPE-mica layers in the TEM images. Orientation of the mica can be observed for the 65 layers system, with mica still well dispersed in the LLDPE layers. The 65 layer multilayer materials have an individual layer thickness of about 5 μm. The average mica diameter (1μm) is in the same range as that of the individual layer thicknesses of the 65 layers multilayer materials. Particles tend to lose their orientation and reaggregate when the layer thickness is close to the particle size. However, reaggregation or a change in orientation of the mica was not evident after the multilayering process. The dispersion of mica in the 17 layer and 65 layer systems appear very similar.

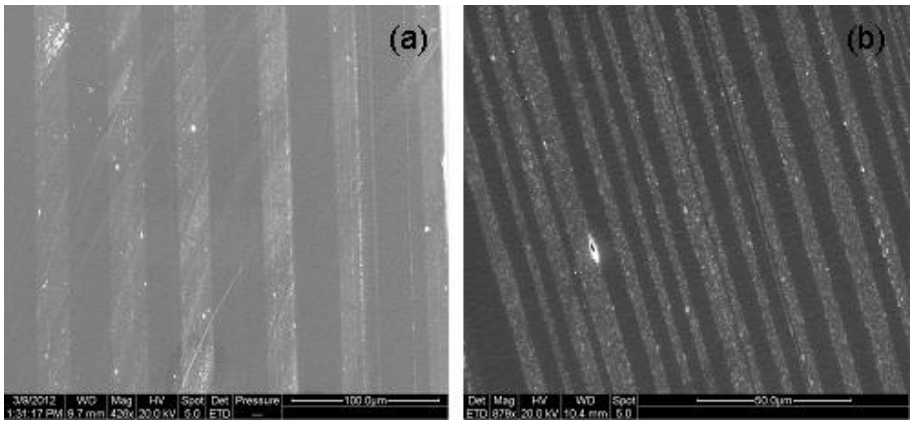

Figure 34. SEM of the (a) 17 layers and (b) 65 layers 5% Mica-LLDPE/LDPE multilayer materials.

Layer structures were observed using SEM by looking at the cross section of the multilayer films. Figure 34 shows SEM images of the 17 layer and 65 layer multilayer materials. The layers are well structured with clear and straight boundaries of the two polymers. For the 17 layer materials, the white layers are the mica filled LLDPE layers with an average thickness of 22.6 μm while the black layers are the LDPE layers with an average thickness of 31.4 μm. LDPE and LLDPE-mica were fed at an 1:1 ratio during the multilayer process, however, the thickness of LLDPE-mica layers and LDPE layers are

slightly different. This may be caused by the interdiffusion of the LLDPE and LDPE layers and the moving boundary effect during the multilayering process. Figure 34(b) shows an SEM image of the 65 layer multilayer material. Both LLDPE-mica and LDPE layers have large variation in thickness. The average thicknesses of the LLDPE-mica and LDPE layers are 5.1 and 5.4 μm, respectively.

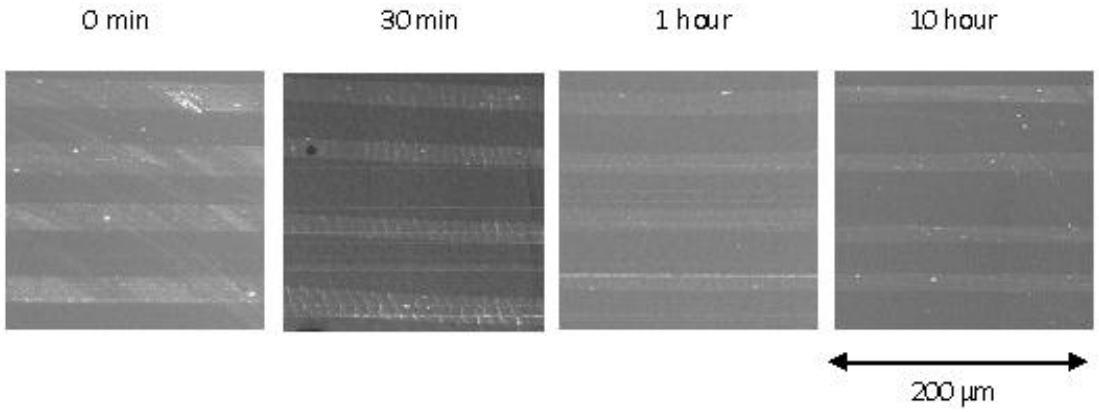

*Figure 35***.** SEM of the 17 layer multilayer annealed for 0 min, 30 min, 1 hour and 10 hours.[26]

Figure 35 show the LLDPE-Mica/LDPE 17 layer materials after being annealed in the melt at 200 ℃ for various periods of time (0 min, 30 min 1 hours and 10 hours). Each image shows a 200 μm×200 μm section with 7 individual layers.[26] As mentioned previously the filled and unfilled layers had approximately the same thicknesses in the original multilayer materials. After 30 min in the melt, the filled LLDPE layers became noticeably thinner and the LDPE layers became thicker due to the moving boundary effect. After 10 hours, the thickness differences are really significant between the LLDPE-mica layers and the LDPE layers. LLDPE is a short chain branched linear polymer and LDPE is a long chain branched polymer contributing to their different mobilities and diffusion coefficient in the melt. Differences in the fractional diffusion coefficients of the components result in a convective flow and movement of the initial

interface toward the faster diffusing material. The thickness changes reached a leveling off point within 60 minutes. After 60 minutes the diffusion speed became really slow and reached a plateau.

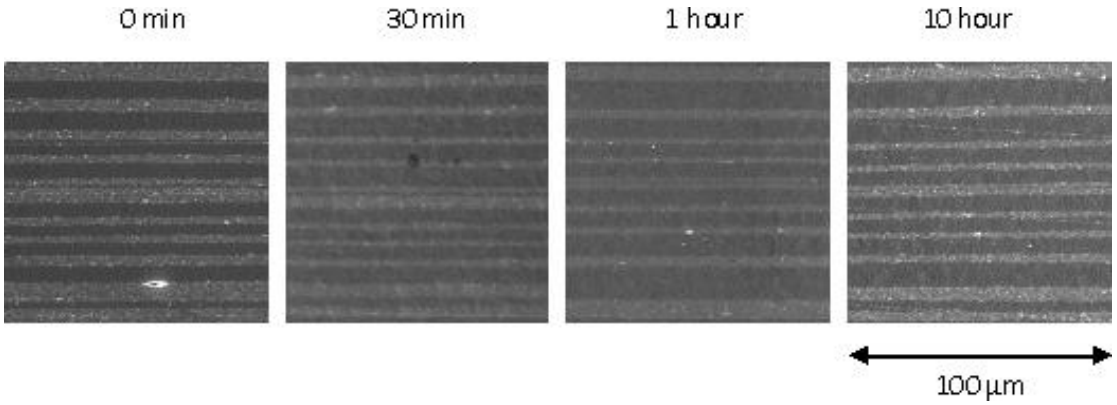

*Figure 36***.** SEM of the 65 layer multilayer annealed for 0 min, 30 min, 1 hour and 10 hours.[26]

The SEM in Figure 36 shows the LLDPE-Mica/LDPE 65 layer material annealed at 200 °C for various times. Each image shows an 100 µm×100 µm area. There are double layers in each picture which can be used as a marker to determine that the same layers were being analyzed in each image. The thickness changes of the double layers are obvious with an increase in annealing time (ie, 19.3 µm for 0 min, 17.9 µm for 30 min, 10.3 µm for 1 hour and 9.0 µm for 10 hours). However, the layers next to the double layer did not change as much (6.1 µm for 0 min, 5.0 µm for 30 min, 5.0 µm for 1 hour and 4.6 µm for 10 hours). Ideally, each filled and unfilled layers should perform the same way in the melt state, however, initial layer thickness differences, heterogeneity of the temperature in the films may result in a disparity in interdiffusion behavior for the different layers.

Thermal decomposition is generally considered to be the prelusion of combustion of materials. TGA was tested to evaluate the thermal stability of the pure polymers and nanocomposites (3%, 5%, 10% and 15% mica-LLDPE). In Figure 37(a), mass loss in

nitrogen is plotted versus temperature. Mass loss of the mica-LLDPE nanocomposites started earlier (about 300 ℃) compare to the pure LLDPE. When more mica added, the early thermal degradation is more obvious. Mass residual of LLDPE, 3% mica-LLDPE, 5% mica-LLDPE, 10% mica-LLDPE and 15% mica-LLDPE are 97.2%, 96.8%, 96.6%, 95.9% and 95.6% at 350 ℃, respectively (Table 5). From the results, one can see that early mass loss could be caused by the thermal degradation of the maleic anhydride compatibilizer and organic surface modifier of the mica. Usually, early small mass loss may be beneficial for the flame retardant properties.

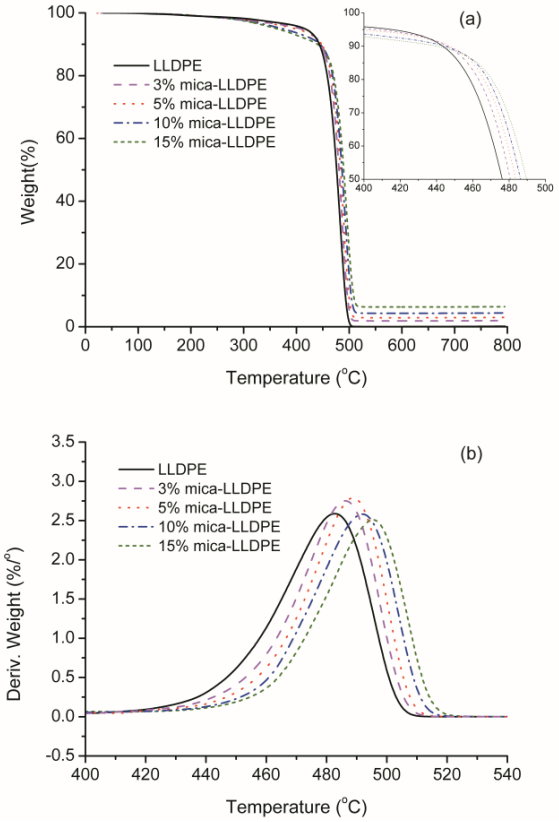

Figure 37. TGA plots of LLDPE and mica-LLDPE composites with 3%, 5%, 10% and 15% mica content in nitrogen atmosphere.

Table 5

TGA data of pure polymers, mica-LLDPE composites and multilayer materials in nitrogen.

Materials	T_{max} (℃)	$T_{50\%}$ (℃)	Mass residual at 350 ℃(%)	Mass residual at 600 ℃ (%)
LLDPE	483	476	97.2	0
LDPE	475	470	99.9	0.6
3% mica-LLDPE	486	481	96.8	1.9
5% mica-LLDPE	489	483	96.6	2.9
10% mica-LLDPE	492	486	95.9	4.3
15% mica-LLDPE	496	489	95.5	6.3
17 layers of 5% mica-LLDPE/LDPE	483	478	98.9	1.6
65 layers of 5% mica-LLDPE/LDPE	483	479	98.6	1.56

Both T_{max} (maximum mass loss temperature) and $T_{50\%}$ (50% mass loss temperature) were increased when increase mica content in the composites. Figure 37(b) shows the weight derivative curves of the LLDPE and its composites. LLDPE has T_{max} at 483 ℃ and when adding more mica particles the peaks of curves moves toward higher temperature reaching highest temperature (496 ℃) with 15% mica in the LLDPE matrix. $T_{50\%}$ of LLDPE, 3% mica-LLDPE, 5% mica-LLDPE, 10% mica-LLDPE and 15% mica-LLDPE are 476 ℃, 470 ℃, 481 ℃, 483 ℃, 486 ℃ and 489 ℃, respectively (Table 5). Thermal stability and char formation of mica nanocomposites improved by increase of mica content.

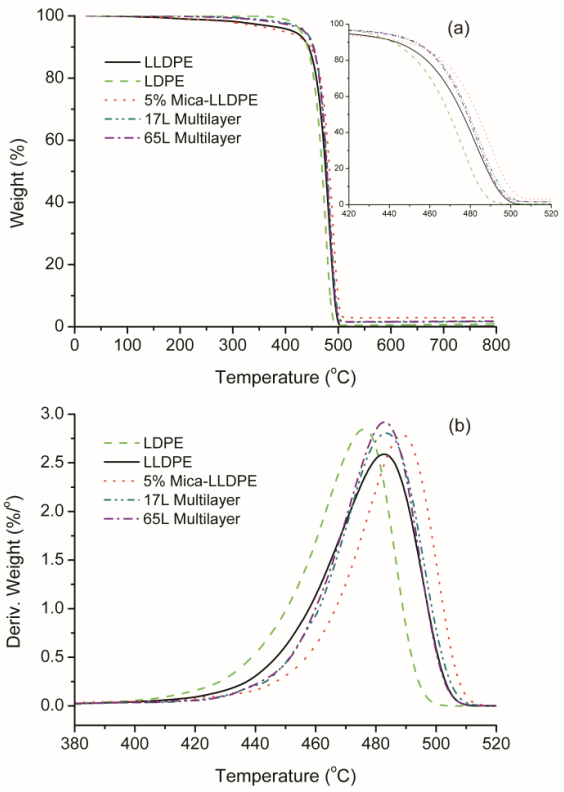

*Figure 38***.** TGA plots of pure polymers, 5% mica-LLDPE composites and multilayer materials in nitrogen atmosphere.

Thermal stability of 17 layers and 65 layers of multilayer materials were compared to the thermal stability of LDPE, LLDPE and 5% mica-LLDPE nanocomposites. LDPE was stable at 350 ℃ and did not show any weight loss at this temperature when LLDPE had about 2.8% weight loss as shown in Table 5. This is because LLDPE contains maleic anhydride modified materials and maleic anhydride has lower degradation temperature than polymers. However, LDPE have lower T_{max} and $T_{50\%}$ than LLDPE and 5% mica-LLDPE composites as shown in Figure 38(a) and Table 5. T_{max} of 17 layer and 65 layer multilayer materials lay between T_{max} of LDPE and 5% mica-LLDPE and close to 5% mica-LLDPE as shown in Figure 38(b). There is not much difference between 17 layer and 65 layer multilayer materials in TGA analysis and the corresponding TGA curves overlapped. $T_{50\%}$, mass residual at 350 ℃ and 600 ℃ are

listed in Table 5. Multilayer materials have about 2.5% mica by weight, and the TGA char formation at 800 ℃ also shows reasonable results. Thermal stability of multilayer materials is close to the 3% mica-LLDPE composites and affected by both LDPE and mica-LLDPE layers.

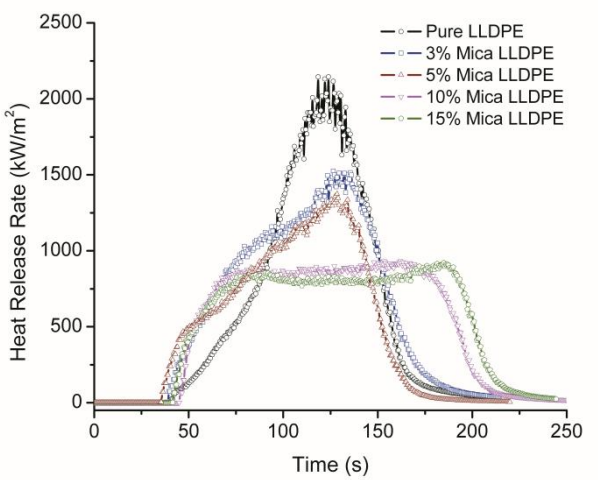

*Figure 39***.** Release rate curves for LLDPE and LLDPE composites with 3%, 5%, 10% and 15% mica conducted at an external irradiation 50 kW/m^2.

The fire behaviors of materials were determined using Cone calorimeter. Cone calorimeter measures parameters such as peak heat release rate (PHRR), time to ignition (t_{ig}), the mass loss rate (MLR), total heat released rate (THR), amount of smoke produced (SEA) and time of peak heat release rate (t_{PHRR}).

The heat release rate curves for the pure LLDPE and its nanocomposites are shown in Figure 39 and the corresponding data are given in Table 6. Pure LLDPE have high PHRR which is about 2173 kw/m^2. PHRR of the nanocomposites contained 3% and 5% mica (1.7% and 2.8% inorganic mica) show a small reduction (about 30%) compare with the pure polymer. Better flame retardant properties were obtained with the higher mica content. When the loadings of the mica reached 10% and 15% (5.6% and 8.4% inorganic mica), LLDPE-mica composites showed about 60% reductions in PHRR. There

is not much difference between 10% and 15% mica-LLDPE composites in PHRR, adding more than 10% mica did not further improve flame retardant properties which may caused by the pure dispersion of mica in 15% mica composites as shown previously in TEM pictures.

Cone tests of MMT contained PE and PP composites were reported previously.[28] With 3%, 8% and 13% organic modified MMT (1.1%, 3.0% and 4.5% inorganic content), PHRR decreased by 15%, 25% and 45% in PE composites compare to the pure PE and 17%, 31% and 40% in PP composites compare to the pure PP at 35 kW/m^2 heat flux. Morgan and his coworkers reported flammability of mica contained polystyrene systems.[13] With 9.3% modified mica (5% inorganic content) in the Polystyrene system, heat release rate decreased by 60% compared to the pure polystyrene at 35 kW/m^2 heat flux.

Other parameters are listed in Table 6. The t_{ig} of mica-LLDPE composites increased compare to the pure LLDPE, however, the improvement is not significant. Previously reported that time to ignition of composite with layered silicate (MMT or mica) in the polymer systems decreased when increasing the inorganic content.[13,28] The fire property improvement is either improving PHRR or t_{ig} for the materials, in this study only PHRR was improved with the t_{ig} remained the same value. Total heat release did not change according to the cone test. The amount of smoke was increased by increasing mica amount. This is cause by incomplete combustion of polymers, which may also related to the additives in the polymer matrix.

Table 6

Cone calorimeter results of polymers, nanocomposites and multilayer materials.

Formulation	HRR (kW/m^2)	Reduct (%)	AMLR ($g/m^2.s$)	t_{ig} (s)	t_{PHRR} (s)	SEA (m^2/kg)	THR (MJ/m^2)	Char (%)
LLDPE	2173±40	-	29.5±0.4	44±1	123±1	325±13	125±0	0
3wt% Mica-LLDPE	1565±57	28	25.1±1.9	42±2	127±6	407±23	128±1	1.4
5wt% Mica-LLDPE	1473±143	32	25.3±0.6	44±5	131±6	386±0	126±2	-
10wt% Mica-LLDPE	936±18	57	17.8±2.2	49±2	159±5	454±35	125±0	4.9
15wt% Mica-LLDPE	953±60	56	17.5±0.7	46±1	178±6	443±8	124±2	6.1
LDPE	2662±205	-	39.3±1.1	53±3	116±5	265±9	126±2	-
17 layer multilayer (20 um) 5% mica-LLDPE/LDPE	1083±76	50	20.0±1.8	63±2	139±7	423±43	120±4	-
65 layers multilayer (5 um) 5% mica-LLDPE/LDPE	1055±57	51	20.2±0.5	53±3	115±5	365±7	119±1	-

There are four ways to improve flame retardant properties: Gas phase radical quench, endothermic degradation, dilution of gas phase and condense phase thermal shielding. These nanocomposites improve flame retardant properties by thermal shielding. Inorganic particles form condense phase to prevent the oxygen reaching polymers and also trap decomposed molecules inside the materials. In this case, PHRR decreases along with mass loss rate decrease because combustion speed will be decreased. Both PHRR and AMLR decreased by adding more and more mica into the polymers because more condensed mica layers were created during combustion.

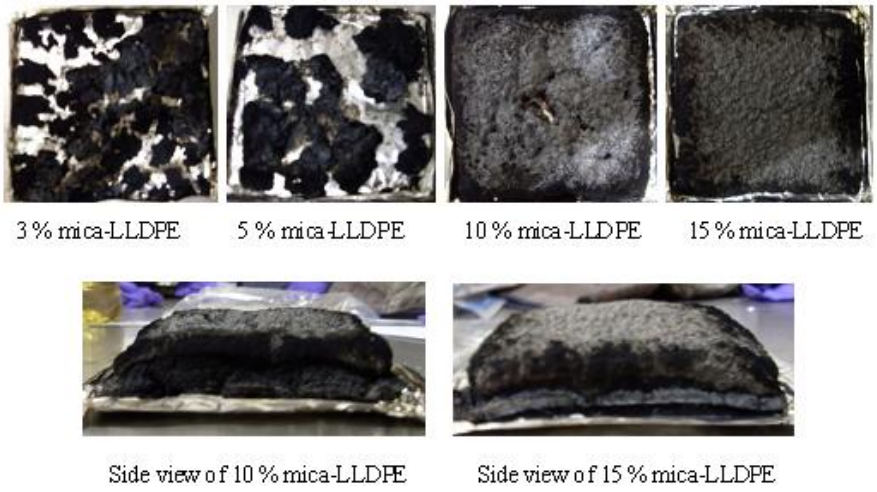

*Figure 40***.** Images of the residues of mica-LLDPE composites with 3%, 5%, 10% and 15% mica content (top view and side view).

Figure 40 shows the char residue of mica-LLDPE composites after combustion. 3% and 5% mica-LLDPE composites do not have condensed char residues while 10% and 15% mica-LLDPE composites showed thick and condensed char morphology. These char morphology can be correlated with the PHRR data. Low mica content composites did not show continuous char morphology compared to high mica content composites. Char consists of inorganic particles and incompletely combusted polymers. Condensed char can prevent oxygen penetrate the burning polymer and an impermeable barrier char layer also can prevent small molecules of pyrolysis from getting out of the polymers. Formation of the char layers may be main reason that PHRR was decreased for high loading composites.

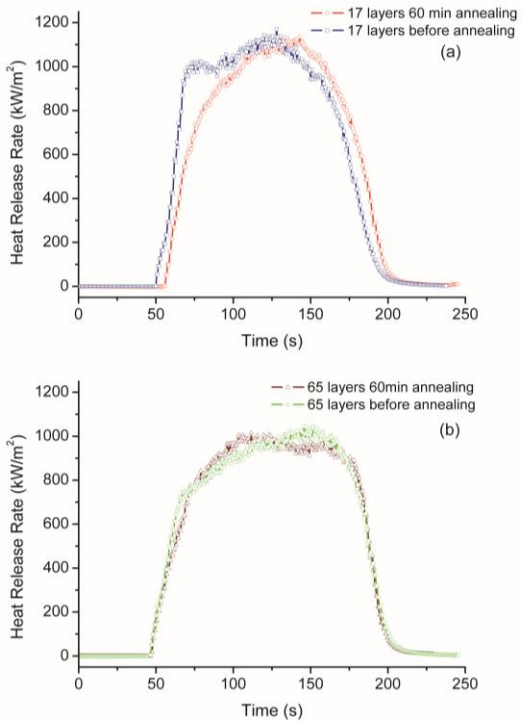

*Figure 41***.** Heat release rate of multilayer materials (a) 17 layers and (b) 65 layers before and after annealing.

The 17 layers and 65 layers multilayer materials were evaluated for flame retardant properties and the heat release rate curves are shown graphically in Figure 41. PHRR of these materials were about 1000 kW/m^2 and materials showed the same PHRR before and after annealing. 17 Layer and 65 layer multilayer materials indicated similar heat release rate behaviors which mean the layer thickness difference did not play really significant role in the range of as thin as micro scale. As shown previously in Figure 35 and Figure 36, for both 17 layers and 65 layers filled layers become thinner after 60 min annealing due to moving boundary effect between LLDPE and LDPE layers. This caused increase of particle concentration in the LLDPE layers and PHRR expected to be lower for annealed films than unannealed film. However, experimental data shows that unannealed and annealed films perform similarly in cone test.

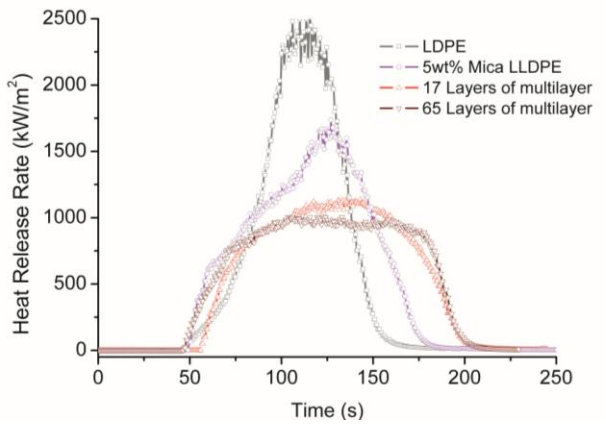

*Figure 42***.** Heat release rate of LDPE, 5% mica-LLDPE, 17 layer and 65 layers mica-LLDPE/LDPE multilayer materials.

The heat release rate of multilayer materials, mica-LLDPE and LDPE are compared in the Figure 34. The PHRR of LDPE and 5% mica-LLDPE were 2662 kW/m^2 and 1473 kW/m^2, respectively. However, multilayer materials show PHRR around 1000 kW/m^2 which is lower than both of the individual layers. Multilayer materials Multilayer materials consist two different polymer and composites layers: LDPE and 5% mica-LLDPE. Multilayer materials contain only 2.5% mica (about 1.4% inorganic mica) in total polymer composites. This decrease of PHRR is significant for this amount of nanoparticles in the materials because at least 10% nanoparticles are needed in the system to achieve similar decrease of PHRR. Increase total amount of particles are important to improve reduce PHRR value; however, it is more important to increase concentration of particles in effective area and effective ways. The possible reason of the high flame retardant improvement with small amount of mica is that prior to ignition melted polymers interdiffusion to each other layers and causes moving boundary of the layers in less than 50 s exposed to high temperature conditions. Moving boundary of layers induced particle concentration in the filled layers fully covered combustible LDPE layers.

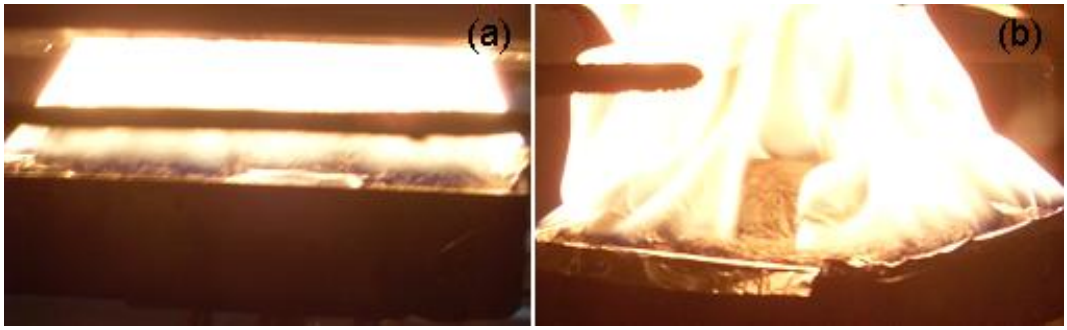

*Figure 43***.** Picture of flame for 10% (a) mica-polybond composites and (b) multilayer materials during the cone calorimetry test at 50 kW/m^2 heat flow.

The Flame of multilayer materials was different compare to the composites as shown in Figure 43. When the nanocomposites burning, the flame was solid and covered the entire surface as shown in Figure 43(a). During the combustion of the multilayer materials, flame was week in the center part of the materials and strong in edge of the materials (Figure 43(b)). This indicate these type of materials prevent flame very well in the direction perpendicular to the surface and not as good in the direction parallel to the surface. Film surface is better flame retardant because of the mica nanoparticles in the parallel layers prevent the decomposed polymers escaping from the inside of the film to the film surface, however, the side of the film is not fully covered by the nanoparticles. Moreover, plate-like shaped nanoparticles have orientation parallel to the film surface in the layers.

Char leftover after combustion of the multilayer materials are shown in Figure 44. Multilayer materials showed thick and continuous char formation with only 2.5% mica in the materials. Nanocomposites with 5% mica do not form char and nanocomposites with 10% mica showed similar char formation as shown previously in Figure 41. Multilayer materials forming thick char with much less nanoparticles in the polymer systems compare to nanocomposites. This results were correlated to the PHRR results. To form

thick char, not only total amount of nanoparticles in the polymers are important, but also the effective particle concentration are matters.

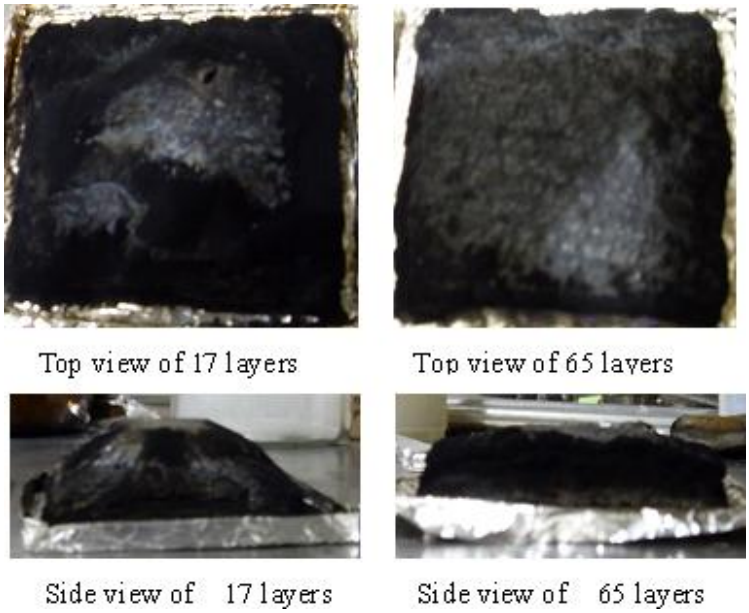

*Figure 44***.** Images of the residues of 17 layers and 65 layers multilayer materials (top view and side view).

In order to observe the layer structures during the polymer decomposition and demonstrate moving boundary effect, a 17 layer multilayer material film was heated at 450 ℃ in the nitrogen for about 30 s. The cross section of the annealed film was observed using SEM. At the temperature higher than 450 ℃, the film was burn to leave only black char while the multilayer material was not burned out at 450 ℃. The SEM of multilayer material before annealed and after annealed at 450 ℃ was shown in Figure 45. The mica filled layer thickness was about 20 μm before annealing however, after annealing at 450 ºC for really short time the filled layers shrunken to about 10 μm which indicate fast interdifusion and boundary movement occurred. The layers were not uniform and straight because fast diffusion coefficient under this temperature.

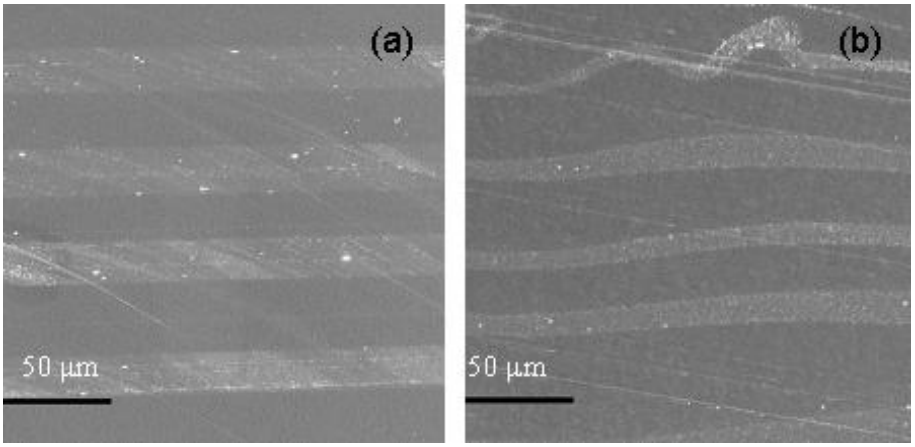

*Figure 45***.** Layer structure of 17 layer multilayer materials before annealing and after annealing at 450 ℃.

Figure 46 shows heat release rate of the 7 alternating layers of LDPE and 5% mica-LLDPE materials. These materials were not processed using layer multiplying co-extruder but made by stacking 7 thin films together using compress molding. The individual layer thickness is about 300 μm which is much thicker than multilayer materials (20 μm and 5 μm) produced by the co-extruder. As expected, flame retardant property improvement was not observed due to thickness of the layers. The PHRR of these materials were in the same range of pure LLDPE. Interdiffusion time depends on the thickness of the layers that longer time is need for thicker layers to show moving boundary effect. PHRR of 7 layer materials before and after annealed were about 2200 KW/m^2 and char formation were not solid and continuous as shown in Figure 46. Flame retardant properties and moving boundary effect were highly related to the scale of layer thicknesses and when the layer thickness is too large, the layered materials burn as nanocomposites not multilayer materials.

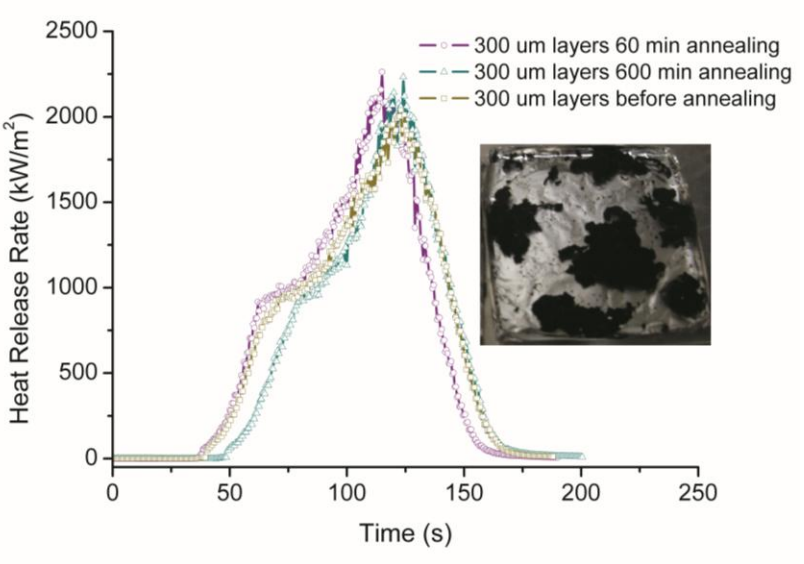

*Figure 46***.** Heat release rate of compressed molding 7 layers material with single layer thicknesses about 300 μm before annealing and annealed for 60 min and 600 min.

Figure 47 schematically showed combustion behaviors of nanocomposites and multilayer materials in cone test. Polymers pyrolyse to generate flammable molecules when exposed to sufficient heat. These molecules mix with oxygen to form an ignitable blend which ignited at the presence of an external source (flame or spark). In nanocomposites, flammability decreased due to the development of a carbonaceous char structure on the surface during the combustion.The carbonaceous char produced superficially generates a physical barrier which protects nanocomposites from heat and oxygen, and slows down the escape of flammable volatiles generated during polymer pyrolysis. Char formation and significant decrease of PHRR happens only when there are enough silicate nanoparticles. Multilayer materials contained LLDPE-mica and LDPE enhance the flame retardant effect of nanocomposites by concentrating the particles and multiplying the physical barrier (char) layers. Multilayer materials showed moving boundary phenomena when expose to high temperature as mentioned previously. The moving boundary effect concentrate nanoparticles in the filled layers and enhance the

char formation on the surface. The flame size was decreased due to stronger char barrier. Smaller flame generated less heat correspondly which feed back to the polymer materials. The char layers can be generated for each of filled layers for 17 layer and 65 layer multilayer materials. Polymer, on the bottom of the layers, was protected by the multiple physical barriers which strongly prevent flammable decomposed molecules from escaping and mix with oxygen. Multilayer materials have much thicker char formation and smaller flame than conventional nanocomposites.

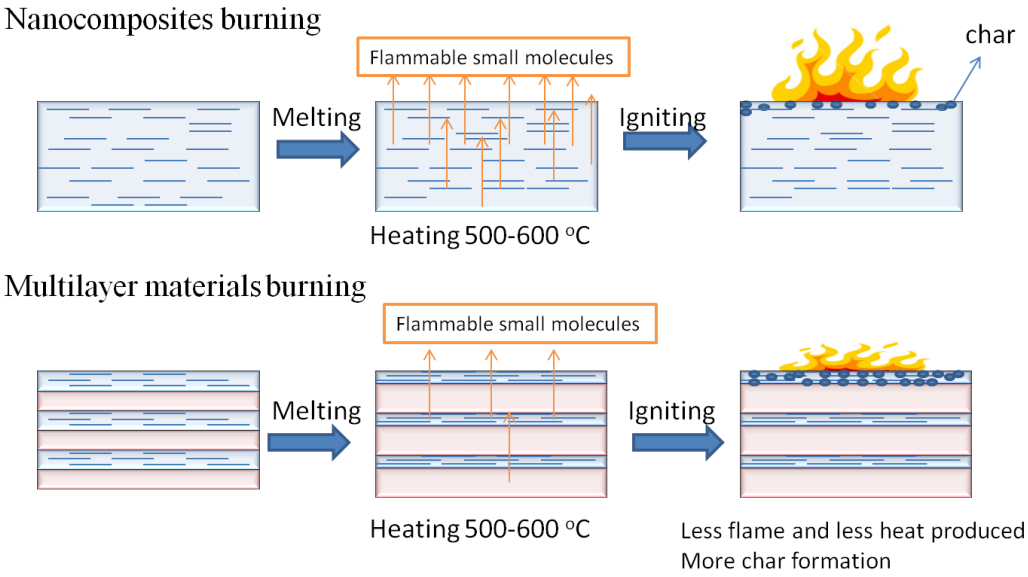

Figure 47. Mechnism of burning of nanocomposites and multilayer materials.

Conclusions

Surfactant modified Mica was able to be exfoliated in the LLDPE polymer matrix. Nanocomposites morphology was observed using TEM which shows near exfoliated nanocomposites system with 5% mica and intercalated nanocomposites system with 10% mica. High aspect ratio mica improved the thermal stability and flame retardancy of LLDPE. The temperature at 50% weight loss and at maximum weight loss rate in nitrogen of the nanocomposite filled with 5% (wt/wt) and 15% (wt/wt) modified mica

was 6 ℃ and 13 ℃ higher than that of neat LLDPE. PHRR of 5% and 10% mica composites decreased by 32% and 57% compare to neat LLDPE. Nanocomposites and LDPE were multilayered in alternating layers of 17 layers and 65 layers. Moving boundary was observed between LLDPE-Mica layers and LDPE layers after annealing these multilayer materials at 200 ℃ for different time. Mica filled LLDPE layers were shrunk while LDPE layers were swelled before combustion exposed to high temperature. Multilayer materials consisted alternating layers of mica filled LLDPE and pure LDPE had improved flame retardant properties with only 2.5% (wt/wt) of mica. The char formation and PHRR results were similar to the nanocomposites with high loading of mica. Multilayer technique and moving boundary effect allowed the low loading multilayer material worked as high loading nanocomposites with same amount of inorganic fillers.

REFERENCES

1. Mack, A. G. FlameRetardants, Halogenated.In *Kirk-Othmer Encyclopedia of Chemical Technology (5th Edition)*; Seidel, A.; John Wiley & Sons, Inc.: Hoboken, NJ, **2005**, Vol 11, 454–483.
2. Rahatekar, S. S.; Zammarano, M.; Matko, S.; Koziol, K. K.; Windle, A. H.; Nyden, M.; Kashiwagi, T.; Gilman, J. W. Effectof Carbon Nanotubesand Montmorilloniteon The Flammability of Epoxy Nanocomposites. *Polym. Degrad. Stab.* **2010**, *95*, 870–879.
3. La Rosa, A. D.; Recca, A.; Carter, J. T.; McGrail, P. T. An Oxygen Index Evaluation of Flammability on Modified Epoxy/Polyester Systems. *Polymer* **1999**, *40*, 4093–4098.
4. Schartel, B.; Braun, U.; Balabanovich, A. I.; Artner, J.; Ciesielski, M.; Doering, M.; Perez, R. M.; Sandler, J. K. W.; Altstaedt, V. Pyrolysis and Fire Behavior of Epoxy Systems Containing A Novel 9,10-Dihydro-9-Oxa-10-Phosphaphenanthrene-10-Oxide-(DOPO)-Based Diamino Hardener. *Eur. Polym. J.* **2008**, *44*, 704–715.
5. Nara, S.; Matsuyama, K. Thermal Degradation and Flame Resistivity of Tetrabrominated Epoxy Resin. *J. Macromol. Sci.: Part A - Chem.* **1971**, *5*, 1205–1218.
6. Gilman J.W. Flammability and Thermal Stability Studies of Polymer-Layered Silicate (Clay) Nanocomposites. *Appl. Clay Sci*. **1999**, *15*, 31–49.
7. Gilman J.W.; Jackson C.L.; Morgan A.B.; Harris Jr R.; Manias E.; Giannelis E.P,; Wuthenow M.; Hilton D.; Phillips S.H. Flammability Properties of Polymer-Layered Silicate Nanocomposites. Polypropylene and Polystyrene Nanocomposites. *Chem.*

Mater. **2000**, *12*, 1866–1873.

8. Zhang, J.; Wilkie, C. A. Preparation and Flammability Properties of Polyethylene-Clay Nanocomposites.*Polym. Degrad. Stab.* **2003**, 80, 163–169.
9. Cheng H. Yu.; Jiang G. J.; Hung J. EnhancedMechanical and ThermalProperties of PS/Mica and PMMA/MicaNanocomposites by Emulsion Polymerization. *Polym.Compos.* **2009**, *30*, 351–356.
10. Chang J.; Mun M. K. Nanocomposite Fibers of Poly(Ethylene Terephthalate) with Montmorillonite and Mica: Thermomechanical Properties and Morphology. *Polym. Int.* **2007**, *56*, 57–66.
11. Soon, K.; Harkin-Jones, E.; Rajeev, R. S. Morphology, Barrier, and Mechanicalproperties of Biaxially Deformed Poly(Ethylene Terephthalate)-Mica Nanocomposites. *Polym. Eng. Sci.* **2012**, *52*, 532–548.
12. Xanthos, M; Faridi, N; Li, Y. Processing/Structure Relationships of Mica-Filled PE-Films with Low Oxygen Permeability. *Int. Polym. Proc.* **1998**, *13*, 58–66.
13. Morgan, Alexander B.; Chu, Lih-Long; Harris, Joseph D. A Flammability Performance Comparison Between Synthetic and Natural Clays in Polystyrene Nanocomposites. *Fire Mater*. **2005**, *29*, 213–229.
14. Mueller, C. D.; Nazarenko, S.; Ebeling, T.; Schuman, T. L.; Hiltner, A.; Baer, E. Novel Structures by Microlayer Coextrusion-Talc-Filled PP, PC/SAN, and HDPE/LLDPE. *Polym. Eng. Sci.* **1997**, *37*,355–362.
15. Ma, M.; Vijayan, K.; Hiltner, A.; Baer, E.; Im, J. Thickness Effects in Microlayer Composites of Polycarbonate and Poly(Styrene-Acrylonitrile). *J. Mater. Sci.* **1990**, *25*, 2039–2046.

16. Sung, K.; Hiltner, A.; Baer, E. Three-dimensional Interaction of Crazes and Micro-shearbands in PC-SAN Microlayer Composites. *J. Mater. Sci.* **1994**, *29*, 5559–5568.
17. Sekelik, D. I.; Stepanov, E. V.; Nazarenko, S.; Schiraldi, D.; Hiltner, A.; Baer, E. Oxygen Barrier Properties of Crystallized and Talc-Filled Poly(ethylene terephthalate). *J. Polym. Sci., PartB: Polym. Phys.* **1999**, *37*, 847–857.
18. Jarus, D.; Hiltner, A.; Baer, E.; Microlayer Coextrusion as A Route to Innovative Blend Structures. *Polym. Eng. Sci.* **2001**, *41*, 2162–2171.
19. Jarus, D.; Hiltner, A.; Baer, E. Barrier Properties of Polypropylene/Polyamide Blends Produced by Microlayer Coextrusion. *Polymer* **2002**, *43*, 2401–2408.
20. Nazarenko, S.; Dennison, M.; Schuman, T.; Stepanov, E. V.; Hiltner, A.; Baer, E. Creating Layers of Concentrated Inorganic Particles by Interdiffusion of Polyethylenes in Microlayers. *J. Appl. Polym. Sci.* **1999**, *73*, 2877–2885.
21. Mueller, C.; Kerns, J.; Ebeling, T.; Nazarenko, S.; Hiltner, A.; Baer, E. Microlayer Coextrusion: Processing and Applications. *Polymer Process Engineering*. Coates, P. D., Eds.;Vol. 97. London: Bradford, **1997**, 137–157.
22. Schuman, T.; Nazarenko, S.; Stepanov, E.V.; Magonov, S.N.; Hiltner, A.; Baer, E. Solid State Structure and Melting Behavior of Interdiffused Polyethylenes in Microlayers. *Polymer* **1999**, *40*, 7373–7385.
23. Schuman, T.; Stepanov, E.V.; Nazarenko, S.; Capaccio, G.; Hiltner, A.; Baer, E. Interdiffusion of Linear and Branched Polyethylene in Microlayers Studied via Melting Behavior. *Macromolecules* **1998**, *31*, 4551–4561.
24. Keskkula, H.; Paul, D. R.; Young, P.; Stein, R. S. Diffusion of Miscible Polymers in Multilayer Films. *J. Appl. Polym. Sci.* **1987**, *34*, 1861–1877.

25. Nazarenko, S.; Dennison, M.; Schuman, T.; Stepanov, E. V.; Hiltner, A.; Baer, E. Creating Layers of Concentrated Inorganic Particles by Interdiffusion of Polyethylenes in Microlayers. *J. Appl. Polym. Sci.* **1999**, *73*, 2877–2885.
26. Wu Y.; Meyers K.; Nazarenko S. Mica Filled Multilayered Composites with Enhanced Gas Barrier Properties. In preparation.
27. Gilman, J. W.; Kashiwagi, T.; Nyden, M.; Brown, J. E. T.; Jackson, C. L.; Lomakin, S.; Giannelis, E. P.; Manias, E. Flammability Studies of Polymer Layered Silicate Nanocomposites: Polyolefin, Epoxy, and Vinyl Ester Resins. In *Chemistry and Technology of Polymer Additives*; Malden, MA, Ak-Malaika, S., Golovoy, A., Wilkie, C. A.; Blackwell Science Inc.: Blackwell Oxford, UK, **1999**, 249–265.
28. Zhang, J.; Jiang, D. D.; Wilkie, C. A. Thermal and Flame Properties of Polyethylene and Polypropylene Nanocomposites Based on An Oligomerically-Modified Clay. *Polym. Degrad. Stab.* **2005**, *91*, 298–304.

CHAPTER VI

FIRE RETARDANT EFFECT OF ZINC BASED COMPOUNDS ADDED TO AN EPOXY-AMINE THERMOSET

Abstract

Zn containing compounds zinc acetate (ZnAc), zinc undecylenate (ZnUnd) and Zinc stearate (ZnSt) have been studied for thermal degradation and flame retardant properties on standard epoxy/amine systems. The zinc salts had improved flame retardant properties (decreased peak heat release rate (PHRR), smoke emission and improved char formation) on epoxy/amine systems and the flame retardant efficiency order was ZnAc, ZnUnd and ZnSt. Char of ZnUnd epoxy/amine composites had protecting zinc oxide layers on the surface which forming physical barrier for the flame. SEM and X-ray were used to further understand the mechanism of zinc salts on flame retardant properties.

Introduction

Epoxy resins have great adhesive, mechanical, thermal, gas barrier and chemical resistance properties which are widely used in the aerospace and electronics area.[1-4] However, the flammability of epoxy resins limited the application of these materials in various industrial areas. The flammability of the epoxy needs to be improved without sacrificing the other important properties, especially mechanical properties. Epoxy flammability was improved by flame retardant additives, such as halogenated, nanoparticles and phosphorus types of additives, or by copolymerization.[5-9] Epoxy blends with additives are more convenient for industrial used; however, copolymers have advantage in maintaining physical properties.

Metal based materials were studied for flame retardant properties for polymeric systems. Recently, Morgan summarized the recent findings on fire retardancy effectiveness of metal oxides, metal salts and metal complexes in his review article. Metal salt worked as flame retardant in both gas and condense phase to reduce flammability.[10] Some of the metals were able to produce free radicals to quench fire, also, metal salt formed nice physical barrier on the surface of the polymer to prevent the flammable small molecules from escaping to the surface. Metal based materials are friendly to the environmental without releasing any toxic gas upon combustion which can be good replacement of halogenated flame retardant.

There are many publications on metal oxide and metal hydroxide based flame retardant. Among the metal hydroxides that can be used as flame retardants in polymer materials, the most important are magnesium hydroxide [$Mg(OH)_2$] and aluminum hydroxide [$Al(OH)_3$].[11] Generally, the flame-retardant mechanism of metal hydroxide is releasing water vapor during decomposition in the fire which isolates the flame and dilutes the flammable gases in the gas phase. Metal hydroxides and oxide have similar flame retardant properties on polymeric systems. Flame retardants such as CaO, MgO, and MgO/CaO only can increase the LOI marginally (about 0.5 unit), and ZnO at the same level as an Sb_2O_3 has an intermediate effect on the LOI increasing it by 2.5 units in PVC systems.[12] Good synergy between Sb_2O_3 and ZnO has been found and improvement of char formation was observed. The metal hydroxide and oxide not only reduce the peak heat release rate (PHRR) but also suppresses the emission of smoke.[13]

Yu and his coworkers[14] studied metal acetate on polypropylene-modified lignin composites. Cone calorimeter results indicate that the presence of $Ni(Ac)_2$ shortens

slightly the time to ignition from 38 s to 31 s and it reduces the PHRR from 380 kW/m^2 to 330 kW/m^2, significantly increases char residue by 44% and increases the LOI value from 22 for PP/functionalized lignin (17.5 for pure PP) up to 26, also indicating a better flame retardancy. However, it has some serious disadvantages such as relatively lower flame-retardant efficiency and thermal stability, and great deterioration in the physical/mechanical properties. In order to improve the flame retarding efficiency and decrease the loading level of metal hydroxide and oxide, some synergists with metal compounds were widely investigated.

Zn containing flame retardants were not well known and only a few of the studies were on polymer flammability improvement by adding metal salts into the polymers. Flame retardancy of different kinds of thermosets can be ensured by the addition of zinc compounds due to the reduced toxicity and low smoke emission. Zinc hydroxystannate (ZHS) and zinc stannate (ZS), have found application as flame retardants in a range of plastics, rubbers and paint formulations. The zinc salt can be used synergetic with metal oxide, halogenated flame retardant or phosphate flame retardant.[15] With 5% to 40% filler content, with a maximum change of about 50% (from 382 to 148 kW/m^2) in the case of 40% of ZB in the epoxy systems. The ZS and ZHS act by a condensed phase mechanism, the volatilisation of the additives from the degrading halogenated polyesters suggest that a vapor phase mechanism possible.[16]

In this study, Zn salts with different organic chain were blended with the standard epoxy/amine systems. Thermal degradation and flame retardant test was conducted using TGA and cone calorimetry. The PHRR, Mass loss rate, smoke, char formation were investigated for ZnUnd epoxy/amine composites. Surface and bulk of the char and

quenched cone samples were analyzed using SEM and SEM-EDX. Mechanism of Zn salts on flame retardancy was proposed and investigated based on ZnUnd composites.

Experimental

EPON 826, a low viscosity liquid epoxy resin often used in coatings and composite applications with an epoxy equivalent weight of 178-186 grams and molecular weight about 700 g/mol was supplied by Hexion. The hardener, Jeffamine D230, with an amine equivalent weight of 60 grams, was supplied by the Huntsman Corporation. Density of EPON 826 and Jeffamine D230 are 1.16 g/ml and 0.948 g/ml at 25 ℃, respectively. The molecular structure is shown in Scheme 1.

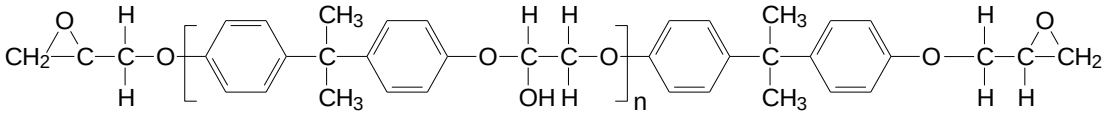

Epon (TM) Resin 826 (Reaction product: bisphenol-A-(epichlorhydrin))

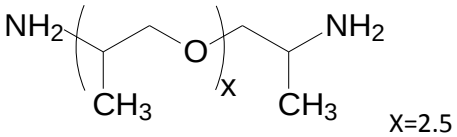

Jeffamine D230 Amine hardener

Scheme 1. Structures of epoxy and harderner.

Zinc acetate dihydrate [$Zn(C_2H_3O_2)_2.2H_2O$] (ZnAc), zinc undecylenate [$C_{22}H_{38}O_4Zn$] (ZnUnd) and zinc stearate [$C_{36}H_{70}O_4Zn$] (ZnSt) were purchased from Aldrich Chemical Company with molecular weight 219.51 g/mol, 431.92 g/mol and 632.33 g/mol ZnAc, ZnUnd and ZnSt are in powder form and showing white color at room temperature.

The composites were prepared as follows: the additives were mixed directly in bisphenol A epoxy resin for several minutes at 60 ^{o}C. The additives were dispersed with a mechanical stirrer. The hardener was added to the mixture in a stoichiometric amount and

stirring continued for an additional 30 minutes at room temperature before the contents of the were poured into a mold. The samples were cured at 80 ^{o}C for 12 hours and post cured at 135 ^{o}C for an additional 3 hours. Prior to curing, the mold containing the mixed reactants was degassed in vacuum to remove any trapped air. Epoxy/amine composites with 4%-27% fillers were made and tested for properties.

A TA instruments Q500 thermogravimetric analyzer (TGA) was used to evaluate the thermal stability of the networks and the additives. The samples (~10 mg) were tested in the nitrogen environments at a heating ramp rate of 10 ^{o}C/min from 25 to 600 ^{o}C.

Cone calorimeter measurements were performed with the Govmark cone instrument according to ASTM E 1354 using a cone shaped heater with an incident flux set at 50 kW/m^2. The exhaust flow was set at 24 L/s and the spark was turned on continuously until the sample was ignited. Cone samples have the same size $10 \times 10 \times 3$ cm^3 for all the metal containing epoxy-amine polymers. Typically the data generated by a cone are quite reproducible with an uncertainty which does not exceed $\pm 10\%$.[17] A set of fire-relevant parameters can be obtained using the cone calorimeter including the peak heat release rate (PHRR), average mass loss rate (AMLR), average specific extinction area (ASEA), time to ignition (t_{ig}), carbon monoxide yield, and specific heat of combustion.

Partially pyrolyzed samples were prepared using cone calorimeter. The samples were exposed to a 50 kW/m^2 heat flux in the cone for limited periods of time, and then removed and quenched using liquid nitrogen for study. The exposed times were 10 s, 15 s, 20 s and 30 s for epoxy/amine/ZnUnd composites.

Scanning Electron Microscopy (SEM) was performed to the additives, surface of char and partially pyrolyzed samples using a FEI Quanta 200 SEM. SEM samples were prepared and coated using gold spatter coating instrument prior to the image taking. SEM thermo scientific NSS 7 EDX was used to analyze the surface elements of the char and partially pyrolyzed smaples.

Results and Discussion

Figure 48 shows the SEM of the ZnAc in big and small magnification. Zinc salts (ZnAc, ZnUnd and ZnSt) used in the study are white power at room temperature. The powder was stick to the SEM holder forming really thin layer and sputter coated of gold before took SEM pictures. ZnAc are micro sized particles and gathered to make even bigger size aggregates as shown in Figure 48. ZnAc particle length is 200 to 300 μm and thickness is 30 μm.

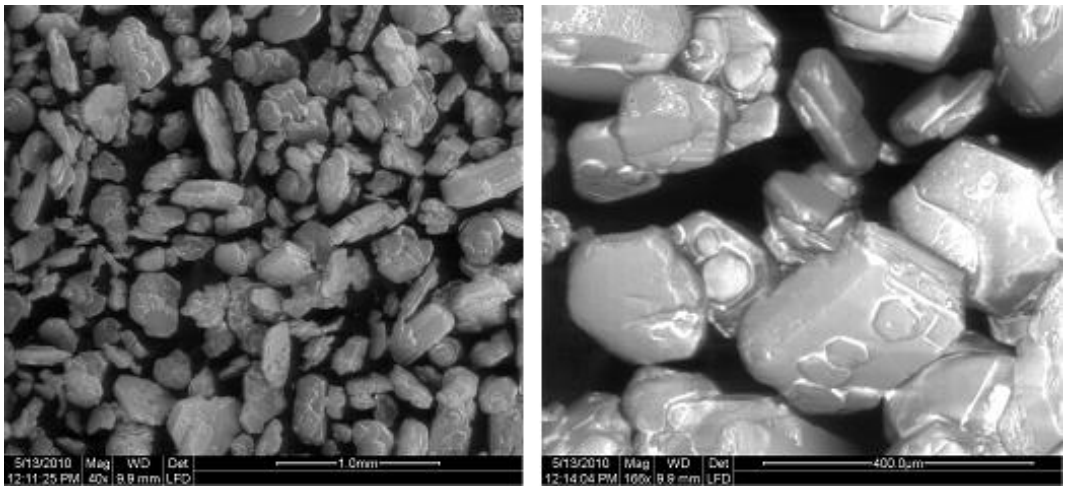

Figure 48. SEM of Zinc acetate and dehydrate (ZnAc) at different magnification.

Metal oxide and metal do not decomposed under high temperature, however, metal salt with organic chain decompose under high temperature. Different types of metal salt have different metal content. The amount of organic chain can be calculated using

TGA analysis. Figure 49 shows TGA of three different types of Zinc salts under nitrogen atmosphere. ZnAc shows two types of decomposition processes. Water molecules are eliminated at temperature range of 55-100 ℃. Weight loss goes rapidly at the temperature 160 ℃ to 190 ℃ in the second stage. The first stage lost of 15% of weight and second stage lost about 65% of weight. ZnUnd and ZnSt also show two types of decomposition process. ZnUnd has first decomposition at temperature 200 ℃ to 300 ℃ and second decomposition at 300 ℃ to 450 ℃. ZnSt has first decomposition started at 250 ℃ and second decomposition at 350 ℃. Both of the particles have about 19% weight remained as residual which is much less than metallic zinc. This is because part of the zinc metal has been volatilized during decomposition reaction. This observation also reported in the previews papers.[18] From the TGA results, Zinc salt is stable at temperature up to 200 ℃ which is higher than the curing temperature of epoxy-amine polymers.

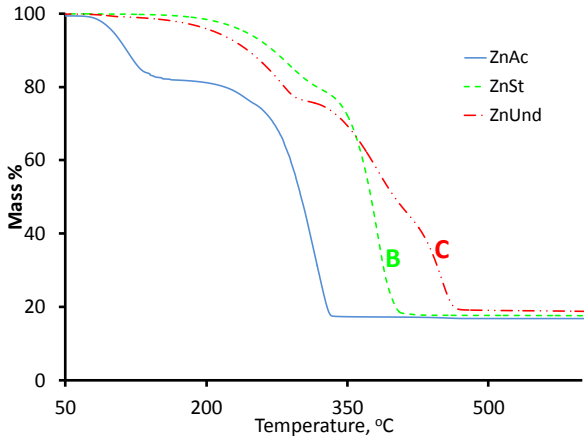

*Figure 49***.** TGA curves of ZnAc, ZnSt and ZnUnd in the nitrogen atmosphere.

Thermal decomposition property is generally considered to be the prelusion of combustion of materials. TGA was tested to evaluate the thermal stability and char formation of the epoxy/amine polymer and metal salt containing epoxy/amine composites. Mass loss in nitrogen is plotted versus temperature in Figure 50. Epoxy-amine has

thermal degradation temperature above 350 ℃ which is thermally stable polymer. TGA curves of Epoxy-amine composites with 10% ZnSt, 7% ZnUnd and 4% ZnAc were also shown in Figure 50. The corresponding metal content is about 1% for all of these composites as listed in Table 7. Thermal degradation temperature was decreased by adding metal salts. Both $T_{10\%}$ (10% mass loss temperature) and $T_{50\%}$ (50% mass loss temperature) were decreased when adding the metal salts to the epoxy matrix as shown in Table 8. The effect of three metal salts on thermal stability of epoxy-amine system is similar with only slight difference. The changes are due to the organic chain in metal salts which decompose at lower temperature compare to the epoxy-amine polymer.

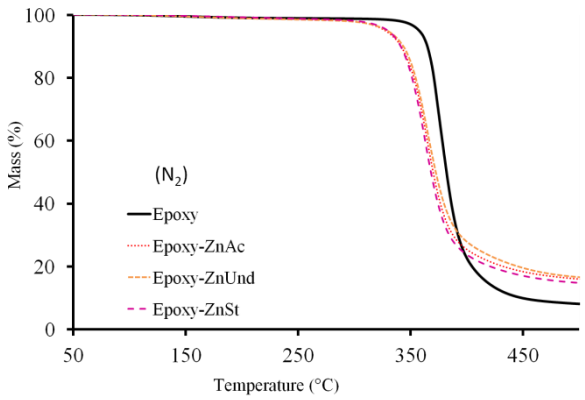

*Figure 50***.** TGA curves of epoxy/amine metal salt composites with 10% ZnSt, 7% ZnUnd, 4% ZnAc and 4% CoAc.

Residual for pure polymer is 7% under the N_2 atmosphere at 500 ℃. Char formation enhanced by adding these metal salts as shown in Table 8. The metal content was only 1%, however, about 7% more char formation was observed. Zn and Co help to increase the carbonaceous residual which is good sign for fire retardant properties. ZnUnd has most char formation and ZnSt has less char formation, however, the difference is not significant

Table 7

Metal salts and epoxy/amine metal salts composites.

	Formula	MW	Metal (Zn or Co) in Metal salt (wt%)	Metal salt in epoxy-amine composites (wt%)	Corresponding Zn (wt%)
Zinc stearate	$C_{36}H_{70}O_4$ Zn	632.3	10.3	10	1.03
Zinc undecylenate	$C_{11}H_{20}O_2$ 1/2 Zn	431.0	15.2	7	1.06
Zinc acetate	$C_4H_6O_4Zn.2H_2O$	219.5	29.8	4	1.19

Table 8

TGA data of epoxy/amine/metal salt composites in nitrogen.

Material	$T_{10\%}$ (^oC)	Delta	Stdev	$T_{50\%}$ (^oC)	Delta	Stdev	Char	Stdev
Epoxy/amine	362	N/A	4	380	N/A	3	7	1
Epoxy/amine/4%ZnAc	340	-22	2	369	-10	1	15	0.3
Epoxy/amine/7%ZnUnd	343	-19	1	372	-7	0	17	2.9
Epoxy/amine/10%ZnSt	340	-22	2	368	-11	1	14	0.2

Flammablity of Epoxy/Amine/Zinc salt composites was evaluated by cone calorimeter. The cone calorimeter investigation is very popular and standard method for evaluating and comparing the flammability of polymeric systems. Peak heat release rate (PHRR) is the very important parameter which provides information regarding the size

and glowing speeds of the fire. Cone calorimeter measures other important parameters such as time to ignition (t_{ig}), the mass loss rate (MLR), total heat released rate (THR), amount of smoke produced (SEA) and time of peak heat release rate (t_{PHRR}).

Figure 51 shows significant reduction in PHRR in epoxy/amine/Zinc salt composites compared to pure epoxy/amine. Composites contained 7% of metal salt but only 0.72% inorganic Zn in ZnSt composites, 1.03% in ZnUnd composites and 2.09% in ZnAc composites. The cone test was done multiple times for each sample. PHRR decreased by about 30% for the epoxy/amine/Zinc salt composites. Epoxy/amine/ZnSt had higher PHRR than the other two composites because the corresponding Zinc content is the lowest. This result shows Zinc salt have can be used as flame retardant without combing with other flame retardant materials in Epoxy/Amine systems.

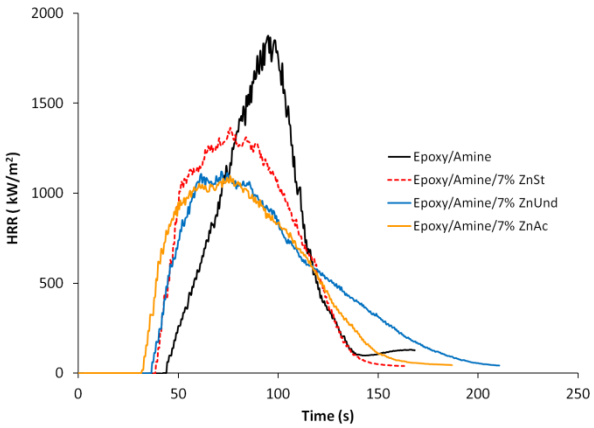

Figure 51. Heat release rate curves for the pristine epoxy/amine thermoset and the resin modified with 7% ZnSt, ZnUnd and ZnAc conducted at an external irradiation 50 kW/m^2.

ZnAc composites with 7%, 13% and 27% fillers were further investigated using cone calorimetry. The PHRR curves of epoxy/amine and epoxy/amine/ZnAc were shown in Figure 52. The PHRR curve for the pure epoxy/amine sample showed a sharp, narrow peak, indicative that the sample was pyrolyzed fairly rapidly. This cone behavior was in accord with the classical patterns typical of weakly charring samples.[19] With an addition

of ZnAc, the shape of HRR curves for the composites changed towards the behavior associated with the formation of a very resistant char barrier layer on the surface of the burning polymer. Adding 7%, 13% and 27% resulted in 49%, 60% and 67% reductions of PHRR values as compared to the unmodified control respectively.

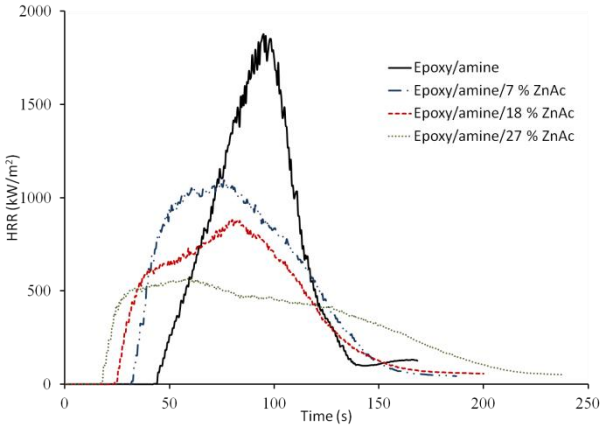

*Figure 52***.** Heat release rate curves for the pristine epoxy/amine thermoset and the resin modified with 7%, 18% and 27% ZnAc conducted at an external irradiation 50 kW/m^2.

The cone data are summarized in Table 9. The time to ignition gradually decreased with increasing ZnAc content. The reduction of the time to ignition showed a correlation with the thermal stability data. The TGA experiments revealed that the thermoset polymer containing ZnAc starts decomposing at lower temperature as compared to the pure epoxy-amine control. It should be noted here that ZnAc melts and decomposes itself at considerably lower temperatures than the polymer in the composites. Smoke release was decreased by adding more ZnAc fillers which was reported previously.[20] With Zinc hydroxystannate (ZHS) in the ethylene-vinyl acetate copolymer system, the smoke emission was decreased. A correlation was found between the reduction in the average mass loss rate (AMLR) and the PHRR values.

Table 9

Cone data summary for epoxy/amine systems containing ZnAc.

Formulation	PHRR (kW/m^2)	Red. (%)	THR (MJ/m^2)	AMLR (g/m^2. s)	t_{ig} (s)	EHC (MJ/kg)	CO yield (kg/kg)	ASEA (MJ/kg)	Residue (wt%)
Epoxy/amine	1977 ±215	N/A	92 ±2	47.2 ±4.2	42 ±1.9	31.1 ±0.3	0.284 ±0.013	743 ±61	0
Epoxy/amine/7%ZnAc	1015 ±144	49	81 ±1	28.2 ±1.5	38 ±7.2	29.9 ±0.7	0.187 ±0.011	635 ±20	11.4 ±0.7
Epoxy/amine/18%ZnAc	789 ±82	60	78 ±1	20.0 ±5.0	32 ±13.6	29.9 ±0.4	0.133 ±0.021	652 ±29	14.2 ±0.4
Epoxy/amine/27%ZnAc	607 ±38	69	73 ±0	17.0 ±1.2	20 ±4.8	29.5 ±0.1	0.211 ±0.010	608 ±27	17.9 ±0.8

Kashiwagi et al. prepared clay-based SAN nanocomposites with zinc chloride as the catalyst.[21] They observed a large improvement in the PHRR relative to the control polymer, but their results indicated that the two additives (clay and zinc chloride) were contributing independently. In this work, ZnAc was able to improve the flame resistant properties without adding halogenated or other flame retardant. Smoke release was decrease which is big improvement for decreasing the damage from the fire. Howeve, ZnAc formed micro dispersion or even big aggregate can be observed in the epoxy-amine composites. With a naked eye, particle aggregation can be observed on the surface. The aggregation may affect the mechanical and other properties of the epoxy materials. In order to improve the dispersion, ZnUnd, another zinc salt with long organic tail compatible with epoxy chains was investigated. ZnUnd has almost the same flame retardant effect as ZnAc which can be seen from the Heat release rate curves, however, ZnUnd may able to disperse well in the epoxy systems to maintain or improve mechanical properties.

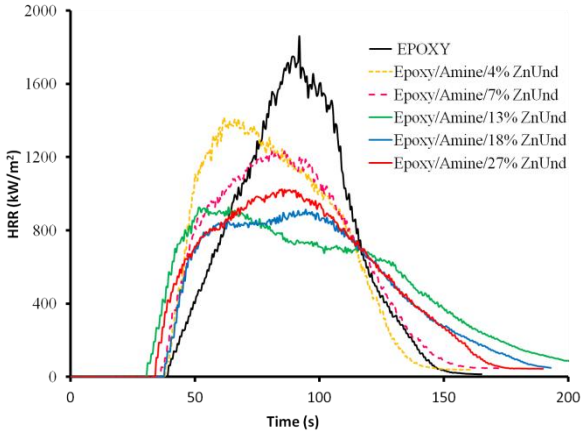

*Figure 53***.** Heat release rate curves for the pristine epoxy/amine thermoset and the resin modified with 4%, 7%, 13%, 18% and 27% ZnUnd conducted at an external irradiation 50 kW/m^2.

Epoxy/Amine resins containing different amount of ZnUnd were evaluated in the cone calorimeter. The cone data are summarized in Table 10 and heat release rate plots are shown in Figure 53. The fire retardant effect of ZnUnd is strong and increased as increase the filler content. Adding 4%, 7%, 13%, 18% and 27% of ZnUnd led to 16%, 31%, 43%, 46% and 43% of PHRR reduction as compared to the pure epoxy/amine system. PHRR gradually decreased by increasing ZnUnd content and reached lever off point after 13% of ZnUnt. The heat release rate curve for the pure epoxy/amine sample showed a sharp, narrow peak, indicative that the sample was pyrolyzed fairly rapidly. With an addition of ZnUnd, the shape of HRR curves for the composites changed and flattened.

The time to ignition (t_{ig}), parameter defined as the time at which the flame started, did not change much with increasing ZnUnd content. Only small amount of decrease was observed due to the early decomposition of ZnUnd as shown in the TGA analysis. It can be seen that effective heat combustion (EHC) and total heat release (THR) of the composites show similar value to the pure epoxy/amine system (Table 10). CO yield and

a measure of smoke yield (ASEA) decreased compared to the pure epoxy/amine system. It was unexpected because adding particles usually leads to polymer in complete combustion and increase of CO yield and ASEA. In this system, the zinc particles may chemically (work as catalysis) and physically (forming barrier layers) affect the smoke release and CO yield which will be discussed later.

Table 10

Cone data summary for epoxy/amine systems containing ZnUnd.

Formulation	PHRR (kW/m^2)	Red. (%)	THR (MJ/m^2)	AMLR (g/m^2. s)	t_{ig} (s)	CO yield (kg/kg)	EHC (MJ/kg)	char (%)	ASEA (m^2/kg)
Epoxy control	1716	NA	91	42.2	41	0.280	30.03	1	725
Epoxy 4 Zinc Und	1440	16	89	35.9	41	0.290	31.27	7	624
Epoxy 7 Zinc Und	1181	31	87	31.9	38	0.261	31.36	10	648
Epoxy 13 Zinc Und	979	43	87	23.5	35	0.218	31.52	11	655
Epoxy 18 Zinc Und	946	45	84	25.3	39	0.224	30.92	12	664
Epoxy 27 Zinc Und	981	43	88	24.7	38	0.188	33.23	12	686

A correlation was found between the reduction in the average mass loss rate (AMLR) and the PHRR values which are graphically shown in Figure 54. Slow release of the fuel or a delay in mass loss has been typically correlated to a combination of physical and chemical phenomena.[22] Three possible reasons were put forward to explain the fire retardant action of ZnUnd in the epoxy-amine thermoset. Perhaps the primary cause is that under fire conditions most of the ZnUnd additive is converted into zinc oxide. Crystalline zinc oxide forms an inorganic layer that covers the surface of the underlying polymer and thus slows down the release of any flammable fragments from the burning

polymer and also reduces the heat transfer to the degrading polymer. Also ZnUnd may participate in the pyrolysis reactions within the condensed phase by promoting a carbonization process which reduces the yield of volatile and combustible products.

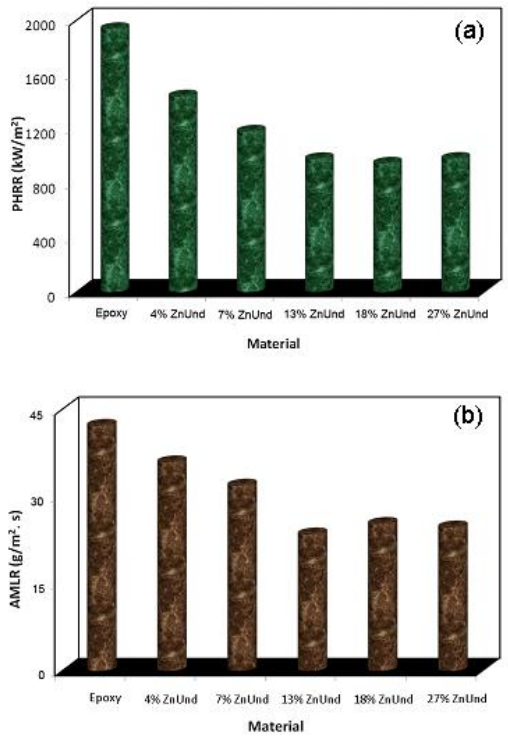

Figure 54. (a) Peak heat release rate and (b) Avergae mass loss rate values for the epoxy/amine/ZnUnd with 4%, 7%, 13%, 18% and 27% filler content.

Figure 55 shows imaged of the cone test residues for the epoxy/amine control and the sample containing 4%, 7%, 13% and 18% of ZnUnd. Adding ZnUnd led to the formation of a char layer upon ignition. The char with ZnUnd additives showed white color due to the inorganic product of the thermal decomposition of ZnUnd while char of epoxy/amine was black. With the addition of more ZnUnd, the char surface layer became much denser, wich less vent holes observed on the char surface. Apparently this whitish zinc oxide char layer formation on the top of the degrading polymer matrix contributes to the fire resistance as it prevents the entry of flammable gases into the gas phase and insulates the underlying polymer from the flame.[10]

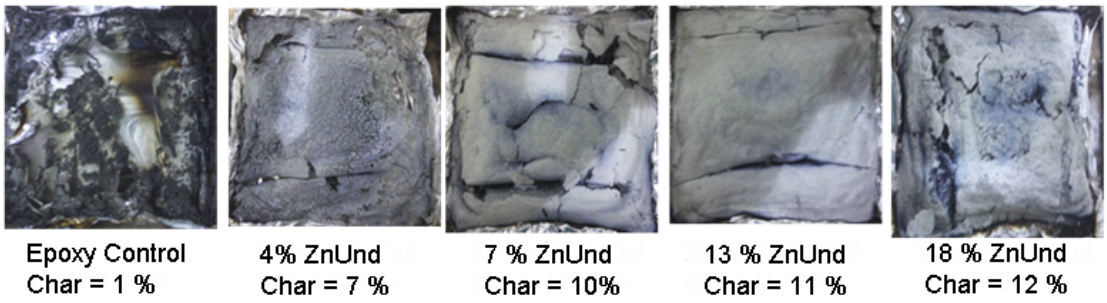

*Figure 55***.** Images of the residues epoxy/amine and epoxy/amine/ZnUnd samples after combustion.

The SEM micrographs of the Char residue of epoxy/amine/ZnUnd composites with 7%, 18% and 27% of ZnUnd are shown in Figure 56 in high and low magnification. The low magnification of epoxy/amine 7% ZnUnd and 18% ZnUnd shows about 50 μm sized hole which were circled. It looks like a lot of disordered flakes accumulated on the surface which is product from Zinc salt. The flake size varied from several micrometer to 50 micrometer which can be oberserved in the high magnification SEM. The char residue of epoxy/amine/27% ZnUnd shows different image compare to the previous two composites. The flakes number increased and covered densely almost the whole surface of the char. This images show that physical barrier was formed by the Zinc particles during the combustion and higher loading composites had more concrete barrier.

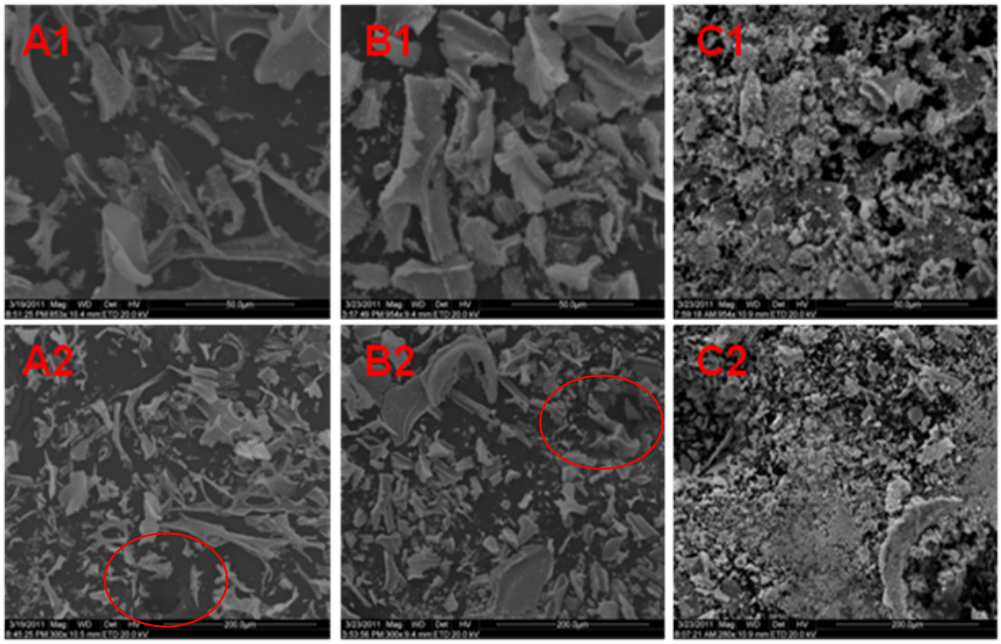

*Figure 56***.** SEM of Char surface of epoxy/amine/ZnUnd composites at low and high magnification with (A1) and (A2) 7% ZnUnd, (B1) and (B2) 18% ZnUnd and (C1) and (C2) 27% ZnUnd.

SEM energy dispersive X-Ray (SEM-EDX) was used to conduct the surface element analysis of the composites char. The results listed in the Table 11. Char of epoxy/amine/7% ZnUnd have about 62.5% carbon and 17.6% Zinc elements on the surface when the composites only have about 1% Zn content. Char of epoxy/amine/27% ZnUnd have about 39.4% carbon and 39.6% Zinc elements when the composites have 4% Zn content. The organic parts were degraded to form combustible gas while inorganic Zn was not able to escape and became residual. It is possible that the surface has much more Zinc elements than the bulk of the char due to transportation of the Zinc particles with the bubble rising during the decomposition of the polymer. In order to confirm the hypothesis, XRD and TGA analysis were conducted.

Table 11

SEM-EDX of the char of epoxy/amine/7% ZnUnd and epoxy/amine/27% ZnUnd for element analysis of Carbon (C) and Zinc (Zn) by weight percentage.

Material	C (wt%)	Zn (wt%)
char-epoxy 7-ZnUnd	62.8	17.6
char-epoxy 27-ZnUnd	39.4	39.6

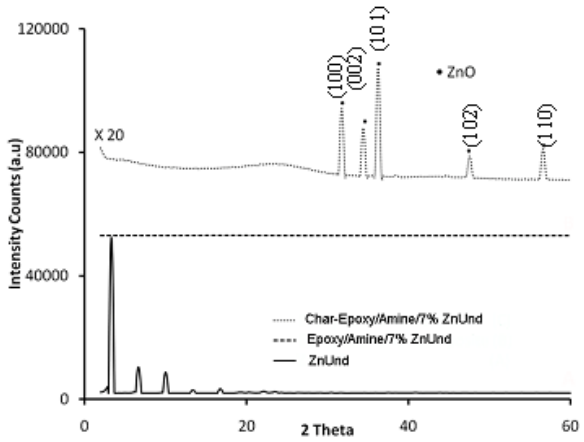

*Figure 57***.** XRD pattems of Char epoxy/amine/7% ZnUnd, epoxy/amine/7% ZnUnd composites, ZnUnd Particles.

Figure 57 shows the XRD of the ZnUnd, epoxy/amine 7% ZnUnd composites and epoxy/amine 7% ZnUnd char. The XRD Patterns of char matches ZnO patterns as described in the previous papers.[23] The observed reflections at room temperature were (100), (002), (101), (102) and (110) reflection which were similar to the observed reflections in ZnO powder. Most of the Zn remained in the char are oxidized form. The XRD patterns of ZnUnd and composites did not show any similar patterns. Related to the surface elements analysis, assuming all the ZnUnd converted to ZnO, one can calculated

inorganic content (ZnO) on the surface are 22.4% (17.6% Zn) for epoxy/amine/7% ZnUnd and 50.3% (39.6% Zn) for epoxy/amine/27% ZnUnd.

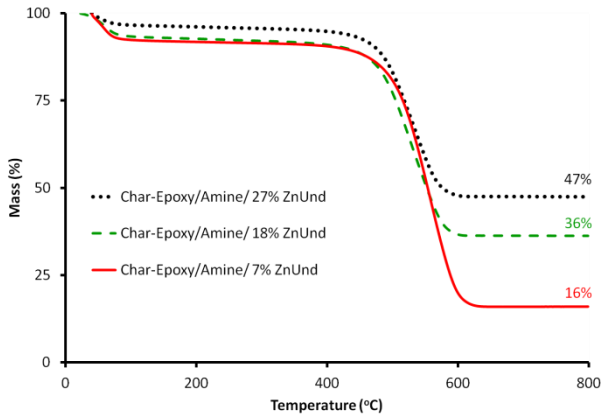

*Figure 58***.** TGA of char epoxy/amine/ZnUnd with 7%, 18% and 27% ZnUnd content in nitrogen atmosphere.

Figure 58 shows TGA curves of Char of epoxy/amine/ZnUnd composites with different amount of ZnUnd. The ZnUnd content were 4%, 18% and 27% which had inorganic Zn content 0.6%, 2.7% and 4.1% respectively before combustion. The inorganic content increased to 16%, 36% and 47% and organic content decreased to 76%, 56% and 48% as shown in the Figure 58 and Table 12 for 7%, 18% and 27% composites char. The inorganic contents were obtained from TGA residual and organic content were obtained from the mass loss of the materials. The results from the TGA are different from the surface element analysis. Inorganic content (ZnO) was higher on the surface (22.4% and 50.3%) than in the bulk (16% and 47%) for both epoxy/amine/ZnUnd char with 7% and 27% ZnUnd in the composites. Char absorbed small amount of water from the atmosphere. The degradation temperature of char was much higher than of composites as expected.

Table 12

TGA analsist of char epoxy/amine/ZnUnd with 7%, 18% and 27% ZnUnd.

	Organic content (A, B, C) (wt%)	Inorganic content (wt%)
char -epoxy 7-ZnUnd	76	16
char -epoxy 18-ZnUnd	56	36
char -epoxy 27-ZnUnd	48	47

In order to further understand the mechanism of the burning of Zinc containing epoxy systems, the partially pyrolyzed samples were analyzed. The epoxy/amine/ZnUnd composites were exposed to the cone with 50 kW/m^2 heat for limited time and immediately quenched using liquid nitrogen before combustion. From the partially pyrolyzed smaples one can analyze process of inorganic particle movement and barrier formation which cannot be observed from totally combusted samples.

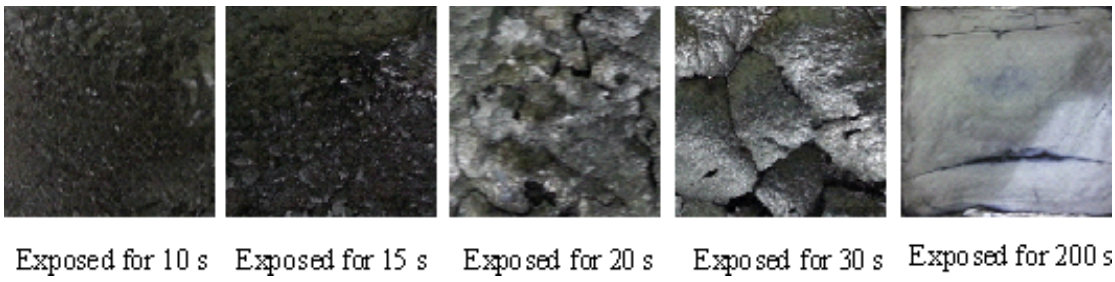

*Figure 59***.** Photographs of the epoxy/amine/14% ZnUnd samples burned for different times and residue after combustion.

Figure 59 shows the epoxy/amine/14% ZnUnd samples exposed under the cone calorimetry for 10 s, 15 s, 20 s, 30 s and 200 s. The first four samples showed samples quenched before flame started (time to ignition was about 40 s) and last photograph shows the totally pyrolyzed sample. The color and surface roughness of the materials

looks different for these samples. Sample exposed for 10 s and 15 s show black color covered with small bumps all over the surface. When exposure time increased, the bump size increased and the surface color became lighter. The samples exposed for 20 s and 30 s had a light gray surface ash, which contained black char underneath. Surface of the 30 s exposed sample only had several big bumps which combined together formed thin layer separated from unburned part of the sample. The sample exposed for 200 s which is totally pyrolyzed sample, has white surface ash with less rough surface. The white colored regin did not extend deep into the sample and bottom of the sample remained black.

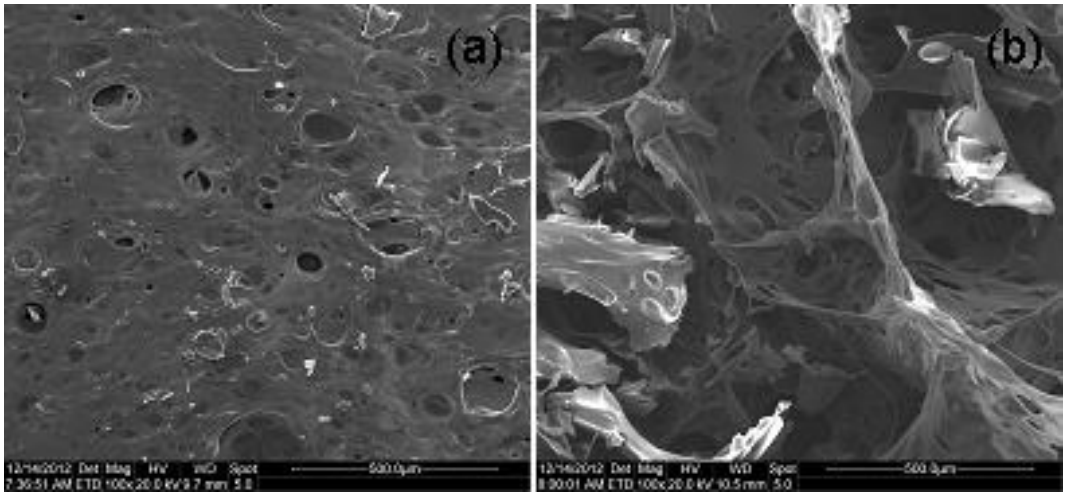

*Figure 60***.** SEM of epoxy/amine/14% ZnUnd sample Exposed for 30 s in the cone calorimeter at 50 kW/m^2 on (a) top area and (b) bottom arear.

SEM of top and bottom of the partially pyrolyzed epoxy/amine/14% ZnUnd sample are shown in Figure 60. The top layer shows small holes on the surface, however, the bottom layer shows almost open cell structure. Both small holes and open cell structures were generated by the polymer pyrolysis. The structure difference between top and bottom layers was due to the accumulation of the Zinc on the surface. Lewin[24,25] suggested movement of silicates from the bulk to the surface is provoked by numerous

rising bubbles which are formed by the decomposing polymer and the clay surfactant for clay-polymer composites. The transportation of Zinc particles from bulk to the surface is aided by the bubbles from the epoxy and Zinc salt decomposition. Because Zinc cannot move to the air, it will accumulate on the surface and make up the surface decomposition.

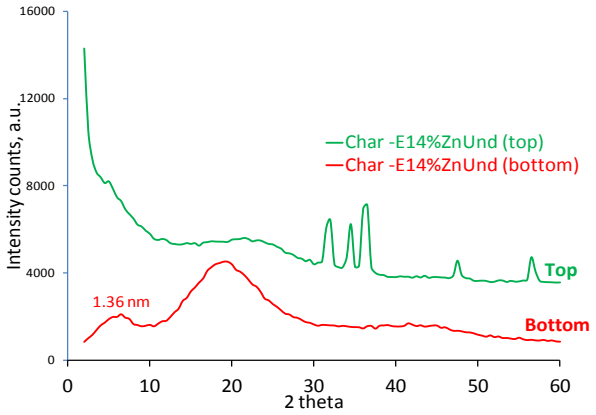

Figure 61. XRD patterns of char of epoxy/amine/14% ZnUnd sample exposed to the cone for 30 s of the top area and bottom area.

XRD can be used to further prove the migration of Zinc particles. Figure 61 shows XRD of the top and bottom of epoxy/amine/14% ZnUnd exposed for 30 s at 50 kW/m^2. The XRD of top area shows several peaks matched patterns of ZnO and bottom area shows totally different peaks. The XRD data from top and bottom layers indicate that top layer contains Zn particles and bottom layers do not have Zn particles.

The transport of Zinc particles were observed by analyzing partially pyrolyzed samples. By increasing the exposure time under the cone the Zinc particles density increased on the surface. The transportation of the Zinc particles cannot be done spontaneously because Zinc materials have higher density than polymers. The motivation is from the movement of the pyrolyzed small molecules and the small molecules carry the Zinc particles to the surface. The Zinc particles accumulated on the surface covering the holes generated from decomposition. That is why surface structure is less porous than

bottom structures. The Zinc particles combined with carbonaceous char formed very dense physical barrier on the surface. The physical barrier slows down the decomposed molecules break out the surface and also decreases the heat transportation. For these particular composites, the physical barrier also decreases the smoke emotion and slows down the total combustion of the polymers.

Conclusions

Zinc salts, ZnAc, ZnUnd and ZnSt, in the epoxy/amine systems were able to improve fire properties without any other synergetic flame retardant additives. Based on the cone measurements, ZnAc has the highest flame retardant effect on the epoxy system. However, poor dispersion of the ZnAc particles formed aggregates in the polymer metrics which may affect other properties. On other hand, improve dispersion of the additives also magnifies the flame retardant effect. ZnUnd and ZnSt with long organic chain were used in order to improve the dispersion in the epoxy systems. ZnUnd composites had better fire properties compare to the ZnSt composites and the dispersion was much better than the ZnAc composites. ZnUnd was not only decrease the PHRR of the polymer, but also decrease the smoke emission, decrease CO gas yield and increase the char formation. XRD, SEM and SEM-EDX studies on the char and partially pyrolyzed samples show that Zn salts converted to ZnO and accumulated on the surface of the composites. The surface of the char and partially pyrolyzed samples had much more ZnO compare to the bulk of the materials due to the transport of the Zn particles with the rising bubbles from the polymer decomposition.

REFERENCES

1. Shieh, J.Y.; Wang, C.S. Synthesis of Novel Flame Retardant Epoxy Hardeners and Properties of Cured Products. *Polymer* **2001**, *42*, 7617–7625.
2. Kinjo, N.; Ogata, M.; Nishi, K.; Kaneda, A.Epoxy Molding Compounds as Encapsulation Materials for Microelectronic Devices. In *Speciality Polymers/Polymer Physics*; Advances in Polymer Science; Springer Berlin Heidelberg: **1989**, Vol 88, 1–48.
3. Nakamura, Y.; Yamaguchi, M.; Okubo, M.; Matsumoto, T.Effects of Particle Size on Mechanical and Impact Properties of Epoxy Resin Filled with Spherical Silica. *J. Appl. Polym. Sci.* **1992**, *45*, 1281–1289.
4. Yung, K. C.; Wu, J.; Yue, T. M.; Xie, C. S. Size Effect of AlN on the Performance of Printed Circuit Board (PCB) Material-Brominated Epoxy Resin. *J. Compos. Mater.* **2006**, *40*, 567–581.
5. Mack, A. G. FlameRetardants, Halogenated. In *Kirk-Othmer Encyclopedia of Chemical Technology (5th Edition)*; Seidel, A.; John Wiley & Sons, Inc.: Hoboken, NJ, **2005**, Vol 11, 454–483.
6. Rahatekar, S. S.; Zammarano, M.; Matko, S.; Koziol, K. K.; Windle, A. H.; Nyden, M.; Kashiwagi, T.; Gilman, J. W. Effectof CarbonNanotubesand Montmorilloniteon The Flammability of Epoxy Nanocomposites. *Polym. Degrad. Stab.* **2010**, *95*, 870–879.
7. La Rosa, A. D.; Recca, A.; Carter, J. T.; McGrail, P. T. An Oxygen Index Evaluation of Flammability on Modified Epoxy/Polyester Systems. *Polymer* **1999**, *40*, 4093–4098.

8. Schartel, B.; Braun, U.; Balabanovich, A. I.; Artner, J.; Ciesielski, M.; Doering, M.; Perez, R. M.; Sandler, J. K. W.; Altstaedt, V. Pyrolysis and Fire Behavior of Epoxy Systems Containing A Novel 9,10-Dihydro-9-Oxa-10-Phosphaphenanthrene-10-Oxide-(DOPO)-Based Diamino Hardener. *Eur. Polym. J.* **2008**, *44*, 704–715.
9. Nara, S.; Matsuyama, K. Thermal degradation and Flame Resistivity of Tetrabrominated Epoxy Resin. *J. Macromol. Sci.: Part A - Chem.* **1971**, *5*, 1205–1218.
10. Morgan, A. B. AReviewof TransitionMetal-basedFlame Retardants: TransitionMetal Oxide/Salts, and Complexes. In *Fire and Polymers V*; Wilkie, C., et al.; ACS Symposium Series; American Chemical Society: Washington, DC, **2009**, 312–328.
11. Masuda, Y.; Kato, K.Tin Oxide Coating on Polytetrafluoroethylene Films in Aqueous Solutions. *Polym. Adv. Technol* .**2010**, *21*, 211–215.
12. Tian, C.; Wang, H.; Liu, X.; Ma, Z.; Guo, H.; Xu, J.Flame Retardant Flexible Poly(Vinyl Chloride) Compound for Cable Application. *J. Appl. Polym. Sci.* **2003**, *89*, 3137–3142.
13. Lu, H.; Hu, Y.; Yang, L.; Wang, Z.; Chen, Z.; Fan, W.Study of The Fire Performance of Magnesium Hydroxide Sulfate Hydrate Whisker Flame Retardant Polyethylene. *Macromol. Mater. Eng.* **2004**, *289*, 984–989.
14. Yu, Y.; Song, P.; Jin, C.; Fu, S.; Zhao, L.; Wu, Q.; Ye, J. Catalytic Effects of Nickel (Cobalt or Zinc) Acetates on Thermal and Flammability Properties of Polypropylene-Modified Lignin Composites. *Ind. Eng. Chem. Fundam.* **2012**, *51*, 12367–12374.
15. Atkinson, P. A.; Haines, P. J.; Skinner, G. A. The Mechanism of Action of Tin Compounds as Flame Retardants and Smoke Suppressants for Polyester Thermosets.

Polym. Degrad. Stab. **2001**, *71*, 351–360.

16. De Fenzo, A.; Formicola, C.; Antonucci, V.; Zarrelli, M.; Giordano, M. Effects of Zinc-based Flame Retardants on The Degradation Behaviour of An Aerospace Epoxy Matrix. *Polym. Degrad. Stab.* **2009**, *94*, 1354–1363.
17. Gilman, J. W.; Kashiwagi, T.; Nyden, M.; Brown, J. E. T.; Jackson, C. L.; Lomakin, S.; Giannelis, E. P.; Manias, E. Flammability Studies of Polymer Layered Silicate Nanocomposites: Polyolefin, Epoxy, and Vinyl Ester Resins. In *Chemistry and Technology of Polymer Additives*; Malden, MA, Ak-Malaika, S., Golovoy, A., Wilkie, C. A.; Blackwell Science Inc.: Blackwell Oxford, UK, **1999**, 249–265.
18. Afzal, M.; Ahmad, H.; Mahmood, F. Decomposition Kinetics of Metal Acetates. *J. Chem. Soc. Pak.* **1991**, *13*, 219–222.
19. Schartel, B.; Hull, T. R. Development of Fire-retarded Materials - Interpretation of Cone Calorimeter Data. *Fire Mater.* **2007**, *31*, 327–354.
20. Cross, M. S.; Cusack, P. A.; Hornsby, P. R. Effects of Tin Additives on The Flammability and Smoke Emission Characteristics of Halogen-Free Ethylene-Vinyl Acetate Copolymer. *Polym. Degrad. Stab.* **2003**, *79*, 309–318.
21. Kashiwagi, T.; Danyus, R.; Liu, M.; Zammarano, M.; Shields, J. R. Enhancement of Char Formation of Polymer Nanocomposites Using A Catalyst. *Polym. Degrad. Stab.* **2009**, *94*, 2028–2035.
22. Morgan, A. B. Flame Retarded Polymer Layered Silicate Nanocomposites: A Review of Commercial and Open Literature Systems. *Polym. Adv. Technol.* **2006**, *17*, 206–217.
23. Singh, P.; Kumar, A.; Davinder, K. D. Zno Nanocrystalline Powder Synthesized by

Ultrasonic Mist-Chemical Vapour Deposition. *Optical Mater*. **2008**, *30*, 1316–1322.

24. Lewin, M. Some Comments on the Modes of Action of Nanocomposites in the Flame Retardancy of Polymers. *Fire Mater*. **2003**, *27*, 1–7.
25. Lewin, M. Reflections on Migration of Clay and Structural Changes in Nanocomposites. *Polym. Adv. Technol.* **2006**,*17*, 758–763.

CHAPTER VII

SUMMARY AND FUTURE WORK

The objective of this study was to analyze the morphology, gas barrier and flame retardant properties of particle reinforced polymer composites. Polymer systems including a polyimide, LLDPE/LDPE and epoxy/amine were investigated after reinforcement with particles such as Chroysite nanotubes (ChNT), high aspect ratio mica and Zinc salt.

In the Chapater III, neat polymer PMDA-ODA polyimide and PMDA-ODA/ChNT nanocomposites were prepared by solvent casting. Improvement in oxygen and water vapor permeability was observed with the addition of a low loading of ChNT when compared to the neat polymers. Water vapor permeability analysis showed a decrease of 58% and oxygen permeability a decrease of 64% with the addition of only 4.50% (vol/vol) ChNT. High and low resolution TEM depicted ChNTs that are well dispersed and orientated in parallel with the film surface in the polyimide matrix at low filler content. However, with increasing the nanotube content the ChNT fillers tend to agglomerate to microsize aggregate which accordingly caused an increase in gas permeability.

In Chapter IV, nanocomposites (LLDPE-mica) and LDPE were multilayed in alternating layers of 17 and 65 layers using a multilayer co-extruder with layer thicknesses of 20 and 5 μm respectively. Gas barrier properties of annealed samples improved when compared to as received multilayer materials because the mica was concentrated in the LLDPE layers. Gas barrier properties of the annealed films improved by 40% due to moving boundary occurred between the LLDPE-mica layers and the

LDPE layers after annealing at 200 ℃ for different annealing times. The mica filled LLDPE layers were shrunk, while the LDPE layers were swelled at increasing annealing times; however, the interdiffusion slowed after 60 min. The filled layers showed a thickness decrease of 30% for the 17 layer and 40% for the 65 layer film after 10 hours of annealing, reaching the limit of boundary movement. The gas barrier properties did not improve further because boundary movement reached completion after a certain time.

Based on Chapter III and IV, it is apparent that both nanotubes and plate-like nanoparticles can improve gas barrier properties of films when dispersed in polymeric matrices. The barrier improvement was correlated to the concentration of the particles, orientation and dispersion. Typically, only with high loadings of nanoparticles can significant barrier improvement be reached. However, increasing the particle concentration results in particle reaggregation and destruction of orientation. Multilayer systems can help resolve this problem; however initial work showed that improvement was not maximized due to moving boundary effect limitations. In the future, different nanotubes, for example carbon nanotubes or halloysite nanotubes with various aspect ratios can be used in different polymer matrices. Nanotube containing composites for gas barrier properties have not been studied extensively previously. It will be interesting to determine how the nanotubes affect the gas barrier properties when the particle chemical structure and aspect ratios are varied. Frther more, the nanotubes also can be used in multilayer systems. As mentioned previously, multilayer systems with clay types of particles limited the moving boundary effect. Tube-like nanoparticles may work differently due to the structural differences.

In Chapter V, the same multilayer systems were studied for flame retardant properties. High aspect ratio mica improved the thermal stability and flame retardancy of the LLDPE. PHRR of 5% (wt/wt) and 10% (wt/wt) mica composites decreased by 32% and 57% compared to neat LLDPE. Multilayer materials consisting of alternating layers of mica filled LLDPE and pure LDPE showed flame retardant properties improvements with loadings only 2.5% (wt/wt) mica. The char formation and PHRR results were similar to the nanocomposites with high loadings of mica. Multilayering and particle concentration though the moving boundary effect resulted in the low loading multilayer materials whose properties are comparable to high loading nanocomposites with the same amount of inorganic fillers.

In Chapter VI, addition of ZnAc, ZnUnd and ZnSt particles into the epoxy/amine systems was able to improve fire properties without any other synergetic flame retardant additives. Based on the cone measurements, ZnAc has the highest flame retardant effect on the epoxy system. However, poor dispersion of the ZnAc particles formed aggregates in the polymer matrices which may affect other properties. On the other hand, improvement in dispersion of the additives also magnifies the flame retardant effect. ZnUnd and ZnSt with long organic chain were used in order to improve the dispersion in the epoxy systems. Addition of ZnUnd was not only decreased the PHRR of the polymer, but also decreased the smoke emission and CO gas yield while increasing the char formation. XRD, SEM and SEM-EDX studies on the char and partially pyrolyzed samples showed that the Zn salts converted to ZnO and accumulated on the surface of the composites.

Chapter V and VI, depict the flame retardant improvement, that are possibly by combining the particles (mica and Zinc slats). The PHRR can be decreased and char formation increased when there are sufficient particles in the polymer matrices. However, adding too much particles decreased other physical properties of the polymers. Multilayer systems and the moving boundary effect enabled the particles to be concentrated in an effective way so as to improve flame retardant properties. The mechanism of the combustion needs to be studied more systematically. On the other hand, flammability test conducted only using cone calorimeter in this study. Other flammability test methods such as ignitability test (Ul94), flame spread test and limiting oxygen index (LOI) can be used to further analyze the fire properties of these materials.